

AD _____

CONTRACT NUMBER DAMD17-94-C-4099

TITLE: Simulates the Tissue Damage from Small Arms Projectiles
and Fragments Penetrating the Musculoskeletal System

PRINCIPAL INVESTIGATOR: Robert D. Eisler, Amiya K. Chatterjee,
George H. Burghart, Peter Loan

CONTRACTING ORGANIZATION: Mission Research Corporation
Fountain Valley, California 92708-4253

REPORT DATE: March 1998

19981013 041

TYPE OF REPORT: Final

PREPARED FOR: U.S. Army Medical Research and Materiel Command
Fort Detrick, Maryland 21702-5012

DISTRIBUTION STATEMENT: Approved for public release;
distribution unlimited

The views, opinions and/or findings contained in this report are
those of the author(s) and should not be construed as an official
Department of the Army position, policy or decision unless so
designated by other documentation.

REPORT DOCUMENTATION PAGE			Form Approved OMB NO. 0704.0188		
Public reporting burden for this collection of information is estimated to average 1 hour per response, including the time for reviewing instructions, searching existing data sources, gathering and maintaining the data needed, and completing and reviewing the collection of information. Send comments regarding this burden estimate or any other aspect of the collection of information, including suggestions for reducing this burden, to Washington Headquarters Services, Directorate for Information Operations and Reports, 1215 Jefferson Davis Highway, suite 1204, Arlington, VA 22202-4302, and to the Office of Management and Budget, Paperwork Reduction Project (0704-0188), Washington, DC 20503.					
1. AGENCY USE ONLY (Leave blank)	2. REPORT DATE	3. REPORT TYPE AND DATES COVERED			
	March 1998	Final (15 Aug 94 – 31 Jan 98)			
4. TITLE AND SUBTITLE		5. FUNDING NUMBERS			
Simulates the Tissue Damage from Small Arms Projectiles and Fragments Penetrating the Musculoskeletal System		DAMD17-94-C-4099			
6. AUTHOR(s)		8. PERFORMING ORGANIZATION REPORT NUMBER			
Eisler, Robert D., Chatterjee, Amiya K., Burghart, George H. ¹ , and Loan, Peter ²					
7. PERFORMING ORGANIZATION NAME(S) AND ADDRESS(ES)		9. SPONSORING/MONITORING AGENCY NAME(S) AND ADDRESS(ES)			
Mission Research Corporation Fountain Valley, CA 92708-4253		U.S. Army Medical Research and Materiel Command Fort Detrick, Maryland 21702-5012			
10. SPONSORING/MONITORING AGENCY REPORT NUMBER					
11. SUPPLEMENTARY NOTES					
Note 1. President, GB Laboratories, Inc., Fountain Valley, California Note 2. Director of R&D, Musculogrpahics, Inc., Evanston, Illinois					
12a. DISTRIBUTION / AVAILABILITY STATEMENT		12b. DISTRIBUTION CODE			
Approved for public release; distribution unlimited.					
13. ABSTRACT (Maximum 200 words)					
This effort used different configurations of ordnance gelatin as surrogate materials to develop an analytical and experimental methodology that describes mechanical damage to human tissue from penetrating wounds. The assumptions employed were specific to the lower extremities and battlefield threats but could be relaxed to generalize the methodology to other body regions, other threats, and other types of wounds. A software package based on this methodology was developed to predict wound geometries. This software was interfaced with a virtual anatomy based on the Visible Human database to describe tissue damage relative to the anatomy of the lower extremities. The software predicts the extent of soft tissue damage as well as bone interaction, including fracture mode and ejected bone fragments.					
14. SUBJECT TERMS		15. NUMBER OF PAGES			
Wound	Ballistics	Biosimulants	Human Tissue	124	
Virtual	Surgery	Penetration	Simulation	16. PRICE CODE	
17. SECURITY CLASSIFICATION OF REPORT		18. SECURITY CLASSIFICATION OF THIS PAGE		19. SECURITY CLASSIFICATION OF ABSTRACT	20. LIMITATION OF ABSTRACT
Unclassified		Unclassified		Unclassified	Unlimited

FOREWORD

Opinions, interpretations, conclusions and recommendations are those of the author and are not necessarily endorsed by the U.S. Army.

Where copyrighted material is quoted, permission has been obtained to use such material.

Where material from documents designated for limited distribution is quoted, permission has been obtained to use the material.

Citations of commercial organizations and trade names in this report do not constitute an official Department of Army endorsement or approval of the products or services of these organizations.

In conducting research using animals, the investigator(s) adhered to the "Guide for the Care and Use of Laboratory Animals," prepared by the Committee on Care and Use of Laboratory Animals of the Institute of Laboratory Resources, National Research Council (NIH Publication No. 86-23, Revised 1985).

For the protection of human subjects, the investigator(s) adhered to policies of applicable Federal Law 45 CFR 46.

In conducting research utilizing recombinant DNA technology, the investigator(s) adhered to current guidelines promulgated by the National Institutes of Health.

In the conduct of research utilizing recombinant DNA, the investigator(s) adhered to the NIH Guidelines for Research Involving Recombinant DNA Molecules.

In the conduct of research involving hazardous organisms, the investigator(s) adhered to the CDC-NIH Guide for Biosafety in Microbiological and Biomedical Laboratories.



PI - Signature

3/2/98

Date

TABLE OF CONTENTS

1	INTRODUCTION.....	8
2	ANALYTICAL DEVELOPMENT.....	10
2.1	RESISTANCE CHARACTERISTICS OF PROJECTILE MOTION IN GELATIN AND TISSUE SIMULANTS	11
2.2	ROTATIONAL KINEMATICS OF A PROJECTILE INSIDE A VISCOELASTIC FLUID	27
2.3	ANALYSIS OF PROJECTILE INTERACTION WITH SOFT TISSUE	32
2.4	KINEMATICS OF BULLET PENETRATION IN A GELATIN WITH EMBEDDED BONES.....	45
2.5	DEVELOPMENT OF THE BONGEL CODE.....	52
3	BALLISTIC TESTING	66
3.1	BALLISTIC IMPACT OF SPHERICAL PROJECTILES INTO 10% AND 15% ORDNANCE GELATIN	75
3.2	BALLISTIC IMPACT OF SPHERICAL PROJECTILES INTO 20% ORDNANCE GELATIN.....	82
3.3	BALLISTIC IMPACT OF PROJECTILES WITH VARIOUS GEOMETRIES AND CONSTITUENT MATERIALS.....	91
4	GRAPHICAL INTERFACE.....	100
4.1	SOFTWARE INTERFACE	100
4.2	GRAPHICAL INTERFACE.....	101
4.3	BOOLEAN CODE FOR INJURY CREATION.....	102
4.4	CODE TO ASSEMBLE INJURED LIMB MODEL WITH TEXTURE MAPS	103
4.5	MODEL QUERY CODE	104
4.6	MATERIAL PARAMETERS.....	104
4.7	CURVATURES AND SURFACE NORMALS	104
4.8	GRAPHICAL DISPLAY OF INJURED LIMB	105
4.9	INTEGRATION OF HEALTHY LIMB MODELS INTO BOOLEAN CODE	105
4.10	PORT MRC CODE TO SGI AND INTEGRATE INTO MGI CODE.....	108
5	CONCLUSIONS AND RECOMMENDATIONS	111

Appendix A

Reprint of MMVR 4 Paper: *Simulation and Modeling of Penetrating Injuries from Small Arms*

Appendix B

List of personnel contributing to this project

LIST OF TABLES

TABLE 1. POLYNOMIAL FIT TO THE RETARDATION FORCE, $F(v)$ FUNCTION	17
TABLE 2. ENERGY AND VELOCITY DATA ON SPHERICAL STEEL PROJECTILES IMPACTING HUMAN FEMURS.....	47
TABLE 3. SUMMARY DESCRIPTIONS OF BALLISTIC TESTS IMPLEMENTED	67
TABLE 4. DEPTH OF PENETRATION DATA FOR $\frac{1}{4}$ " STEEL SPHERE IN 10, 15, AND 20% GELATIN.....	96

LIST OF FIGURES

FIGURE 1. SCHEMATIC OF PROJECTILE-TARGET INTERACTION	12
FIGURE 2. MRC AND EDGEWOOD ARSENAL DATA FOR PENETRATION OF SPHERICAL	16
FIGURE 3. COMPARISON BETWEEN EXPERIMENTAL PENETRATION DATA AND HIGH AND LOW VELOCITY ASYMPTOTES	17
FIGURE 4. THEORETICAL RETARDATION FORCE AND POLYNOMIAL FITS	18
FIGURE 5. COMPARISON OF EXPERIMENTAL PENETRATION DATA AND THEORETICAL RESULTS	18
FIGURE 6. EXPERIMENTAL DATA AND BEST THEORETICAL FIT WITH QUADRATIC FORCE FUNCTION	19
FIGURE 7. COMPARISON OF BALLISTIC DATA VERSUS PREDICTED RESULTS FOR A 19.6-GRAIN	20
FIGURE 8. E(BETA) VERSUS BETA	23
FIGURE 9. COMPARISON OF PENETRATION DEPTH VERSUS STRIKING VELOCITY USING EMPIRICAL FIT TO QUADRATIC FUNCTION VERSUS SEMI-ANALYTICAL APPROACH	23
FIGURE 10. E(BETA _c) VERSUS BETA _c	25
FIGURE 11. RETARDATION FUNCTION, F(V), WITH LOW AND HIGH VELOCITY ASYMPTOTES	25
FIGURE 12. PROJECTILE LOCATION AND LOADING AT TIME T	28
FIGURE 13. SCHEMATIC OF BRL CALCULATION OF PRESSURE FIELD	33
FIGURE 14. RADIATION PATTERN DUE A POINT FORCE	33
FIGURE 15. SCHEMATIC OF MRC MODEL OF MOVING POINT SOURCE	34
FIGURE 16. PRESSURE DISTRIBUTION DURING PROJECTILE PENETRATION	36
FIGURE 17. EFFECT OF ENERGY ABSORPTION ON TEMPORARY AND PERMANENT CAVITY	40
FIGURE 18. CAVITIES AT VARIOUS PENETRATION DEPTHS FOR NON-LINEAR SPRING MODEL	41
FIGURE 19. CAVITIES AT VARIOUS PENETRATION DEPTHS FOR NON-LINEAR SPRING	41
FIGURE 20. AFFECTED ZONES AND CAVITIES AS A FUNCTION OF PENETRATION DEPTH	42
FIGURE 21. SCHEMATIC OF HYSTERESIS EFFECT	43
FIGURE 22. TRANSIENT CAVITIES PLOTTED AT DIFFERENT PENETRATION	43
FIGURE 23. ENTRY AND EXIT VELOCITY OF STEEL PROJECTILES STRIKING EMBALMED HUMAN FEMURS	48
FIGURE 24. ENERGY LOSS AND AVERAGE VELOCITY (SCALED DISPLAY)	49
FIGURE 25. ENERGY LOSS PER UNIT PROJECTED AREA AND AVERAGE VELOCITY	49
FIGURE 26. NOMENCLATURE ASSOCIATED WITH PRE- AND POST IMPACT KINEMATICS	51
FIGURE 27. FLOWCHART OF MRC BONEGEL CODE	55
FIGURE 28. COORDINATE SYSTEMS USED IN BONEGEL CODE	62
FIGURE 29. SHOTLINE AND IMPACT DIRECTION IN THE LOCAL FRAME SYSTEM	63
FIGURE 30. BALLISTIC TEST CONFIGURATION	68
FIGURE 31. PCB TRANSDUCERS 1.5 INCHES FROM TRAJECTORY AT 48 μ SEC	69
FIGURE 32. PCB TRANSDUCERS 3.2 INCHES FROM TRAJECTORY AT 40 μ SEC	69
FIGURE 33. PREDICTED PRESSURE VERSUS CHANGE IN	70
FIGURE 34. PREDICTED VELOCITY IN FEET PER SECOND VERSUS TIME IN MILLISECONDS	71
FIGURE 35. SCHEMATIC OF NON-LINEAR SPRING MODEL	71
FIGURE 36. ANALYTICALLY PREDICTED $\beta = \beta(\alpha)$	73
FIGURE 37. SCHEMATIC AND NOMENCLATURE OF BOUNDARY LAYER SEPARATION FROM SPHERE	73
FIGURE 38. SHADOWGRAM TO SHOW SCALE OF SUBSEQUENT PHOTOS (CALIPER OPEN 1 INCH)	76
FIGURE 39. SHADOWGRAM AT 0 MICROSECONDS IN 10% ORDNANCE GELATIN	76
FIGURE 40. SHADOWGRAM AT 106 MICROSECONDS IN 10% ORDNANCE GELATIN	77
FIGURE 41. SHADOWGRAM AT 287 MICROSECONDS IN 10% ORDNANCE GELATIN	77
FIGURE 42. SHADOWGRAM IN 15% GELATIN RECORDED 286 MICROSECONDS AFTER IMPACT	78
FIGURE 43. SHADOWGRAM IN 15% GELATIN WITH PRESSURE	78
FIGURE 44. SHADOWGRAM RECORDED 2.095 MSEC AFTER IMPACT IN 15% GELATIN	79
FIGURE 45. RESIDUAL CAVITIES IN 15% ORDNANCE GELATIN	79
FIGURE 46. LATE-TIME CAVITY IN 15% GELATIN TARGET WITH PRE-EXISTING RESIDUAL CAVITY	80
FIGURE 47. TRACES FROM BREAK SCREEN AND PRESSURE TRANSDUCER 1	80
FIGURE 48. TRACES FROM FLASH DETECTOR AND PRESSURE TRANSDUCER 2	81

FIGURE 49. SPHERICAL PROJECTILE WITH IMPACT VELOCITY OF 490 FPS AT 1.1 MSEC AFTER IMPACT	81
FIGURE 50. SPHERICAL PROJECTILE WITH IMPACT VELOCITY OF 1,870 FPS 107 MICROSEC AFTER IMPACT.....	81
FIGURE 51. RESIDUAL CAVITY IN 20% GELATIN TARGET	82
FIGURE 52. SPHERICAL PROJECTILE WITH IMPACT VELOCITY OF 1,300 FPS 220 MICROSEC AFTER IMPACT.....	82
FIGURE 53. SPHERICAL PROJECTILE WITH STRIKING VELOCITY OF 1,870 FPS 107 MICROSEC AFTER IMPACT	82
FIGURE 54. SPHERICAL PROJECTILE WITH STRIKING VELOCITY OF 1,940 FPS 133 MICROSEC AFTER IMPACT	83
FIGURE 55. TIME RESOLVED PRESSURE PULSE FOR FIGURE 7 TEST	83
FIGURE 56. TIME RESOLVED PRESSURE PULSE FOR EXPERIMENT IN FIGURE 8	83
FIGURE 57. SPHERICAL PROJECTILE WITH IMPACT VELOCITY OF 1,150 FPS 2.730 MSEC AFTER IMPACT.....	84
FIGURE 58. SPHERICAL PROJECTILE WITH STRIKING VELOCITY OF 750 FPS 88 MICROSEC AFTER IMPACT.....	84
FIGURE 59. TIME RESOLVED PRESSURE PULSE FROM FIRST TRANSDUCER.....	85
FIGURE 60. TIME RESOLVED PRESSURE PULSE FROM REAR SURFACE TRANSDUCER	85
FIGURE 61. TEMPORAL CORRELATION OF PRESSURE HISTORIES	85
FIGURE 62. TIME RESOLVED PRESSURE FOR SPHERICAL PROJECTILE STRIKING 10% GELATIN AT 1,570 FPS	85
FIGURE 63. PEAK PRESSURE IS PROPORTIONAL TO STRIKING VELOCITY SQUARED.....	86
FIGURE 64. CONFIGURATION OF SIMULATED FEMUR BALLISTIC EXPERIMENTS	86
FIGURE 65. TIME RESOLVED PRESSURE FOR SPHERICAL PROJECTILE STRIKING 20% GELATIN AT 1,760 FPS	87
FIGURE 66. SPHERICAL PROJECTILE INCIDENT AT 1,370 FPS, 320 MICROSEC AFTER IMPACT	87
FIGURE 67. SPHERICAL PROJECTILE INCIDENT AT 1,750 FPS 332 MICROSECONDS AFTER IMPACT	88
FIGURE 68. TIME RESOLVED PRESSURE FOR GLANCING IMPACT ON INSTRUMENTED "FEMUR" AT 1750 FPS	88
FIGURE 69. SPHERICAL PROJECTILE INCIDENT AT 2,160 FPS 178 MICROSEC AFTER IMPACT.....	89
FIGURE 70. SPHERICAL PROJECTILE INCIDENT AT 2,060 FPS	89
FIGURE 71. TIME RESOLVED PRESSURE FOR 2,160 FPS STRIKING VELOCITY.....	90
FIGURE 72. TIME RESOLVED PRESSURE FOR BALLISTIC EXPERIMENT IN PREVIOUS FIGURE.....	90
FIGURE 73. BALLISTIC PENETRATION OF BBs INTO 20% ORDNANCE GELATIN	91
FIGURE 74. BALLISTIC PENETRATION OF $\frac{1}{4}$ " SPHERES INTO 20% ORDNANCE GELATIN.....	92
FIGURE 75. $\frac{1}{4}$ " STEEL SPHERE DATA β -SCALED TO BB BALLISTIC PENETRATION DATA.....	92
FIGURE 76. CONFIGURATION OF IN-SITU EXPERIMENTS	93
FIGURE 77. EXPERIMENT 9-12-03	93
FIGURE 78. EXPERIMENT 9-18-02	95
FIGURE 79. EXPERIMENT 9-18-03	95
FIGURE 80. PRESSURE PULSE FROM EXPERIMENT 8-23-02.....	96
FIGURE 81. PRESSURE PULSE FROM EXPERIMENT 9-26-01	96
FIGURE 82. SHADOWGRAM FROM EXPERIMENT 8-23-03	97
FIGURE 83. SHADOWGRAM FROM EXPERIMENT 10-05-01	97
FIGURE 84. PRESSURE PULSE FROM EXPERIMENT 10-5-01	98
FIGURE 85. PRESSURE PULSE FROM EXPERIMENT 7-31-03	98
FIGURE 86. PRESSURE PULSE FROM EXPERIMENT 10-5-01	99
FIGURE 87. INJURY MODELING SOFTWARE	100
FIGURE 88. USER INTERFACE FOR THE INFILCT MODULE OF INJURY CODE	102
FIGURE 89. WIREFRAME MODEL OF PREDICTED TEMPORARY AND PERMANENT CAVITIES	109
FIGURE 90. ANALYTICALLY SIMULATED ENTRANCE WOUND ON THIGH.....	110

1 INTRODUCTION

This report describes development of a software package that simulates tissue damage from small arms projectiles and fragments penetrating the lower extremities. The software can be interfaced with software that performs a detailed biomechanical assessment of residual physical capability, specifically moment generating capability of joints affected. Finally, a graphical interface is provided for medical simulation and training.

Two subcontractors assisted Mission Research Corporation (MRC), MusculoGraphics, Inc. (MGI) of Evanston, Illinois and GB Labs (GBL) co-located with MRC in Fountain Valley, California. MGI developed the interface allowing visualization of the wound tract. This visualization is incorporated in the virtual anatomy developed by MGI as part of the DARPA/MGI *Surgical Simulation for Limb Trauma Management* Technology Reinvestment Program (TRP). GB Labs performed ballistic testing on biosimulant materials to develop a phenomenological database as well as help validate MRC modeling. This testing involved innovative biosimulant target configurations with *in situ* instrumentation.

Major accomplishments of MRC included the development of models describing soft tissue damage from a penetrating wound. This description includes the permanent wound cavity, tissue transient response, and hemorrhagic zone of extravasation. MRC also developed models that describe the interaction of bone tissue with the missile including mode of fracture produced and the resulting kinematics of the projectile in three spatial dimensions and time.

The models, technical insights, and/or biosimulant configurations are already being employed in five other Government projects. In the DARPA/DLA/NRaD *Sensate Liner Development for Combat Casualty Care* (NRaD/MRC N66001-96-C-8641), MRC developed non-invasive sensors and signal processing algorithms that can acquire the acoustic signature of projectiles penetrating soft tissue and determine, in near real-time, the trajectory of the projectile through the human anatomy. This project exploited the soft tissue modeling, biosimulant technology, and wound profile analysis developed in the DARPA/USAMRMC project.

In a project for the Army's Soldier System Command (USASSCOM/MRC DAAH02-98-C-4012) *Development of a Character Simulator for Battlefield Virtual Environments*, MRC is developing a virtual human that incorporates the DARPA/USAMRMC/MRC wound ballistic penetration algorithms. As a subcontractor to Scientific Applications and Research Associates (SARA), MRC is developing models and performing experiments using biosimulant human phantoms developed in the DARPA/USAMRM/MRC project to describe the biological effects of non-lethal, high-energy, toroidal vortices. As a subcontractor to Simulation Technologies, Incorporated (STI), MRC incorporated for the USASSCOM, new wound ballistic and casualty assessment algorithms in the Army's CASRED code. The algorithms were based on the penetration algorithms developed in the DARPA/USAMRMC/MRC project,

Finally, as previously mentioned the DARPA/USAMRM/MRC software is being directly integrated into the *Lower Extremity Battlefield Trauma Simulator* being developed by MGI for DARPA. In this DARPA/MGI project, the MRC software is being used to provide an analytical description of tissue damage from a penetrating wound. This is necessary because although an

entrance and exit wound may be empirically observed and digitized, intervening tissue damage may only be surmised. The DARPA/USAMRM/MRC project thus filled this void by providing physically based analytical models that explicitly describes the interaction of a penetrating missile with tissue.

There are two major shortcomings of the DARPA/USAMRM/MRC models however. First, while the distribution and sizes of ejected bone fragments in soft tissue is modeled, the enhanced tearing of soft tissue resulting from the ejected bone fragments acting as stress concentrations in the projectile wake is not modeled. Second, the correlation of the models with autopsy data was not as extensive as what we would have liked. These shortcomings were not due to any fundamental technical obstacles but rather due to a lack of program resources.

This report is divided into five major sections, as well as two Appendices. The second section, Section 2, describes development of the analytical models and the resulting BONEGEL code. The BONEGEL code describes the physical interaction between projectiles, soft tissue, and bone. Sections 2.1 through 2.4 describe development of the analytical methodologies and insights that are incorporated into the BONGEL software. Section 2.5 describes the detailed structure of BONEGEL. The third section, Section 3, describes the experimental effort that supported analytical model development. Section 4 describes development of the graphical interface and incorporation of the BONEGEL code into a software package that enables reading tissue geometries and properties from a virtual anatomy based on the visible human. Section 5 details conclusions and recommendations from the entire effort. Appendix A includes a paper originally presented at *Medicine Meets Virtual Reality IV*. This paper gives an overview of the phenomenology, modeling, experimental efforts, and accomplishments of this program. References to other presentations made on behalf of this program are listed below. Appendix B lists the MRC, MGI, and GBL personnel involved in this effort.

- R. D., Eisler and A. K. Chatterjee, *Analytical Simulation of Wound Tracts from Missile Penetration*, PROCEEDINGS OF SEVENTH INTERNATIONAL SYMPOSIUM OF WEAPON TRAUMATOLOGY AND WOUND BALLISTICS, St. Petersburg, Russia, 20-23 September 1994 (Unclassified).
- R. D., Eisler and A. K. Chatterjee, *Simulation and Assessment of Musculoskeletal Trauma from Ballistic Penetration*, MEDICINE MEETS VIRTUAL REALITY, III, Sponsored by the University of California Medical School at San Diego, the Commission on the European Union, and the U.S. Advanced Research Projects Agency, San Diego, 21 January 1995 (Unclassified).
- A. K. Chatterjee and R. D. Eisler, *Ballistic Penetration into Gelatin*, IMPACT, WAVES, AND FRACTURE, Proceedings Of The Werner Goldsmith Symposium, sponsored by the Applied Mechanics Division of the American Society of Mechanical Engineers and the University of California at Los Angeles, Los Angeles, 28 - 30 June 1995, ASME Applied Mechanics Division, Volume 205, pp. 9-20, 1995 (Unclassified).
- R. D., Eisler, A. K. Chatterjee, and G. H. Burghart, *Simulation and Modeling of Penetrating Injuries from Small Arms*, published in: HEALTH CARE IN THE INFORMATION AGE: FUTURE TOOLS FOR TRANSFORMING MEDICINE, presented at the Medicine Meets Virtual Reality 4 International Symposium sponsored by The University of California School of Medicine, the Advanced Research Projects Agency, American Psychiatric Association, Institute for Telemedicine, Society for Minimally Invasive Surgery, Society of Gastrointestinal Endoscopic Surgeons, and Society of Cardiovascular and Interventional Radiology, San Diego, California, 17 – 20 January 1996 (Unclassified).

2 ANALYTICAL DEVELOPMENT

During the course of this program various formulations of ordnance gelatin (250A from Knox and Kind) were used during ballistic experiments as surrogates for human tissue. These experiments are elaborated in Section 3. Ordnance Gelatin was selected based on two factors. First, ordnance gelatin demonstrates phenomenology that is similar to penetration in human soft tissue. Second, ordnance gelatin is a non-linear, viscoelastic material that has many of the same unknowns, in terms of material properties, that *in-vivo* human tissue has. That is, a fundamental technical obstacle that thwarts analysis of projectile-human tissue interaction is the lack of *in-vivo* dynamic properties of living tissue. Further, it is unlikely that these properties will ever be acquired.

Another complication is that human tissue undergoes phase transitions during the penetration process. At high penetration velocities tissue tends to act more like a viscous fluid. At low penetration velocities tissue tends to behave as a viscoplastic solid. Most of the material adjacent to the projectile however, particularly at intermediate velocities (which is where most of the wound tract is established) is a multiphase medium with even less defined material properties. Thus, any technique that relies on the input of these properties for human tissue, such as finite element or hydrocode techniques, at least for the analysis of "dynamic events" involving human tissue, is of questionable utility. Rather, a technique is required that can analyze the dynamic interaction between a penetrating missile and human tissue in terms of data that exists and is appropriate for this type of interaction.

An assumption in this program has been that if ballistic penetration into ordnance gelatin can be analyzed using the material properties available or measurable for ordnance gelatin targets, then the same methodology can be applied to human tissue since the same material property unknowns and phenomenology applies to human tissue. Note this assumption is far less restrictive than what the lethal effects community normally assumes in using ordnance gelatin targets. That is, the lethal effects community normally assumes that penetration in human tissue can be linearly related (i.e., scaled) to penetration in either a 10% or 20% ordnance gelatin target. Without addressing the veracity of this controversial issue, we make no such assumption. We merely assume that the phenomenology and that the material property unknowns are similar.

Using this set of assumptions, our approach has been to parametrically vary the gelatin formulation to document the change in gelatin mechanical properties and effect on projectile terminal ballistics. A model is then developed that describes the observed trends in terms of the parameters and mechanical properties that were varied.

This model, based on the previous assumptions, should have the same parametric form as the analogous model describing the same phenomenology in human tissue. If the model parameters are formulated in terms of stable, independently measured material properties that are available for gelatin as well as human tissue, with the appropriate substitution of parameters, the response in human tissue can be described. Validation of this approach is achieved by comparing predicted wound tracts to autopsy data. It should be noted that the analytically predicted wound tracts are based on a sequence of highly non-linear interacting events. These events include the transient expansion and recovery of tissue in the projectile wake. This expansion and recovery

results in a hysteresis effect and the accumulation of inelastic strain which results in the permanent wound tract. Given the highly non-linear nature of the projectile-tissue and projectile-gelatin interaction, any agreement of analytically predicted wound tract characteristics and observed wound tracts would greatly exceed random probability and therefore must be the result of correctly modeling the physics of the interaction.

In general, analytical predictions successfully correlated with the experimental results on gelatin targets and the more limited autopsy data (which we would have liked to pursue if program resources were available).

2.1 RESISTANCE CHARACTERISTICS OF PROJECTILE MOTION IN GELATIN AND TISSUE SIMULANTS

During penetration of a projectile inside a target, the retardation force that decelerates the projectile arises due to its contact with surrounding target material. The nature of these contact forces depends on the kinematic state of the projectile and possibly on its kinematic history as well. For example, in the case of a penetration velocity that is much slower than the speed of sound, c_p , in the material, the retardation force is approximately equal to the compressive fracture threshold of the material, and hence can be regarded as a material constant, c_f .

Alternatively, when the penetration velocity is comparable to c_p , the target material behaves like a viscous fluid medium, and hence the force of resistance, F , is no longer a material constant but depends on the local kinematics and possibly on kinematic history of the projectile penetration. Most experimental studies done in the fluidized state of the material assume that the character of F depends on the steady state fluid drag on the projectile even when the problem is temporally unsteady.

Assuming that this is a valid approach, F is proportional to v^2 in this regime where v is the steady state velocity of the flow. But since F is the surface integral of the contact forces over the contact area, it is physically evident that for unsteady problems, the contact area may not only depend on the instantaneous velocity of the projectile but may also depend on the history of loading prior to the current state. The contact area also depends on the locations of boundary layer separations. Determination of boundary layer separations in unsteady flow is a very complex mathematical problem that has not been solved to date except by purely numerical algorithms implemented on super computers.

Here we have taken a different approach. Our goals are to bypass the complex step of numerical integration of nonlinear differential equations and to develop a technique based on a semi-analytical approach, that can be used to estimate the retardation force, F , for a given target over a given range of entry velocities.

For our analysis, we assume that there exists an experimental database that contains an array of penetration depths and corresponding entry velocities for the target material under study. Our analysis also deals with the relationships between the model parameters and physical parameters of the problem as much as practicable, so that an extension of our analysis to unknown materials (where no penetration data are available) can be made. With these goals in mind, we start with

the assumption that, even in an unsteady problem, F depends only on the instantaneous velocity of the projectile. We also conceive that our *projectile is made up of a rigid collection of particles* so that F can be determined by integrating the forces on such particles over the surface of the projectile. Thus, we need a basis of determining the force on one such spherical particle. For our purpose, we used small spherical projectiles to simulate such particles. Questions may arise as to whether these projectiles are suitable for simulating particles that constitute a particular projectile. The success or failure of our approach will determine whether the use of other particle simulants is warranted.

Thus, we have reduced the problem of determining the retardation force on a projectile penetrating a given target to the problem of determining the retardation force, $F(v)$ *per unit mass*, on a spherical projectile where F is an unknown function of the instantaneous velocity of the projectile inside a target. The penetration problem of such a particle inside a target is schematically shown in Figure 1.

We also assume that we have an experimental database relating the distribution of the penetration depth function, $\delta(v_0)$ (Figure 1) as a function of entry velocity, v_0 . Furthermore, the low and high velocity behaviors are assumed to be known and these are given by

$$\lim_{v \rightarrow 0} F(v) = c_f, \quad \lim_{v \rightarrow c_p} F(v) = \alpha v^2 \quad (1)$$

In Equation 1, both c_f and α depend on target material properties.

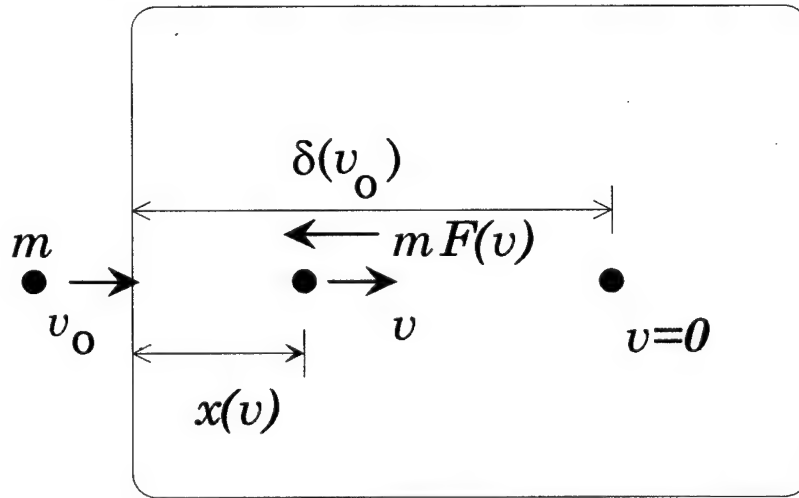


Figure 1. Schematic of projectile-target interaction

Let us first establish an exact relation between the two-function $\delta(v)$ and $F(v)$ introduced above. The equation of motion of the center of mass (CM) of the projectile is given by

$$v \frac{dv}{dx} = -F(v) \quad (2)$$

Integrating (2) from $x=0$ to $x=\delta$, we have

$$\delta(v_0) = \int_0^{v_0} \frac{vdv}{F(v)} \quad (3)$$

Since (3) is valid for all v_0 , we have, after differentiation of (3) with respect to v_0 ,

$$F(v) = \frac{v}{\frac{d\delta}{dv}} \quad (4)$$

Equation (4) is valid for all values of the local velocity v of the projectile inside the target, and establishes the exact relation between the retardation force $F(v)$ *per unit mass* and the penetration depth δ . Equation 4 can be used to estimate $F(v)$ from the experimental database of $\delta(v)$ and v . Below we present a method of estimating $F(v)$ and v from known $\delta(v)$ and v .

2.1.1 Determination of the Projectile Retardation Function, $F(v)$

2.1.1.1 Low Velocity of Penetration

From the first equation in (1) and (4), it is clear that

$$\lim_{v \rightarrow 0} \delta(v) \approx v^2 \quad (5)$$

and hence in the low velocity range $\delta(v)$ can be expanded in a Taylor's expansion as

$$\delta(v) = v^2(a + bv + cv^2 + \dots) \quad (6)$$

We can now estimate the constants $a, b, c \dots$ in (6) by first dividing the experimental data by v^2 and then fitting a polynomial to the reduced data. The relation between the constant a in (6) and the physical constant c_f can be found by using (1), (4) and (6). These give

$$c_f = \lim_{v \rightarrow 0} F(v) = \lim_{v \rightarrow 0} \frac{v}{\frac{d\delta}{dv}} = \frac{1}{2a} \quad (7)$$

Thus, the leading term in the expansion of $\delta(v)$ in (6) can be found from physical data of c_f that can be interpreted as the ultimate static strength of the material.

2.1.1.2 High Velocity of Penetration:

From the second equation in (1) and (4), it is clear that $\delta(v)$ behaves like the natural logarithm of v when the velocity v is comparable to the sonic velocity, c_p , of the target medium. Hence in this region, $\delta(v)$ can be expanded as

$$\delta(v) = a' \ln(v) + \frac{b'}{v} + \frac{c'}{v^2} + \dots \quad (8)$$

The constants a' , b' , c' etc. can now be calculated from the experimental data for large v using a fit of the form of (8) to $\delta(v)$. Since α in (1) is related to the drag coefficient for the target medium, α is a physical parameter which, using Equations (1) and (8), can be related to the coefficient of a' of the leading term in (8). This yields $\alpha = \frac{1}{a'}$.

2.1.1.3 Solution in the Intermediate Velocity Region

In the intermediate region of the penetration velocity v , the solution for $F(v)$ and the analytical fit for $\delta(v)$ can be found by using matched asymptotic expansions of these functions in the low and high velocity range. This procedure is discussed in more detail in Section 2.1.1.9. The matched asymptotic technique is based on the simple rule that there is an overlapping region in the intermediate velocity range where both the low velocity (Equation 6) and high velocity (Equation 8) expansions yield the same result. This procedure is discussed and is illustrated by the example discussed in Section 2.1.1.5 below.

2.1.1.4 Final Polynomial Fit to $F(v)$

After the determination of $F(v)$ is complete using the procedure given above, it is possible to fit a polynomial in v to fit the resulting $F(v)$. The virtue of such fit can be realized in the theoretical prediction of the penetration depths for velocities in the interior of or outside the experimental database. Since the calculation of $\delta(v)$ from a fitted $F(v)$ involves an integration (which is a smoothing process) as in Equation 3, estimates of $\delta(v)$ are usually very good. These expansions are however not valid for characterization of $\delta(v)$ using the differential relation in (4) as they may predict the incorrect behavior of these functions at both low and high velocity domains. For example, if the polynomial fit

$$F(v) = \beta_1 + \beta_2 v + \beta_3 v^2 + \beta_4 v^3 \quad (9)$$

is used to predict the behavior of $\delta(v)$ for high velocity ranges using (4), we get

$$\delta(v) \approx \frac{1}{v} \text{ and } F(v) \approx v^3 \quad (10)$$

Equations 10 contradict Equation 8 and the second equation in (1) respectively.

2.1.1.5 An Example

For the case of a target made of 20% gelatin, we have gathered experimental data on penetration depth and entry velocity for small spherical projectiles. These projectiles are composed of steel with a mass of about 0.344 grams and a diameter of 1.0 cm and density of 8.46 grams/cc, approximately. The entry velocity has been varied from 340 ft/sec to 6,000 ft/sec and the total penetration depth was measured in inches. A schematic of these experiments is shown in Figure

1 and the experimental data, with supplementary experimental data from the Edgewood Arsenal, are shown in Figure 2.¹

2.1.1.6 Data Processing

2.1.1.6.1 Low Velocity Region

As indicated previously, in this range we first compute $\delta(v)/v^2$ versus v from the known experimental data prior to a polynomial fit to obtain $\delta(v)$ in the form

$$\delta(v) = v^2 \sum_{i=0}^n a_i v^i \quad (11)$$

where n is the degree of the polynomial and a 's are unknown constants to be determined from the polynomial fit to the experimental data. For $n=2$, we find

$$a_0 = 5.13 \times 10^{-6}, \quad a_1 = -2.844 \times 10^{-9}, \quad a_2 = 5.0 \times 10^{-13}.$$

2.1.1.6.2 High Velocity Region

For high velocities, $\delta(v)$ behaves like $\ln(v)$ and hence can be expanded as

$$\delta(v) = a' \ln(v) + \sum_{i=1}^n b_i v^{-i} \quad (12)$$

The a' and b_i 's can be calculated from fitting (12) to the experimental database for high velocities. This yields $a' = 1.261$, $b_i = -7.67 \times 10^3$. Comparisons between the low and high velocity asymptotes and the experimental data are shown in Figure 3. As indicated previously, there is an intermediate region of velocity where both of these asymptotes yield the same penetration depth. For this experimental database, this region is seen to lie between 2000 ft/sec to 2200 ft/sec (Figure 3).

¹ R. D. Eisler, et al, *Phase II Development of a Soldier Protective Ensemble Computer Aided Design (SPE/CAD) System*, Final Report for U.S. Army Natick Contract DAAK60-C-92-0008, Mission Research Report MRC-COM-94-R-0455, 4 July 1997, To Be Published as U.S. Army Soldier System Command Technical Report.

² BRL: Report No. 2423, 1974.

³ Huelke, D. F. et. al, *An experimental study in bio-ballistics: Femoral fractures produced by projectiles-II, Shaft Impacts*, J. BIOMECHANICS, Vol. 1, pp. 313-321, 1968

⁴ R. D. Eisler and A. K. Chatterjee, *Effect of Coatings and Processing on Failure of Polycarbonate Substrates During Ballistic Impact*, Final Report for Natick/MRC contract DAAK60-91-C-0087, MRC report MRC-COM-R-97-500, To Be Published as Natick Technical Report, 31 December 1997.

⁵ MRC conducted an extensive literature search to acquire data relative to bone trauma produced by ballistic events. Less than twelve sources were identified since 1900. The most recent data is from the People's Republic of China during the mid-1980's. In general, the data from these experiments is compromised by the relatively unsophisticated instrumentation available at the time. We submitted a proposal to DARPA in conjunction with Maj. Paul Dougherty, M.D., USAMC to conduct ballistic tests on femurs embedded in gelatin matrices with *in-situ* instrumentation. In addition to the *in-situ* instrumentation, the bones would be tested in a fixture that would impose tendon and gravity loads representative of a standing soldier. Although, this proposal was selected for funding, the overall Government program funding these activities ended and hence this proposal remained in abeyance.

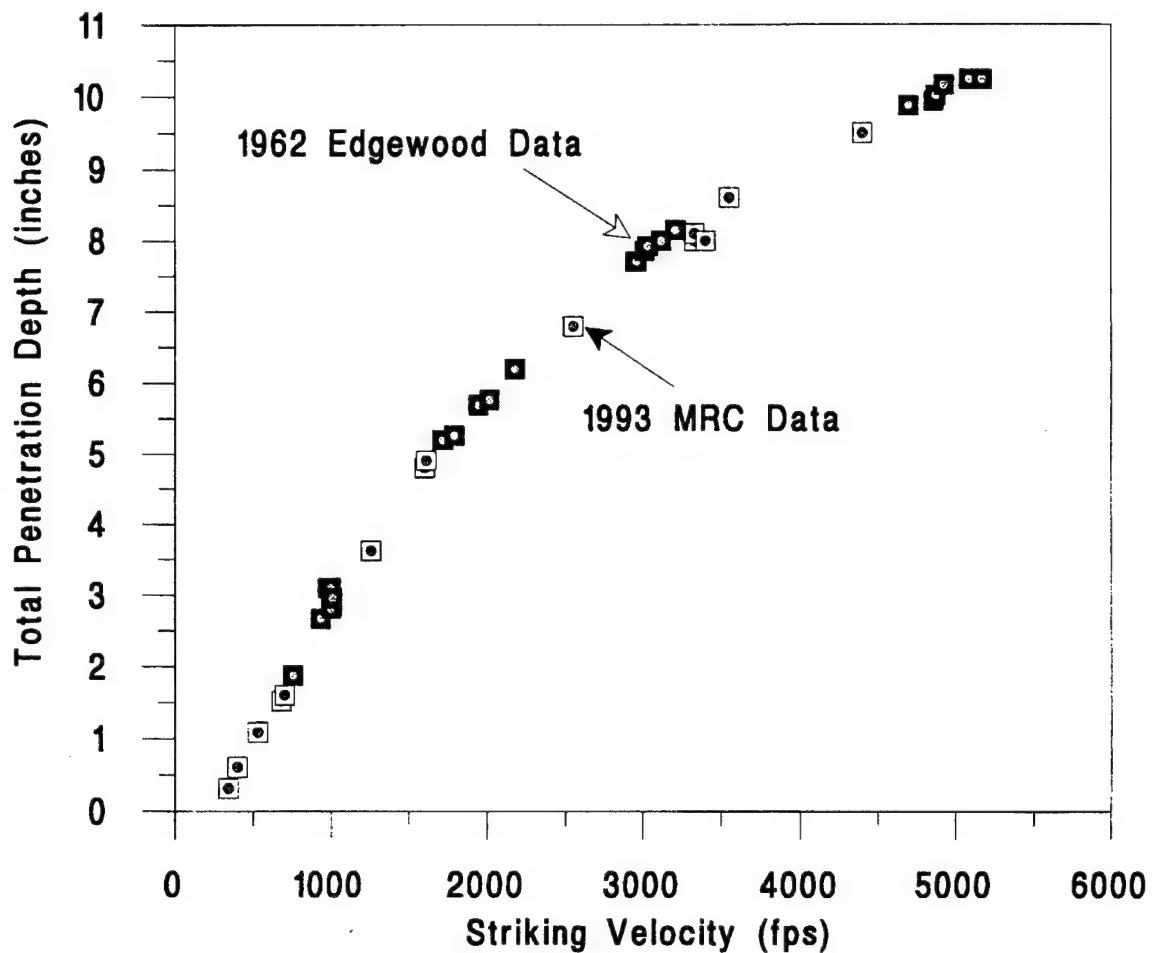


Figure 2. MRC and Edgewood Arsenal Data for Penetration of Spherical Projectiles into 20% Ordnance Gelatin (Reference 1)

2.1.1.7 Determination of Retardation Force

Using the low and high velocity asymptotes of $\delta(v)$ given in Equations 11 and 12, respectively, and the relation between $F(v)$ and $\delta(v)$ given in Equation 4, we can determine the retardation force $F(v)$. For the current database, the computation of $F(v)$ is shown in Figure 4 by the solid line curve. We fit polynomials of degrees 2, 3 and 4 to the theoretical $F(v)$ distribution and these results are shown in Figure 5. The coefficients of these polynomial fits are tabulated in Table 1.

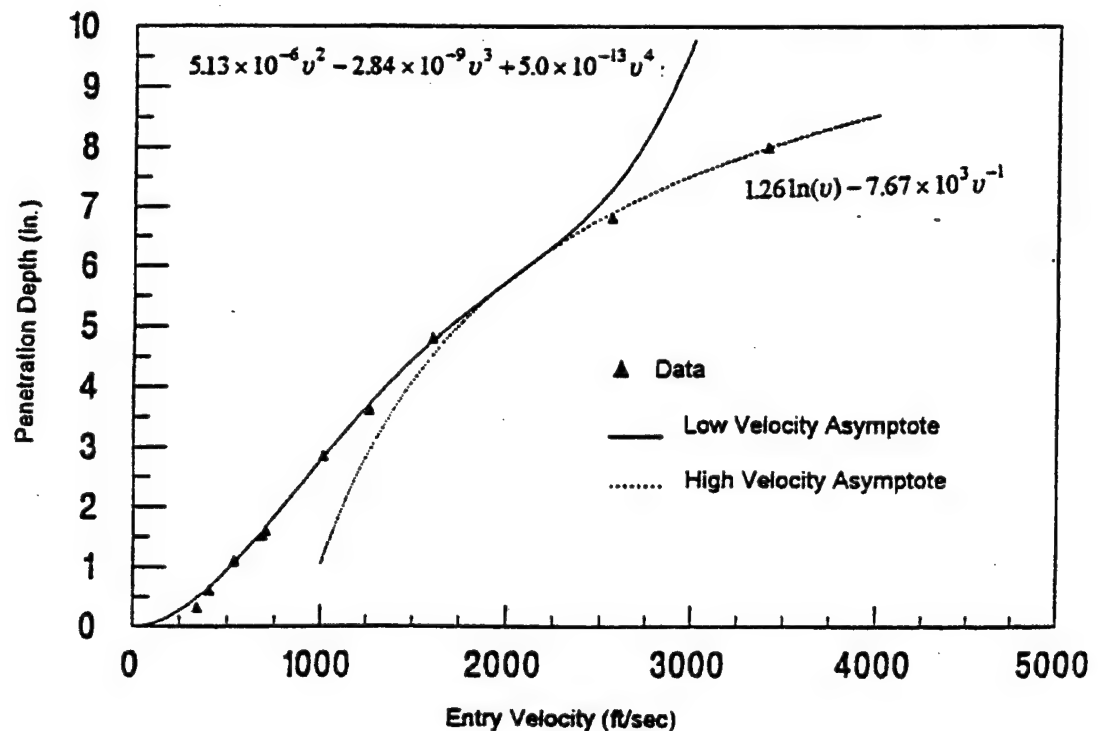


Figure 3. Comparison Between Experimental Penetration Data and High and Low Velocity Asymptotes

Table 1. Polynomial Fit to the Retardation Force, $F(v)$ Function

Degree of Polynomial Fit to $F(v)$	Coefficients in ascending order of the variable				
2	2.45×10^5	-570.63	0.044		
3	0.95×10^5	106.46	2.287×10^{-5}	7.04×10^{-5}	
4	0.88×10^5	195.33	-0.16	1.48×10^{-4}	1.07×10^{-8}

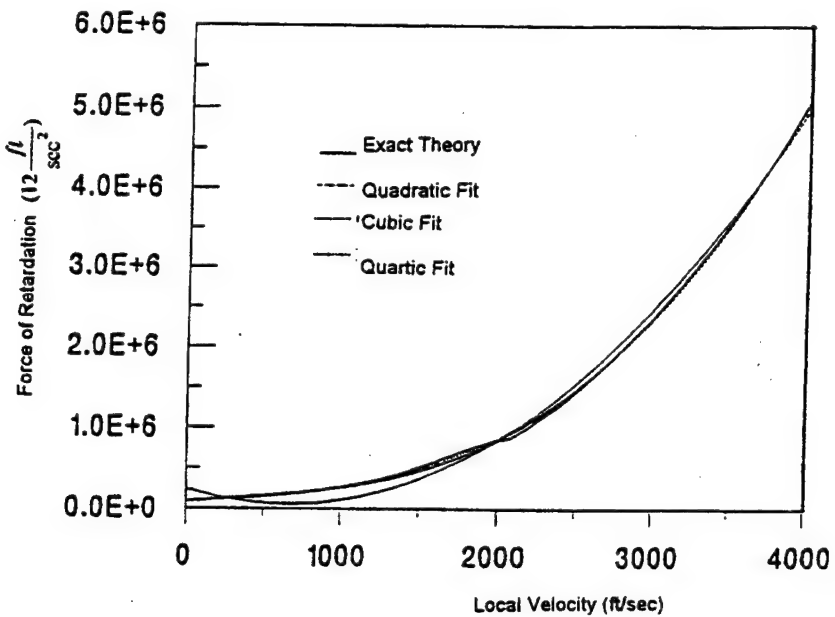


Figure 4. Theoretical Retardation Force and Polynomial Fits

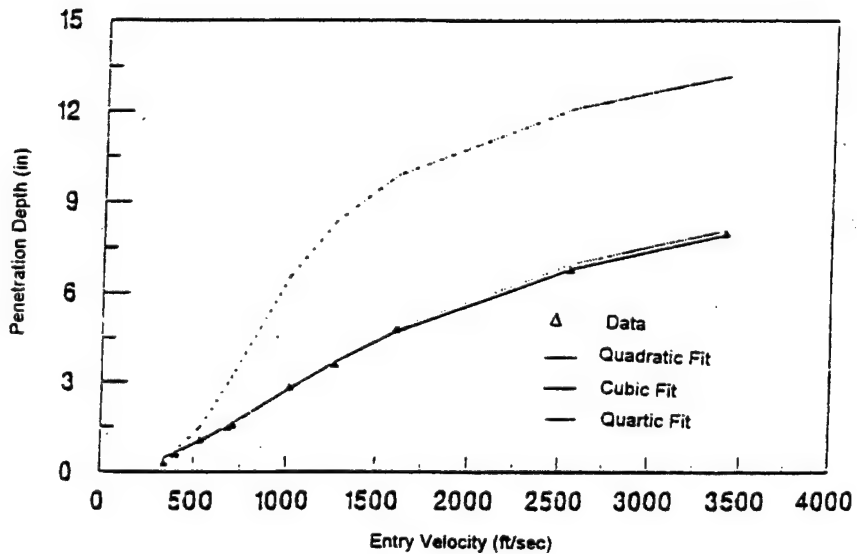


Figure 5. Comparison of Experimental Penetration Data and Theoretical Results

Once we have determined the theoretical distribution of the retardation function $F(v)$, we can now calculate the theoretical penetration depth function, $\delta(v)$, so that the accuracy of the theoretical calculations can be estimated. Using (3) and the polynomial fits given in Table 1, we have compared the experimental data with the theoretical prediction of the penetration function.

The results are shown in Figure 5. From Figure 5, we see that the cubic polynomial fit of the retardation function, $F(v)$, gives the best result while the quadratic fit yields the worst result. To improve the fit of the quadratic form of the retardation function we have adjusted the coefficients of the second row of Table 1 so as to yield the same experimental penetration depth at the maximum velocity of 3400 ft/sec in the current database from spherical projectiles into 20% gelatin. The new coefficients to the quadratic fit to $F(v)$ are 4.046×10^5 , -941.54, 0.72. The resulting $\delta(v)$ from this fit is compared with the experimental data in Figure 6.

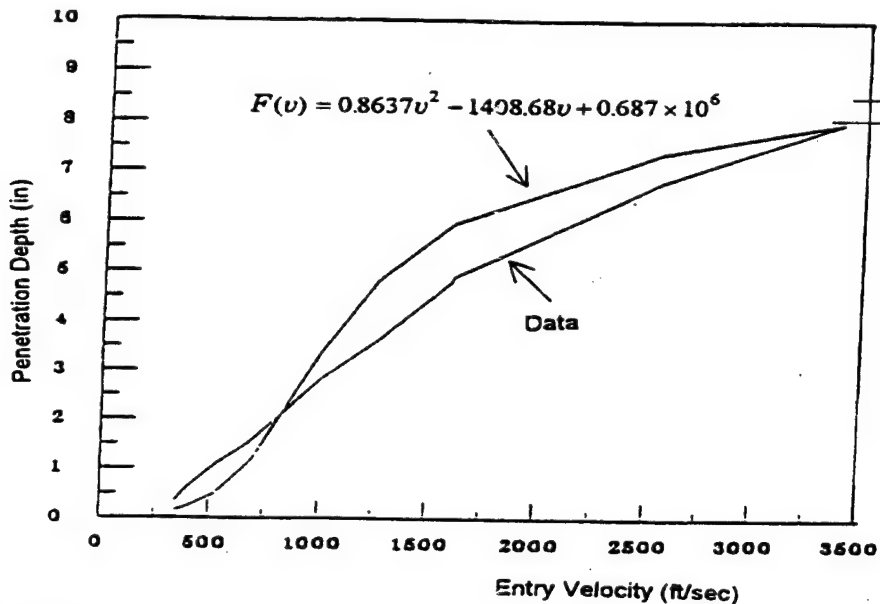


Figure 6. Experimental data and best theoretical fit with quadratic force function

2.1.1.8 Application to Flechette Penetration Database

We have experimental results on the penetration of flechettes into 20% gelatins from Natick/MRC contract DAAK-92-C-0003. As part of this effort MRC developed numerical algorithms which can describe the two-dimensional motion of a flechette when the quadratic form of the retardation force is prescribed. To estimate the accuracy of these algorithms, which is based on modeling the projectile as a rigid ensemble of particles where the resistance to particle penetration is derived from the retardation functions derived from small spherical projectiles, we have applied the above estimated polynomial fit to the retardation force function as input to our flechette code. Unfortunately, at the time of development of the flechette code, we assumed that a good quadratic fit is possible, and hence a quadratic retardation force and local velocity is assumed in the code. Since it is resource intensive to modify our flechette code to incorporate higher order polynomial fits, we decided to use the modified coefficients for the quadratic, $F(v)$ and v (Figure 6) in our flechette code to obtain and compare the theoretical predictions to the experimental flechette database. Figure 7 compares results from a ballistic test for a flechette versus predicted results. The results agree reasonably well considering the fact that we have not used a good fit to the retardation function $F(v)$. If the current flechette code were modified to accept higher order $F(v)$ and v polynomials, we would expect much better agreement between experimental data and the theoretically predicted results.

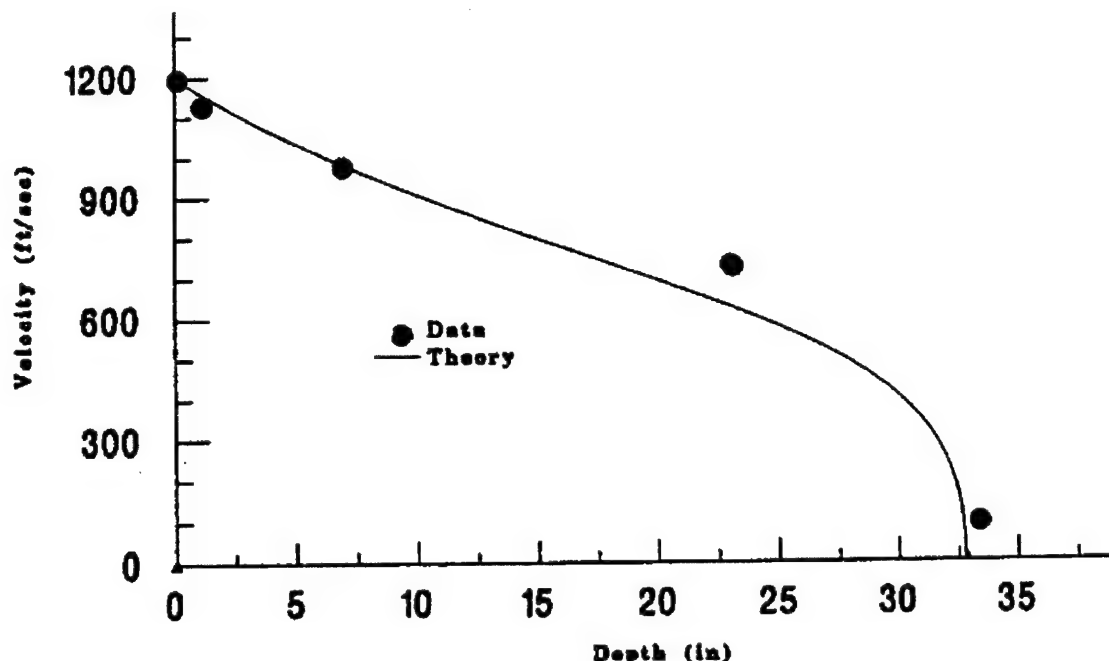


Figure 7. Comparison of Ballistic Data versus Predicted Results for a 19.6-grain flechette striking 20% ordnance gelatin at 1200 ft/sec with a 6.6 degree yaw

2.1.1.9 Calculation of Retardation Coefficients from Penetration Data

As concluding remarks to the above analysis, we would like to point out some important aspects of the theoretical modeling of penetration problems. First, in the absence of basic understandings of the physics for low and high entry velocities, it is not possible to model the nature of the retardation force from experimental data. In this regard, Equation 4 should be used as a guiding equation to connect the characters of the two fundamental functions; $\delta(v)$, the penetration and entry velocity function and $F(v)$, the retardation force and local velocity function. Special care should be taken when we use the derivative of $\delta(v)$ to obtain $F(v)$, and large errors may be introduced if the proper functional forms, Equations 7 and 8, are not used.

Secondly, the usual quadratic, polynomial form of the retardation force function, $F(v)$ and v , does not yield acceptable solutions when compared with the experimental data, and correct forms should be carefully incorporated in the analysis. It is interesting to mention here that a quadratic form is tempting because it predicts correct behaviors at both high- and low-velocity regions. But our problem here is to come up with a functional form that can be used for intermediate velocities as well. This is exactly where such a functional form fails to provide the correct results. Since $\delta(v)$ depends on the integral of $F(v)$, error accumulation coming from the intermediate local velocities are manifested in the incorrect prediction of the final penetration depth, $\delta(v)$, for a given entry velocity v .

In our analysis we have used the assumption that the force of retardation per unit mass, $F(v)$, during penetration of gelatin, can be expressed as a quadratic function of the projectile instantaneous velocity, v , i.e., $F(v) = \alpha v^2 + \beta v + \gamma$, where α , β , and γ are undetermined

coefficients. From previous reduction of experimental data it can be shown that α is related to the high velocity behavior of the penetration depth function, $\delta(v)$,

$$\delta(v)_{high} = a' \ln(v) + \frac{b'}{v} + \dots$$

where v is the entry velocity while γ is related to $\delta(v)$ at low velocities.

$$\delta(v)_{low} = v^2 (a + bv + cv^2 + \dots)$$

High velocity refers to about 90% of the maximum velocity of interest, v_{max} ($\sim 4,500$ ft/sec for MRC small spherical projectile penetration data) where $\delta(v)$ behaves like $\ln(v)$. Although, $\ln(v)$ is the first order and dominant term of the series at high striking velocities, $\delta(v)_{high}$, there are second order terms that include contributions from the linear and constant terms in the quadratic retardation force function. This is not the case for the low velocity behavior of $\delta(v)$ however. These results were established earlier from the exact functional relationship between $F(v)$ and $\delta(v)$, i.e., $\delta(v) = v/F(v)$ where prime indicates differentiation with respect to the argument v .

Using previously generated experimental data, the coefficients above have the following values for small spherical projectile penetration into 20% ordnance gelatin.

Low Velocity Coefficients

$$a = 5.13E-6$$

$$b = -2.84E-9$$

$$c = 5E-13$$

High Velocity Coefficients

$$a' = 1.2.61$$

$$b' = -7.67E3$$

Depending on the choice of v_{max} , the offset, δ_c , is constant and be estimated by writing the high velocity asymptote, $\delta(v)_{high}$, as $\delta(v) = \ln(v)/a - \delta_c$. In the following calculations, v is measured in ft/sec while lengths are measured in inches. From the penetration data on small diameter spherical projectile data into gelatins, δ_c is approximately 2 inches.

The β term cannot be directly inferred since it represents contributions from the various phases of the gelatin, which predominate at intermediate velocities. The following procedure, which can only be applied to the high velocity asymptote which include secondary contributions from other retardation terms, is therefore used to estimate β . For any given velocity, $v = v_H$; in the high velocity region of the parameter space, calculate:

$$a' \ln(v) - \delta(v_H) \Big|_{data} = \delta_c$$

This forces the parameter to fit: $a' \ln(v) - \delta_c$ for $v = v_H$.

The error, $E(\beta)$, for any given v_H can therefore be estimated from

$$E(\beta) = \int_0^{v_H} \frac{v dv}{F(v)} - [\alpha' \ln(v_H) - \delta_c]$$

Our objective is, to find β for a known α and γ such that the root of $E(\beta) = 0$. The coefficients of the retardation function have been estimated from the experimental data using two approaches.

Estimated values for α and γ using fits to the parametric forms of the high and low velocity

asymptotes are $\alpha = \frac{1}{\alpha'} = 0.793$ and $\gamma = \frac{1}{2\alpha} = 0.974E5$. Coefficients estimated from fitting a quadratic retardation function to the entire set of experimental data (which as discussed in previous progress reports yields poor estimates of penetration depth) results in the following coefficients (distinguished by the subscript "c").

$$\alpha_c = 0.8637 \quad \beta_c = 1408.68 \quad \gamma_c = 0.687E6$$

In both cases $v_{max} = 4500$ fps.

The first term in the expression for $E(\beta)$ above is identically equal to $\delta(v)$ as described in previous progress reports. Assuming a quadratic form of the retardation function, $\delta(v)$ can be integrated as follows.

$$\delta(v) = \frac{\ln\left(\frac{\alpha v^2 - \beta v + \gamma}{\gamma}\right)}{2\alpha} \Delta(\beta) + \frac{\beta}{\alpha \Delta(\beta)} \left[\arctan\left(\frac{2\alpha v - \beta}{\Delta\beta}\right) + \arctan\left(\frac{\beta}{\Delta\beta}\right) \right]$$

The first term in the expression above can be simplified to $\left(\beta^2 - 4\alpha\gamma\right)^{\frac{1}{2}}$.

Knowing that $E(\beta) = \delta(v) - \frac{\ln(v)}{\alpha} + \delta_c$ and using $\delta_c = 2$ inches which is the empirically observed offset from the logarithmic curve at high striking velocities, we can determine $E(\beta) = \beta$ as shown Figure 8.

The optimum β which minimizes the error term, $E(\beta) = 0$, is $\beta = -478.54$.

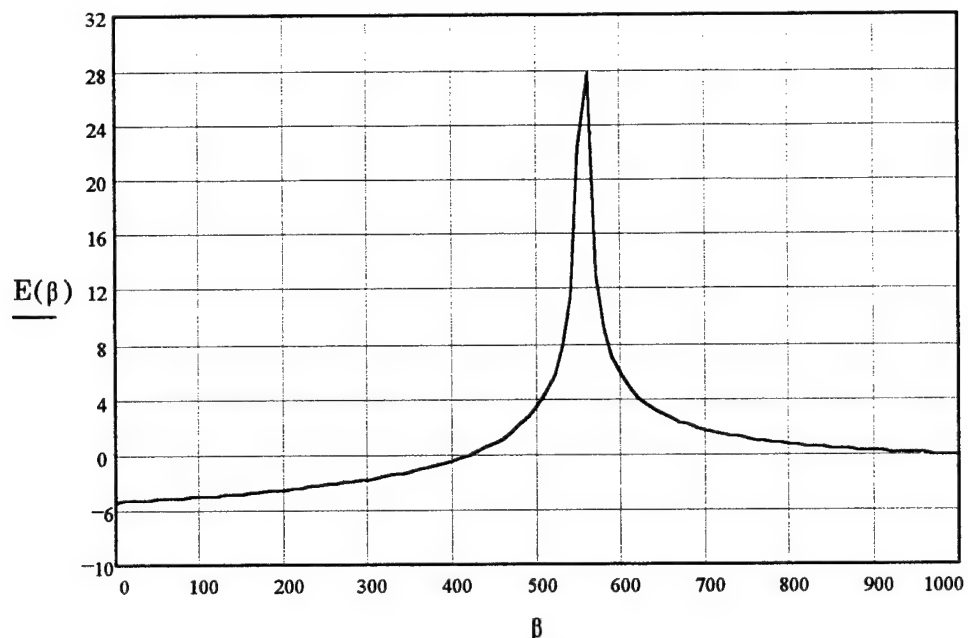


Figure 8. $E(\beta)$ versus β

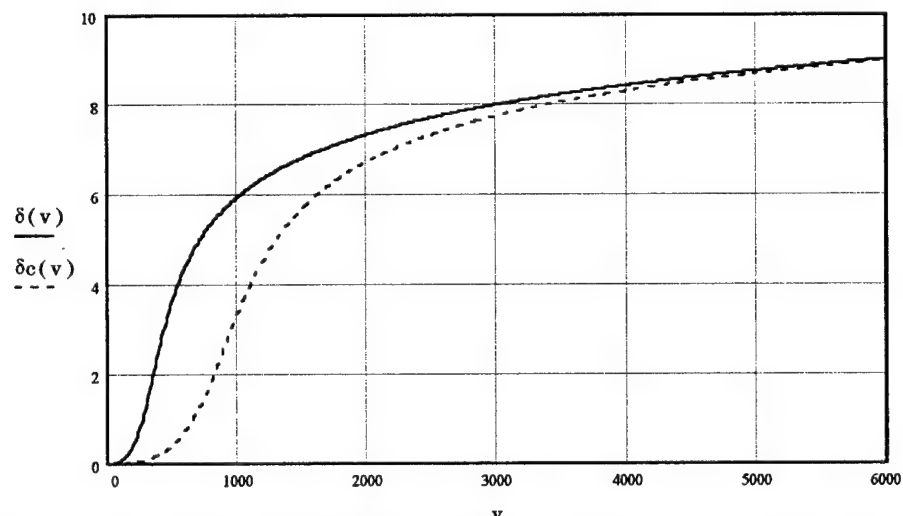


Figure 9. Comparison of Penetration Depth versus Striking Velocity using Empirical Fit to Quadratic Function versus Semi-Analytical Approach

Previous experimental data fit to a quadratic retardation function yields, $\beta_c = 1408.68$. A comparison between both approaches and estimated penetration depth is shown in 27 where discrepancies accrue for a significant portion of the intermediate velocities.

At high velocities both approaches agree with the data and each other, $\delta(4500 \text{ fps}) = 8.608 \text{ inches}$ and $\delta_c(4500 \text{ fps}) = 8.517 \text{ inches}$. To check the estimation procedure for β , the process was repeated to estimate β_c . For this case when $\alpha = \alpha_c$ and $\gamma = \gamma_c$ the results in Figure 10 are produced for $E(\beta_c)$ versus β_c , see Figure 10.

The actual root of $\{E(\beta), \beta\} = 0$ corresponds to $\beta = 1.415E3$. This compares to the empirically determined $\beta_c = 1.409E3$. This appears to corroborate the procedure to estimate coefficients of terms in the retardation function that predominate at intermediate velocities.

The next step in the analysis was to determine if there was continuity in the slope of the high and low velocity asymptotes and determine sensitivity of these slopes to the specific value of the coefficients. This is a more stringent requirement on the fidelity of the retardation function than simply ascertaining the coefficient of an assumed polynomial coefficient. In order to have continuity of the first derivative, the functional representation must be much more highly resolved. For low velocities where we assume a threshold velocity of $v_1 = 0.1v_{max}$:

$$c + bv_1 = \alpha v_1^2 + \beta v_1 + \gamma \quad (a)$$

$$b = 2\alpha v_1 + \beta \quad (b)$$

and for high velocities where we assume a threshold velocity of $v_2 = 0.9v_{max}$

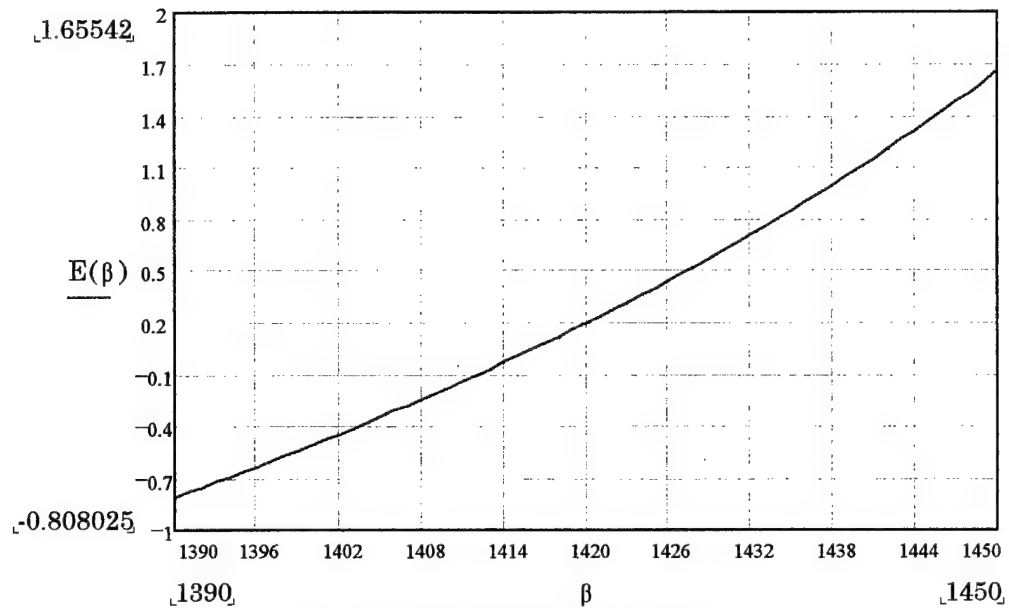
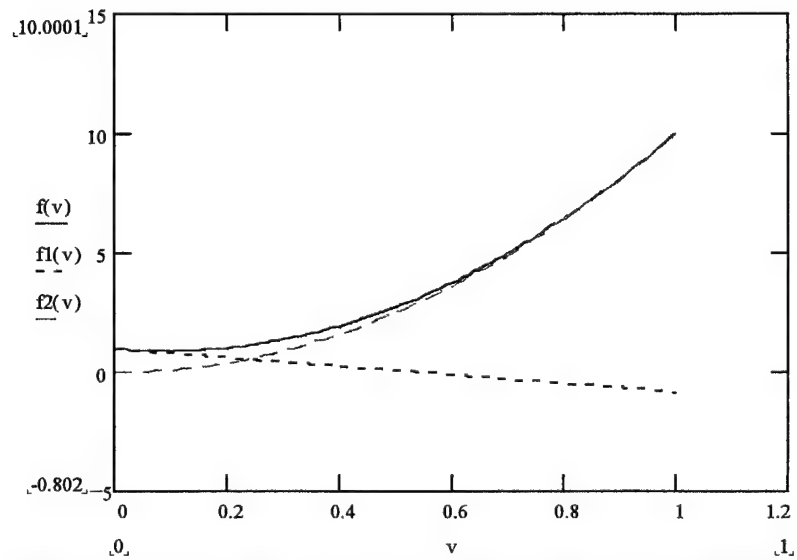
$$\alpha v_2^2 = \alpha v_2^2 + \beta v_2 + \gamma \quad (c)$$

$$2\alpha v_2 = 2\alpha v_2 + \beta \quad (d)$$

If we normalize the striking velocities to v_{max} i.e., $v_1 = 0.1$ and $v_2 = 0.9$ and assume an order of magnitude difference between α (= 10.0) and c (= 1.0) then the following applies.

$$A := \begin{bmatrix} v1^2 & v1 & 1 & -v1 \\ 2 \cdot v1 & 1 & 0 & -1 \\ v2^2 & v2 & 1 & 0 \\ 2 \cdot v2 & 1 & 0 & 0 \end{bmatrix} \quad A^{-1} = \begin{bmatrix} 1.25 & -0.125 & -1.25 & 1.125 \\ -2.25 & 0.225 & 2.25 & -1.025 \\ 1.013 & -0.101 & -0.012 & 0.011 \\ -2 & -0.8 & 2 & -0.8 \end{bmatrix}$$

$$\begin{bmatrix} \alpha \\ \beta \\ \gamma \\ b \end{bmatrix} := A^{-1} \begin{bmatrix} c \\ 0 \\ a \cdot v2^2 \\ 2 \cdot a \cdot v2 \end{bmatrix}$$

Figure 10. $E(\beta_c)$ versus β_c Figure 11. Retardation Function, $F(V)$, with Low and High Velocity Asymptotes

form which we can obtain:

$$\alpha = 11.375, \beta = -2.475, \gamma = 1.114, \text{ and } b = -0.2.$$

Re-doing this problem with threshold velocities assumed to be $v_1 = 0.01$ and $v_2 = 0.99$ result in:

$$\alpha = 11.021, \beta = -2.022, \gamma = 1.001, \text{ and } b = -1.802.$$

A plot of this retardation function with the low and high velocity asymptotes is shown in Figure 11.

2.1.1.10 Summary

Predicting the geometry of wound tracts in humans requires a retardation function that describes the velocity history of the projectile during penetration in human tissue. This velocity history is used as an initial condition to other models that describe tissue displacement normal to the wound tract. Since ballistic testing cannot be done on humans, ballistic testing is implemented on surrogate materials, which phenomenologically manifest behavior similar to what would be expected in human tissue. A model is then developed for the surrogate and assumed to have a functional form similar to human tissue. The model parameters however need to have rigorous physical interpretations so that they can be ascertained independent of a ballistic test. In our case we need to be able to quantify the model parameters based on tissue properties that are available.

The procedure discussed in this section enables the determination of β for known α and γ where α , β , and γ are coefficients in the polynomial representation of the retardation function. The retardation function describes the velocity history of the projectile during penetration and is an essential element of the methodology to predict the wound tract in humans. The quadratic term of the retardation function has been shown to be associated with the dynamic pressure produced by passage of the projectile and is significant at high velocities (see Figure 16). Given this interpretation, the only tissue property that is relevant for calculating this term in the retardation function is tissue density or specific gravity. Other properties that are relevant are associated with the projectile geometry and striking conditions. There is evidence to suggest that second order terms effects can be important, which is the reason for the offset, δ_c , from the logarithmic term in the plot of penetration depth versus striking velocity. These are all properties that can, for the most part, be determined independent of ballistic testing. This means we can fairly reliably predict the value of this model parameter applicable to human tissue.

Similarly, the constant term, γ , can be shown to be equal to $[\sigma_c A_p]/m_p$, where σ_c is a characteristic stress in the tissue, A_p is the projected area of the projectile, and m_p is the projectile mass. If we assume that the *characteristics stress* is the ultimate tensile strength of the target material, which in the case of gelatin is between 10 and 100 psi and low strain rates, for the ballistic testing that has been accomplished employing a 341 mg, 0.171 diameter steel ball, we obtain an estimate for γ that is somewhere between 0.4E5 and 0.4E6. Recall that this compares with $\gamma = 0.974E5$ based on calculations using $\delta(v)$ and $\gamma_c = 0.687E6$ using a quadratic fit.

The detailed quasistatic stress strain curve for the different formulations of gelatin can be compared with the differences in penetration depth observed at the low velocities. The detailed stress strain curve is also required for the transient response model. This model describes tissue displacement, strain, and stress normal to the wound tract. Fortunately, quasistatic stress strain data is available for many human tissues from fresh, unembalmed, cadavers. This would allow model parameters to be calculated for penetrating injuries in humans.

2.2 ROTATIONAL KINEMATICS OF A PROJECTILE INSIDE A VISCOELASTIC FLUID

Bodies penetrating a highly viscous material suffer retardation forces mainly originating from three fundamental sources. These are: (a) a dynamic pressure drag force which is usually proportional to the second power of the instantaneous velocity, v , of the contact point between the projectile and the target, (b) a viscous drag force proportional to the magnitude of v , and (c) a drag independent of v . The last term is basically the force needed to fracture the material in the appropriate mode.

From a dimensional point of view, independent dimensions of both v^2 and v can be found from the physical properties of the target and the projectile and hence any power of such non-dimensional groups can be deemed to influence the a or b retardation terms. Obviously, the simplest function of these non-dimensional groups is a linear function of the form $av^2 + bv + c$ where a , b , and c are constants depending on the size, shape and other material properties of the projectile and the target. Determination of these constants for a specific case is however extremely difficult since the general motion of the projectile is at least two-dimensional where the projectile center of mass moves with a superposed motion about its center of mass.

For some applications, extensive experiments have been conducted to determine the depth of penetration as a function of the incident velocity of the projectile for specific combinations of targets and projectiles. These experiments are useful since such data can be directly inverted to obtain the functional form of the force of retardation on the motion of the center of mass. Since the motion of the center of mass depends only on the vector sum of all the forces acting on a rigid body, we can use this information to estimate the force on a point mass moving in the same media when the instantaneous velocity of the point mass is known. Using this concept, a mathematical model was developed which describes the two-dimensional motion of projectile inside the target when the initial conditions are prescribed. This motion is divided into two parts; motion of the center of mass and the motion about the center of mass. Since the order of these two motions is immaterial for a rigid body, these two motions completely determine the location of the projectile inside the target as a function of time.

The motion of the center of mass (CM) of a projectile entering a target can be calculated by integrating the differential equation of motion in the velocity-distance space under the assumption that the coefficients a , b , c in the retardation force-velocity relation are known from experimental or theoretical calculations. These coefficients represent average values that are capable of predicting the motion of the CM only. To extend the results to full two-dimensional prediction of projectile motion inside a target, we need to make some assumptions.

One of the most important assumptions is that in the current mathematical formulation, the associated coefficients are also capable of estimating the force of retardation on a point mass moving inside a target. If this is true, then a rigid body may be conceived as an ensemble of particles where the retardation force on each particle is known, and hence, the equations of motion governing motion about the CM can be written down. If we ignore the frictional drag on these particles, then the resistive force can be calculated by the same functional form shown above except that v should be replaced by the normal component of the velocity of a particle

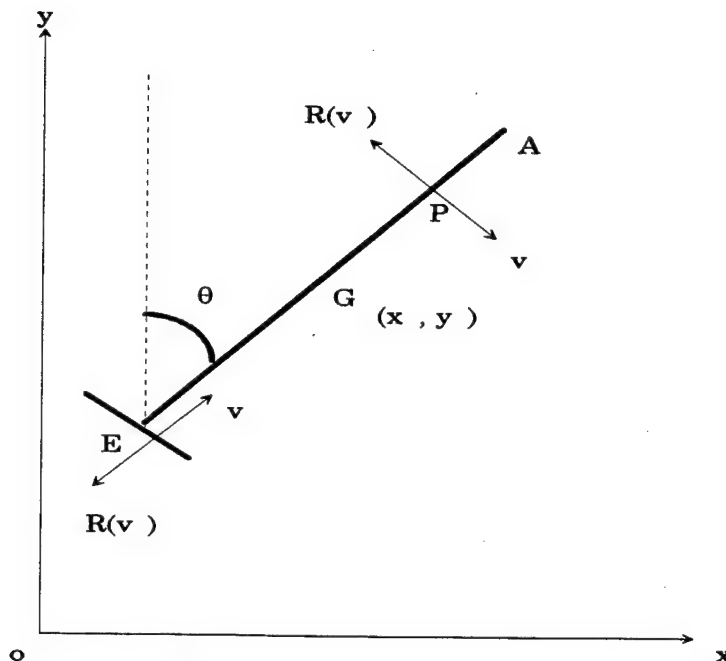


Figure 12. Projectile location and loading at time t

mass on the projectile. Here the normal direction is defined by the outward normal direction at the projectile surface.

Assuming that the **force of retardation $R(v)$ per unit mass** on each of these collection of particles constituting the projectile, we can write $R(v)$ as

$$R(v) = av^2 + bv + c \quad (13)$$

where the v is the normal component of the velocity as described above. The distribution of these forces on the body and fin area of a flechette is shown in Figure 12.

At any given time t , let $[x_G(t), y_G(t)]$ and $\theta(t)$ be the coordinates of the center of mass G of the projectile and the angular coordinate defining the inclination of the projectile body with the y -axis. These coordinates completely specify the location of the projectile at time t . In order to determine these coordinates; we need to use the equations of motion of and about the CM . Since the motion of the CM is governed by a corresponding particle mass problem where the mass of the particle is equal to the mass of the flechette and all the forces on the flechette are assumed to pass through the CM , we have the following equations of motion for the projectile CM .

$$m\ddot{x}_G = - \int_{-l}^l \rho R(|v_{pn}|) \operatorname{sgn}(v_{pn}) \cos \theta dr - m_f R(|v_{en}|) \operatorname{sgn}(v_{en}) \sin \theta \quad (14)$$

$$m\ddot{y}_G = + \int_{-l}^l \rho R(|v_{pn}|) \operatorname{sgn}(v_{pn}) \sin \theta dr - m_f R(|v_{en}|) \operatorname{sgn}(v_{en}) \cos \theta$$

The equation of motion about the *CM* can be obtained by taking moments of the equations of motion of the ensemble of particles constituting the projectile, about the *CM*. This yields

$$I_G \ddot{\theta} = - \int_{-l}^l \rho R(|v_{pn}|) \operatorname{sgn}(v_{pn}) r dr \quad (15)$$

In Equations 14 and 15, ρ is the mass of the projectile per unit length, r is measured from the *CM* (Figure 12), m_f is the mass of the base of the projectile, $2l$ is the projectile and I_G is the moment of inertia of the projectile about its *CM*. R is the force of retardation per unit mass for the particle mass problem.

The velocity of a particle P at a distance r from the *CM* in the direction normal to the flechette body can be expressed in terms of the velocity components of the *CM* in the x - and y -directions and angular velocity $\dot{\theta}$, as

$$v_{pn} = r\dot{\theta} + \dot{x}_G \cos \theta - \dot{y}_G \sin \theta \quad (16)$$

Using Equations (13) and (16), R can be written as in terms of the retardation coefficients a , b , c as

$$R(|v_{pn}|) = (a\dot{\theta}^2)r^2 + (2aA \pm b)\dot{\theta}r + (aA^2 \pm bA + c) \quad (17a)$$

$$\text{where } A = \dot{x}_G \cos \theta - \dot{y}_G \sin \theta \quad (17b)$$

Similarly, $R(|v_{en}|)$ is given by

$$R(|v_{en}|) = aB^2 \pm bB + c \quad (18a)$$

$$\text{where } B = \dot{x}_G \sin \theta + \dot{y}_G \cos \theta \quad (18b)$$

Substituting Equations 17 and 18 into Equations 14 and 15, and integrating, it follows that

$$\begin{aligned} (m_b + m_f)\ddot{x}_G &= -\frac{m_b}{2l}\Gamma_1 \cos \theta - m_l\Gamma_2 \sin \theta \\ (m_b + m_f)\ddot{y}_G &= -\frac{m_b}{2l}\Gamma_1 \sin \theta - m_l\Gamma_2 \cos \theta \\ I_G \ddot{\theta} &= -\frac{m_b}{2l}\Gamma_3 \end{aligned} \quad (19)$$

In (19), Γ 's are defined as

$$\begin{aligned}
 \Gamma_1 &= a\dot{\theta}^2 I_{A,B}^{(2)} + 2A\dot{\theta}I_{A,B}^{(1)} + (aA^2 + c)I_{A,B}^{(0)} + 2lbA \\
 \Gamma_2 &= (aB^2 + c)\operatorname{sgn}(B) + bB \\
 \Gamma_3 &= a\dot{\theta}^2 I_{A,B}^{(3)} + 2A\dot{\theta}I_{A,B}^{(2)} + (aA^2 + c)I_{A,B}^{(1)} + \frac{2}{3}bl^3\dot{\theta}
 \end{aligned} \tag{20}$$

For the projectile, I_G is given by $I_g = \frac{1}{3}m_b l^3 + m_f l^2$

In (20), $I_{A,B}^{(n)}$, $n = 0, 1, 2, 3$ are integrals that keep track of load reversal due to the change in the location of the instantaneous center of rotation. In order to explain the cause of this load reversal, the expression that calculates the normal component, v_{pn} , of velocity (see Figure 12) needs to be considered. As shown earlier, v_{pn} is given by (16). To find the regions of positive v_{pn} , the following four cases may occur depending on the relative values and signs of A and $\dot{\theta}$. With reference to Figure 12, v_{pn} is positive in the following regions.

$$\begin{aligned}
 1. \quad & r_1 \left(= -\frac{A}{\dot{\theta}} \right) < r < l, \text{ for } A < 0, \dot{\theta} > 0 \\
 2. \quad & -r_2 \left(= \frac{A}{\dot{\theta}} \right) < r < l, \text{ for } A > 0, \dot{\theta} > 0 \\
 3. \quad & -l < r < r_1 \left(= -\frac{A}{\dot{\theta}} \right) < r < l, \text{ for } A > 0, \dot{\theta} < 0 \\
 4. \quad & -l < r < -r_2 \left(= \frac{A}{\dot{\theta}} \right) < r < l, \text{ for } A < 0, \dot{\theta} < 0
 \end{aligned} \tag{21}$$

With the above definitions of r_1 and r_2 , the integrals I can be expressed as

$$\begin{aligned}
 I_A^{(n)} &= m_1 \int_{-l}^{-r_2} r^n dr + m_2 \int_{-r_2}^l r^n dr \\
 &= \frac{l^{n+1}}{n+1} (m_2 + (-1)^n m_1) + \frac{r_2^{n+1}}{n+1} (-1)^{n+1} (m_1 - m_2) \\
 I_B^{(n)} &= m_1 \int_{-l}^{r_1} r^n dr + m_2 \int_{r_1}^l r^n dr \\
 &= \frac{l^{n+1}}{n+1} (m_2 + (-1)^n m_1) + \frac{r_1^{n+1}}{n+1} (-1)^{n+1} (m_1 - m_2)
 \end{aligned} \tag{22}$$

In Equation 22, m_1 and m_2 are either $+1$ or -1 and defined as follows. For the $I_A^{(n)}$ integral (i.e., when r_1 is feasible which corresponds to cases 2 and 4 of Equation 21), $m_1 = -\operatorname{sgn}(A)$ and

$m_2 = \text{sgn}(\dot{\theta})$. Similarly, for the $I_B^{(n)}$ integral (cases 1 and 3 of Equation 21), $m_1 = \text{sgn}(A)$ and $m_2 = -\text{sgn}(\dot{\theta})$. These integrals keep track of the reversal of the retardation forces when the location of the instantaneous center of rotation changes dynamically with the relative values of A and $\dot{\theta}$.

Equations 19 through 22 completely determine the two-dimensional motion of the projectile. These equations are coupled, nonlinear, second order differential equations that have *no closed form solutions*.

2.2.1 Initial Conditions

To solve the system of differential equations above, initial conditions specifying the location of the center of mass, G , and the inclination of the projectile at time, $t = 0$, need to be defined. The initial velocity (\dot{x}_G, \dot{y}_G) of the CM and the angular velocity, $\dot{\theta}$, of the projectile also need to be specified.

When the initial conditions above are specified, the differential equations of motion, Equations 21 and 22, can be solved using a fourth order Runge-Kutta numerical integration routine.

2.2.2 Motion of a Partially Embedded Flechette inside a Target

Equations 14 through 22 describe the motion of a projectile that is fully embedded in a target at all times. However, prior to full penetration, the projectile undergoes a phase of partial penetration. During this phase, the limits of the integrals in Equation 14 should be replaced by proper limits that define the part of the projectile inside the target. Other than these changes, the methodology used above are applicable for the initial phase of partial penetration prior to the problem of the fully embedded projectile moving in a target discussed above.

2.3 ANALYSIS OF PROJECTILE INTERACTION WITH SOFT TISSUE

2.3.1 Determination of Temporary and Permanent Cavities and Nonlinear Spring-Mass Model

We have developed a computer code that calculates the transient response of an elastic medium due to a moving projectile. This problem is solved by simulating the actual physical problem of determining the transient response of a medium when ballistic penetration takes place. This problem is solved by the superposed response of properly distributed transient point sources. We have used the fundamental Green's function solution for a *transient, stationary* point source with an arbitrary temporal distribution as the building block for the desired solution. The fundamental solution has three terms each signifying the response for various time periods at a given point inside the medium. Physically, the mathematical solution represents the sum of the near field solution, far field P-wave and far field S-wave solutions. The desired solution of the above problem is then constructed from this fundamental solution by properly distributing a series of sources along the penetration path of the projectile. The temporal distribution for each of these transient sources has a support function that is equal to the travel time of the moving projectile from one source location to the next one. Adjusting the spacing between the point sources tests solution convergence. From our earlier results on the nature and magnitude of the drag forces when the instantaneous velocity of the projectile is known, the intensity of a particular source is calculated as a function of location and time. The intensity depends on the velocity of the projectile when it is passing through the transient point source location.

2.3.2 Calculation of Transient Response of a Target and Temporary Cavity due to a Penetrating Object using a Moving Force of Variable Intensity Formulation

When a projectile of small size e.g., a bullet penetrates a gelatin or similar highly viscous material, the trailing path of the projectile may partially or almost fully close due to material settling. The response at a given point Q inside the target is very complicated due to the nonlinear field equations and temporal boundary conditions. The current state of the art is represented by a BRL model² that assumes that such moving source produces spherically symmetric waves emanating from its instantaneous location so that the total impulse any given point Q (Figure 13) is given by the integral

$$\text{Impulse at } Q = \int_0^{z_0} P(z) \frac{e^{-\frac{R}{\lambda}}}{R} dz \quad (23)$$

From our analysis using a moving point source formulation, it is evident that the BRL model is simply a far field point source solution where a viscoelastic damping term is added in the form of the exponential product, $e^{-\frac{R}{\lambda}}$, in the integrand in Equation 23. This model suffers from the following deficiencies:

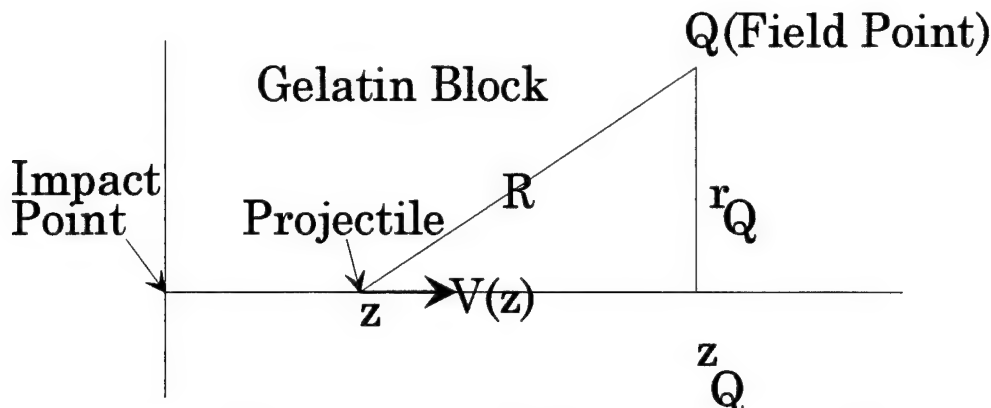


Figure 13. Schematics of BRL Calculation of Pressure Field

- A spherical radiation pattern assumed,
- The Force intensity is not an explicit function of projectile velocity, and
- Only far field P-wave response is considered.

2.3.3 Spherical Radiation Pattern

The loading on the target due to a penetrating projectile in a specified direction is opposite to the retardation force that the projectile experiences during its motion. For an elastic medium, the radiation pattern from such a directive force can be calculated from the corresponding Green's function in the medium and is shown in Figure 14. This radiation pattern is significantly different from the spherical wave radiation pattern used in the above BRL model, especially behind the projectile since the displacement has opposite signs in these two models.

2.3.4 Force Intensity Dependence on Instantaneous Projectile Velocity and Target Properties

In the development of our models to analyze penetration history, we concluded that the force of

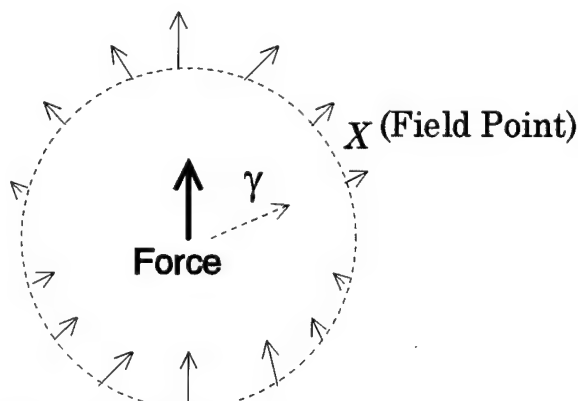


Figure 14. Radiation Pattern due a Point Force

retardation depends on the instantaneous speed, v , of the projectile. The magnitude of the retardation force can be approximately calculated from a second order polynomial in v of the form av^2+bv+c where a , b and c are dependent on the properties of the target and the projectile.

2.3.5 Far Field P-wave Response

This follows from our moving force model described below. With reference to Figure 15, let the location of the projectile at any given time t be described by the function: $x=l(t)$. Behind the projectile, the penetration path is composed of partially open and fully closed material. The effect of the open penetration path introduces additional perturbation in the medium due to a vanishing stress field at these locations. We do not know at this point how much influence such a perturbed field produces at a given field point. To estimate that, we first assume that the penetration path closes completely after its passage. If we ignore any effect of any finite boundaries the response of the medium can now be calculated from the Green's function due to a time varying point force in the direction of the projectile located at its instantaneous position. The physical model is described in Figure 15.

The fundamental assumptions of this model are described below:

1. A moving load of known intensity is assumed along the x -axis
2. The force intensity is a known function of the velocity v in the form av^2+bv+c where the constants a , b , c depend on the target and projectile properties.
3. The force location $x=l(t)$ is a known function of time t .

Assumptions in 2 and 3 follow from the retardation models developed in previous sections.

2.3.6 Calculation of Transient Response due to an Applied Force

The displacement at a point x at time t due to a point force at the origin at time $t = 0$ in an infinite medium is given by the sum of the following three terms:

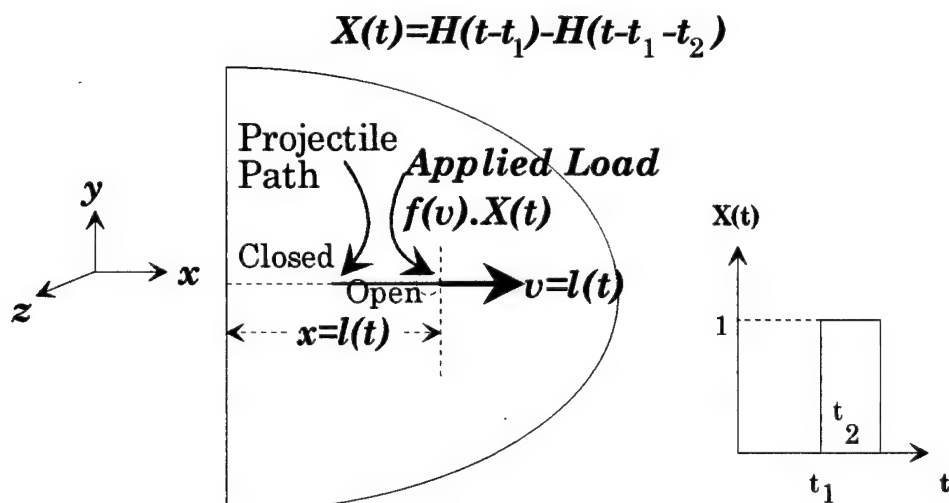


Figure 15. Schematic of MRC Model of Moving Point Source

$$\begin{aligned}
 1. \text{ Near Field Response: } u_i(\bar{x}, t) &= \frac{3\gamma_i\gamma_j - \delta_{ij}}{4\pi\rho r^3} \int_{\frac{r}{\alpha}}^{\frac{r}{\beta}} \tau X(t - \tau) d\tau \\
 2. \text{ Far Field P-wave Response: } u_i(\bar{x}, t) &= \frac{\gamma_i\gamma_j}{4\pi\rho\alpha^2 r} X(t - \frac{r}{\alpha}) \\
 3. \text{ Far Field S-wave Response } u_i(\bar{x}, t) &= \frac{\gamma_i\gamma_j - \delta_{ij}}{4\pi\rho\beta^2 r} X(t - \frac{r}{\alpha}) \tag{24}
 \end{aligned}$$

Closure of penetration path immediately after projectile pass is assumed. Effects of non-closure will be later added as a perturbation to the above solution.

2.3.7 Calculation of the Transient Cavity due to Projectile Penetration

The mechanics of projectile penetration can be described by considering the target as a three-dimensional network of molecular bonds between atoms. When a projectile penetrates a target, it severs molecular bonds between particles behind the projectile while the particles ahead of the projectile experience high pressures. The radiation pattern of these pressure waves is not spherical in shape, but rather is highly directive due to the penetration-induced directive loading on the target. The shape of the near- field and far-field radiation pattern for this directive loading is very similar those given by the Equations 24 even though these equations are in theory valid in an infinite medium with no fracture induced free surface present.

The transient cavity is formed when these pressure waves try to displace target material away from the fracture region while no molecular resistance to such motion is offered from the fractured region through which the projectile has passed. Thus, at any instant in time, the target material manifests various stress distributions along with new stress-free surfaces. The boundary of the transient cavity can therefore be calculated from the locus of zero-pressure near the projectile path. We denote this surface by *transient cavity boundary 1* or *tcb1*.

According to the model used in the BRL analysis employing a spherical radiation pattern, the boundary of the transient cavity is a locus of critical pressure points in the target at any given point in time. We call this surface as the *transient cavity boundary 2* or *tcb2t*. The difference in the transient cavity prediction can be schematically shown in Figure 16. Since the pressure is zero on *tcb1*, by definition, and is again zero at distances far from the fracture region, the variation of pressure will have distribution similar to that shown in Figure 16.

In the comparison with the BRL predicted *tcb2* and MRC's *tcb1*, we have used three of the cases for which experimental data are available. These are solid steel spheres penetrating 20% ordnance gelatin at speeds of 614, 783 and 984 ft/sec respectively. These spheres have a 0.635-cm diameter. Since we have assumed in our analysis that the path of penetration closes after the passage of the spheres, the lateral displacement is zero along the penetration path of the

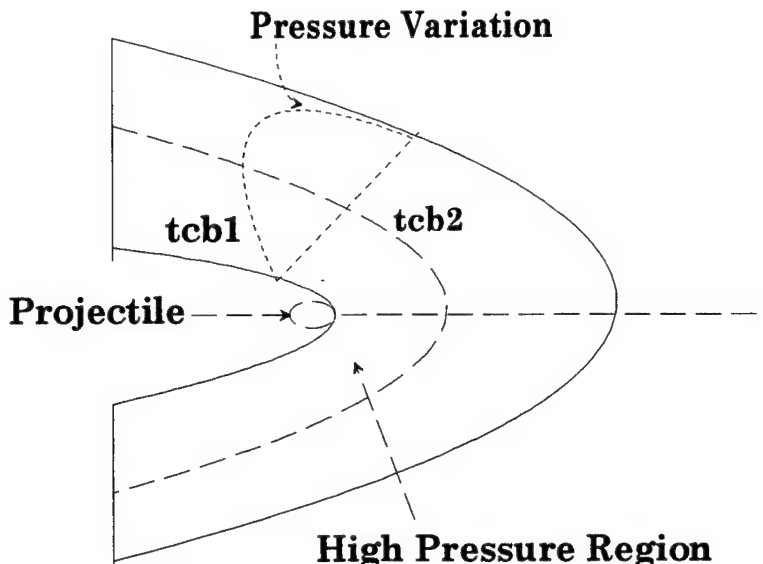


Figure 16. Pressure Distribution during Projectile Penetration

projectile. For the calculation of $tcb1$, we need to determine the displacement of the fractured particles that are situated along the trajectory of the spherical projectiles.

We know that the lateral displacement is zero on the penetration path as well as at distances far from the penetration path (radiation condition). Thus, it should assume a local maximum at some distance from the penetration path (Figure 16). We can then calculate the maximum lateral displacement for a given location along the projectile path for various values of the lateral coordinate. As expected, this maximum occurs very close to the penetration path. To reduce the singularity-induced instability (Equation 24 for small r) in our calculation, we exclude a small region near the point source for which the contribution at a given field point is calculated. The pulse width for each point source is taken to $\Delta t = 1\mu\text{s}$ while the radius of the excluded zone is taken to be $\beta\Delta t$ where β is the shear wave speed in the target. The calculated results are then scaled to correspond to the projectile size since the formulation used in the analytical model corresponds to a moving point force in the target medium. The retardation coefficients used in the MRC developed penetration model, corresponds to the small sphere data obtained from correlation with MRC generated experimental data on the penetration depths of these spheres in 20% ordnance gelatin targets. These coefficients are, in cgs units,

$$\begin{aligned}a &= 0.227 \text{ (cm}^{-1}) \\b &= -1.126 \times 10^4 \text{ (sec}^{-1}) \\c &= 1.675 \times 10^3 \text{ (cm/sec}^2)\end{aligned}$$

The problem of penetration of a target by high velocity projectiles can be divided into two problems. First, we need to know the characteristics of the retarding force acting on the projectile and then we also need to calculate the target response due to projectile penetration. Experimental data from ballistic testing described in Section 3 has been implemented for different formulations

of ordnance gelatin targets. These data show the distribution of projectile penetration depth as a function of striking velocity. An analytical inversion process has converted these data to determine the distribution of the retarding force as a function of instantaneous projectile velocity inside the target. The distribution of the retarding force yields excellent agreement with the experimentally observed projectile velocity history inside the target.

Let us now look at the problem of the target response due to the projectile penetration. Physically, this involves the determination of the temporary transient cavity formed behind the projectile as well as the final long term cavity known as permanent cavity along the penetration path of the projectile after the target comes to rest. The second problem requires the knowledge of the viscoelastic characteristics of the target.

To solve the first problem by direct mathematical modeling of the actual problem, we should consider the response of a viscoelastic medium due the penetration of a projectile with variable velocity of penetration. The temporal character of the velocity of penetration is assumed to be known *a priori*. Thus, the full form mathematical model is a three-dimensional model with axial symmetry along the penetration path. The penetration path should be a stress free surface for the model. The only forcing function in the target medium is the force exerted by the projectile at its instantaneous location. This driving force is also assumed to be known since this force is exactly equal and opposite to the force of retardation experienced by the projectile. The resulting problem can now be approximately solved, at least numerically, by using the full three dimensional form of the representation theorem of linear elastic theory for the transient part of the response and then using viscoelastic theory to calculate the permanent cavity diameter.

Some first and second order estimates of the transient target response can be obtained by simplifying the problem by eliminating some of the aspects of the full three-dimensional problem. These models along with their limitations are discussed below:

2.3.8 Three dimensional Target Response under the Assumption of Crack closure

If we assume that the path behind the projectile closes right after the passage of the projectile, then we can get the target response by superposing the solution of the appropriate Green's functions for point sources of known intensities along the path of the projectile. These Green's function have two parts; one describes the response at a point inside the target when the P-wave radiated from the source arrives at the location and the other one comes from the S-wave passage through this point. Each of these responses has their near and far field representations. These Green's function solutions need to superpose with proper time shifts to incorporate the moving source associated with the projectile motion. The intensities also are time dependent since they represent the intensity of the force that is a function of the instantaneous velocity of the projectile at the source location. The shortcoming of such a simplified model response is that the lateral displacement will be zero on the projectile path (due to the symmetry of the problem with respect to the line of penetration) as well as zero at large distances from the sources due to the decay of the radiated fields with distance. For the original problem, the displacement should be maximum along the penetration path. Since the reduced problem has a local maximum at a point away from the penetration path, we can extrapolate the transient cavity radius from such simple models.

2.3.9 Response of the Target due to a Two-dimensional Crack Moving with Known, Variable Velocity:

If only the early response of the target is of importance, we may assume that the crack formed by the projectile penetration is a two dimensional surface because the radiation from the other stress free surface away from the path of the projectile will contribute to the late time response of the target. Here again we assume that the stress ahead of the crack tip is known i.e., the stress intensity factor ahead of the crack tip is assumed to be known as a function of the instantaneous velocity of the projectile. The response of the target can now be obtained from the descritized version of the representation theorem for such a problem. The shortcoming of this two-dimensional crack model is that the late time response of the modified function has a long tail while the original problem has a much faster decay in time.

Once the analysis of the results from these two simplified models are complete, we will be able to understand the physics of the full problem more clearly, and then solve the full three-dimensional problem described above if such solutions are warranted for better correlation of the experimental data and theoretical analysis.

2.3.10 Reduction of three-dimensional inhomogeneous material distribution to an equivalent non-linear mass-spring system

In the determination of mechanical response of parts of bodies due to impact or other similar loading, it is currently conceived that it is possible to replace the relevant part of the body by an equivalent mass spring system. There are obviously some questions that need to be addressed before such idealization is useful. For a given body part the main issues with this approach are discretization of the mass particles that preserves proper mass distribution inside the body as well as the conservation of mass for the given body, and the determination of the equivalent spring constants.

Since the two critical parameters in the mass-spring model of a given body part are the particle mass distribution and the equivalent spring constants connecting these mass particles, we looked at some of the fundamental issues associated with their description. Discretizing the given bodies mass into particle masses is not a problem. In a three-dimensional scenario, if we divide a given body into voxels, any mass element inside a cube can be decomposed into eight equal particle masses at the corners of the elements. Summing all the particle masses at any cube corner from all the adjacent elements, we get the equivalent particle mass for that point.

The calculation of the spring constant for the equivalent mass-spring system is not that simple. The complexity comes from the ways the inhomogeneities inside a cube element are distributed. If we assume that all components of a body part have known properties, each component can be assigned to a known nonlinear description of force-displacements relations. If two of these elements are stacked in parallel, then we can calculate the equivalent spring constants in the following way. Let us assume that two different elements are situated in parallel inside a cube element. Then, under a given force F if u is the displacement of the element, then

$$\begin{aligned}
 F_1 &= k_1 u + c_1 u^2 \\
 F_2 &= k_2 u + c_2 u^2 \\
 F &= \bar{k} u + \bar{c} u^2 = F_1 + F_2
 \end{aligned} \tag{25}$$

This gives the equivalent spring constants \bar{k}, \bar{c} in terms of the individual spring constants k_1, c_1 and k_2, c_2 as $\bar{k} = k_1 + k_2, \bar{c} = c_1 + c_2$.

For nonlinear springs in series, such a description is not possible simply because F can not be written in terms of $u = u_1 + u_2$ alone. This necessitates the imposition of critical constraints so that a given cube can not contain two different material types in series. If this is not possible, then the inverse relations between the equivalent spring properties and individual spring properties should be used even though they do not exactly satisfy the required kinematic relations. If this is done, then an error estimate should be obtained to give some credibility to the solution.

As previously mentioned, the penetration problem by high velocity projectiles can be divided into two sub-problems. First, we need to know the characteristics of the retarding force acting on the projectile and then we also need to calculate the target response due to projectile penetration. We can analytically invert ballistic data relative to projectile penetration depth as a function of striking velocity to determine the retarding force acting on the projectile as a function of the instantaneous projectile velocity inside the target.

Let us now look at the problem of the target response due to the projectile penetration. Physically, this involves the determination of the temporary transient cavity formed behind the projectile as well as the final long term cavity known as permanent cavity along the penetration path of the projectile after the target comes to rest. The second problem requires the knowledge of the viscoelastic characteristics of the target.

To solve the first problem by direct mathematical modeling of the actual problem, we should consider the response of a viscoelastic medium due the penetration of a projectile with variable velocity of penetration. The temporal character of the velocity of penetration is assumed to be known *a priori* since we have already shown the method of solution for such velocity histories. Thus, the full form mathematical model is a three-dimensional model with axial symmetry along the penetration path. Besides, the penetration path should be a stress free surface for the model. The only forcing function in the target medium is the force exerted by the projectile at its instantaneous location. This driving force is also assumed to be known since this force is exactly equal and opposite to the force of retardation experienced by the projectile. The resulting problem can now be approximately solved, at least numerically, by using the full three dimensional form of the representation theorem of linear elastic theory for the transient part of the response and then using viscoelastic theory to calculate the permanent cavity diameter.

Some first and second order estimates of the transient target response can be obtained by simplifying the problem by eliminating some of the aspects of the full three-dimensional problem.

2.3.11 Selected Model Results

Figure 17 shows predicted scaled displacement versus scaled time for permanent and temporary cavities using a quadratic model for the spring stiffness. The governing equation of motion is given below.

$$m \frac{d^2x}{dt^2} = -[K_1 x + K_2 x^2] = -\left[\frac{K_1}{m} x + \frac{K_2}{m} x^2 \right] = -[\bar{K}_1 \bar{x} + \bar{K}_2 \bar{x}^2]$$

The displacement is given by the parameter, x ; m , t , and K_i represent the lumped mass, time, and stiffness of spring i , respectively. We assume:

$x_s = \frac{\bar{K}_1}{\bar{K}_2}$ and $t_s = \frac{x_s}{v_0}$ where v_0 is initial velocity; then, $\bar{x} = \frac{x}{x_s}$ and $\bar{t} = \frac{t}{t_s}$ where \bar{x} and \bar{t} are the non-dimensional scaled parameters.

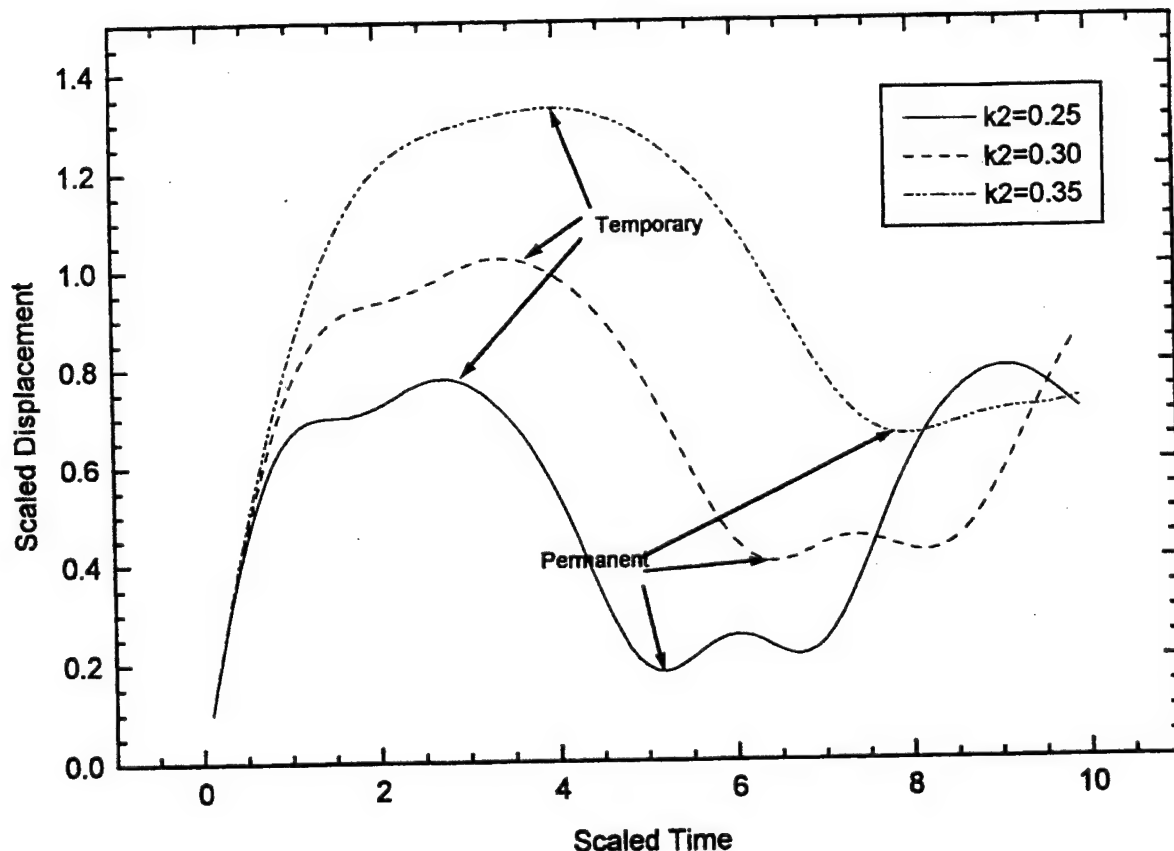


Figure 17. Effect of Energy Absorption on Temporary and Permanent Cavity

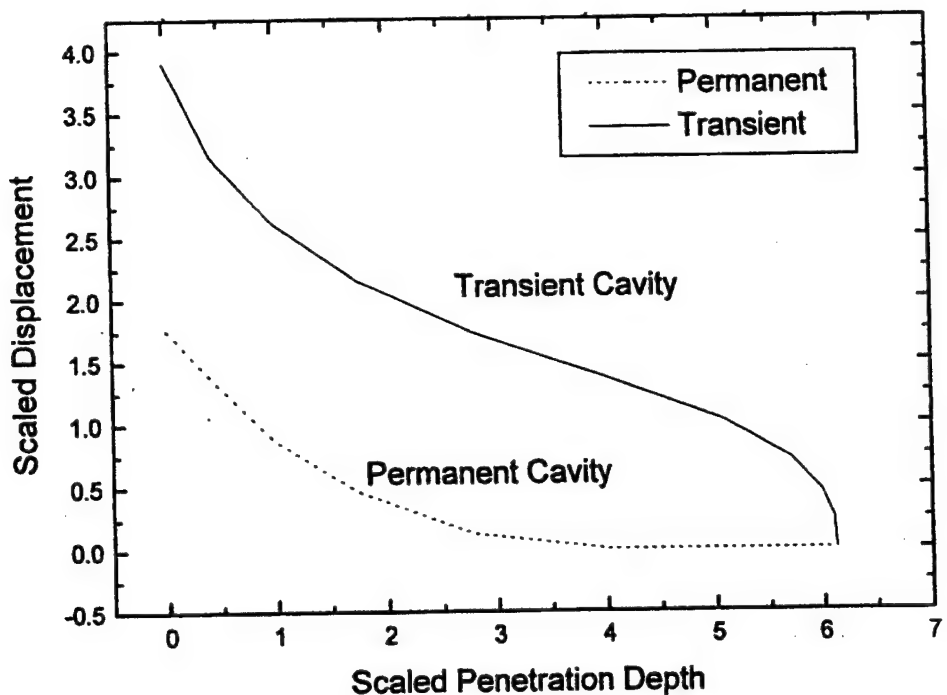


Figure 18. Cavities at Various Penetration Depths for Non-Linear Spring Model with Three Particles ($K_1 = 1.0$ and $K_2 = 0.35$)

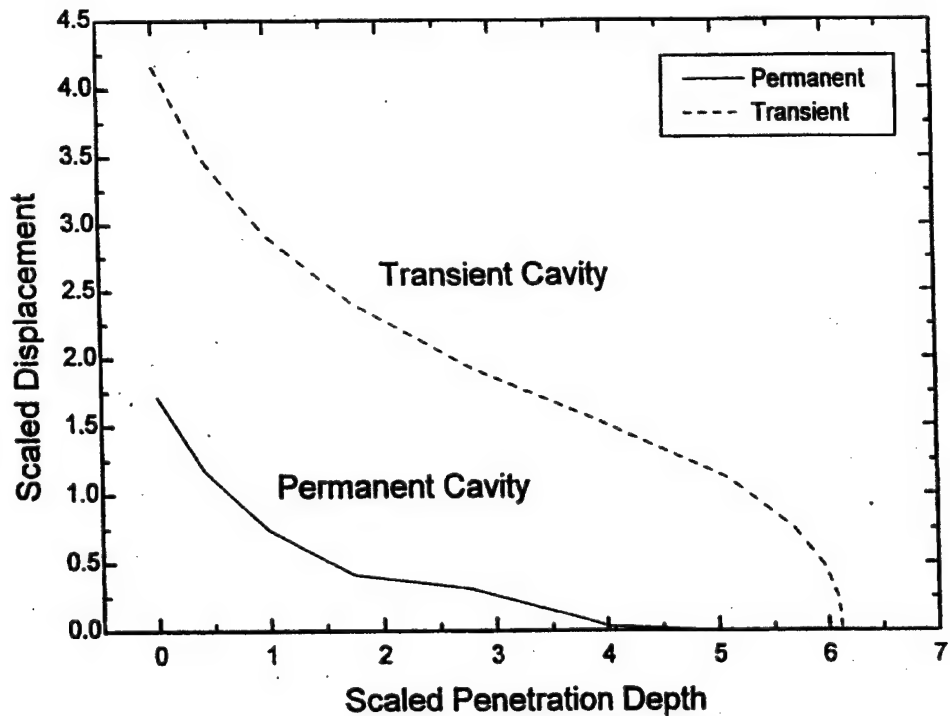


Figure 19. Cavities at Various Penetration Depths for Non-Linear Spring Model with Five Particles ($K_1 = 1.0$ and $K_2 = 0.35$)

Figure 18 and Figure 19 shows transient and permanent cavity displacement versus penetration depth for identical non-linear spring models but where the lumped mass has been discretized into 3 and 5 particles. Figure 20 shows the "affected zone" superimposed on Figure 19. The affected zone is established by identifying those areas beyond the permanent cavity where a hysteresis or inelastic strain accumulates. A hysteresis effect is illustrated in Figure 21.

A typical tissue stress-strain curve is shown in Figure 21. The projectile impact results in the material being loaded up to point *A* in Figure 21. When elastically unloaded to point *B*, a residual strain or hysteresis effect is evident. The affected zone in Figure 20 is established by examining each spring in the lattice (see Figure 35 and associated discussion regarding non-linear spring-mass lattice, all Appendix A) to determine where a non-zero residual strain exists. If the initial part of the stress-strain curve were linear, as is usually the case, then for sufficiently small-imposed loads, unloading would result in return a zero residual or initial strain condition. It is only when the load extends into the concave portion of the stress-strain curve and then elastically unloaded that a hysteresis effect is evident.

Figure 22 shows, as a function of penetration depth, the size of the temporary cavity for a 344 mg, 0.171 inch diameter steel sphere striking 20% ordnance gelatin at 1667 feet per second. The plot shows predictions using different discretization schemes where, particularly at low velocities, it is seen that convergence is very fast.

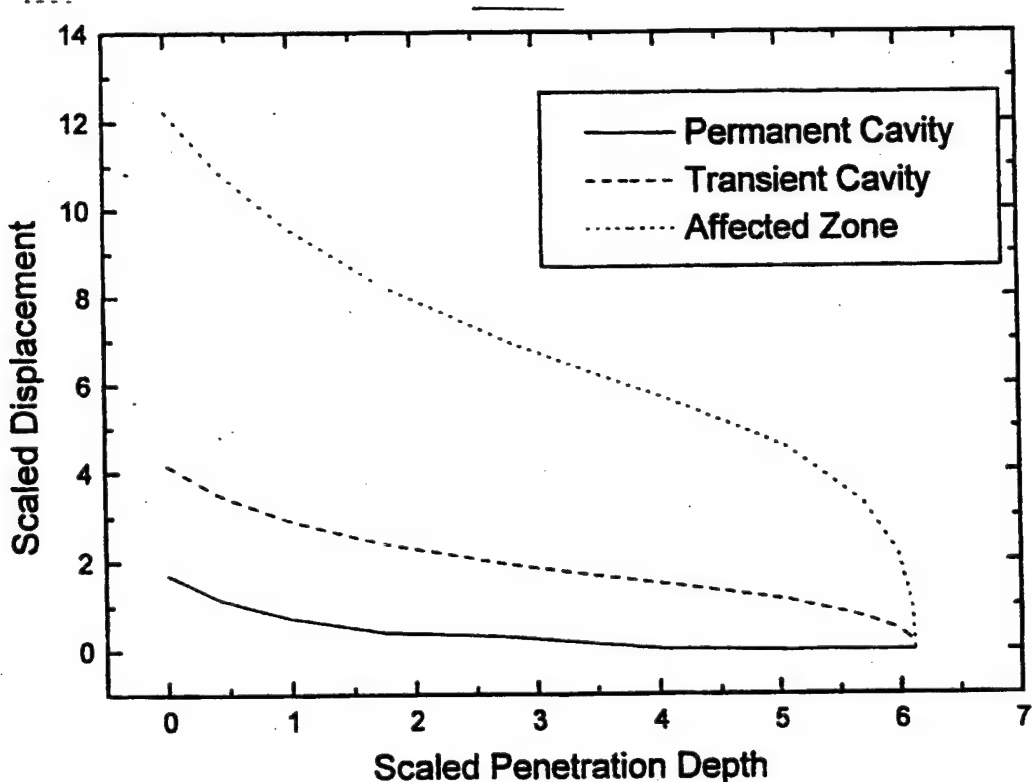


Figure 20. Affected Zones and Cavities as a Function of Penetration Depth for Non-Linear Spring Model with Five Particles ($K_1 = 1.0$ and $K_2 = 0.35$)

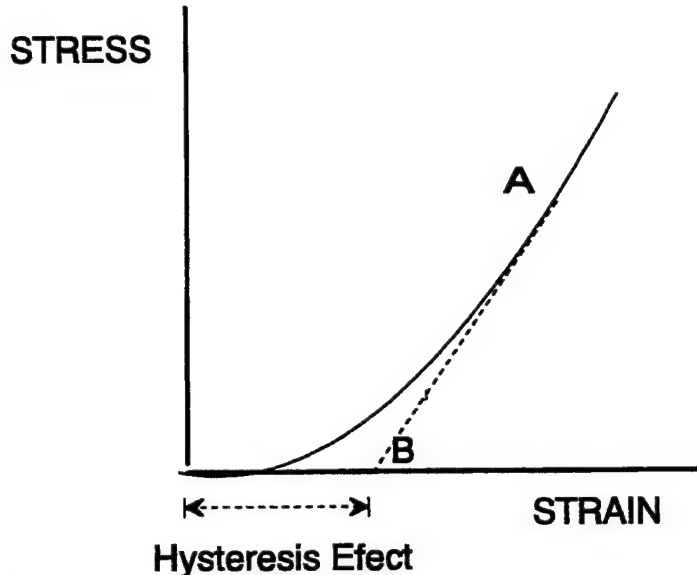


Figure 21. Schematic of Hysteresis Effect

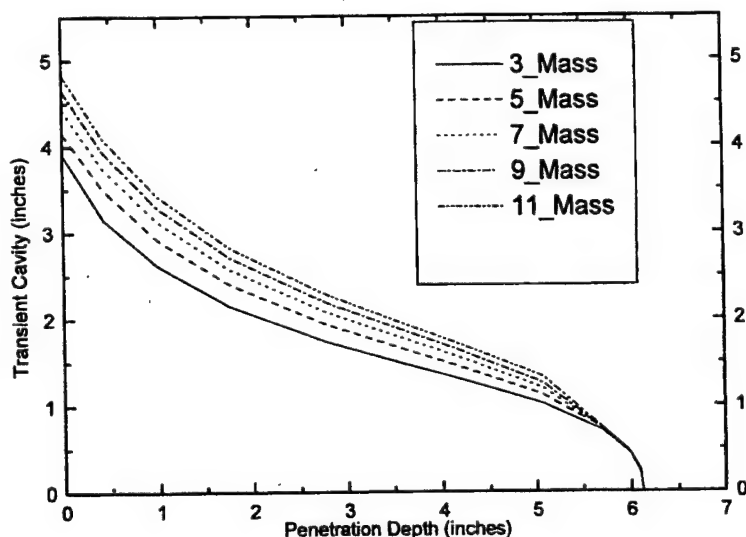


Figure 22. Transient Cavities Plotted at Different Penetration Depths for Various Numbers of Particles (3, 5, 7, 9, and 11) in Non-Linear Spring Model

replaced with a 20% gelatin or any other suitable medium where the characteristic of the force of resistance as a function of instantaneous velocity is known. We should recall at this point that the coefficients appearing the description of this force of retardation are influenced by the material properties of target and projectile as well as by the geometrical shape of the bullet tip. In our

Notice in Figure 22 that convergence (i.e., the offset between the various curves) is slower at high penetration velocities than at low penetration velocities (where the offset between the various curves decrease very fast with increasing numbers of particles).

Analytical models were also developed that calculate the wound tract geometry for motion of a bullet or other similar bodies of high aspect ratio in a bone-tissue environment. We assumed that the bullet suffered no rotation until it hits the bone so that its center of mass moves in a straight line. It is possible to relax this condition on the projectile kinematics but the resulting problem becomes three-dimensional. Besides, for most problems of interest, this condition does not impose any limitations in applications of these models.

The problem was formulated as follows. We consider a target composed of tissue matrix where a cylindrical shape bone is embedded. Here the tissue material is

earlier analysis, we developed a sufficiently accurate model that describes the force of retardation as a cubic polynomial in the instantaneous velocity.

For bullets impacting bones, depending on the entry velocity of the bullet prior to hitting the bone, various modes of motion can be classified as follows.

- (1) *No penetration of bone.* In this case, the projectile velocity is not enough to penetrate so that the bullet either turns or rebounds. This threshold velocity is approximately 200 ft/sec for osteoporotic bones and 700 ft/sec for normal bones.
- (2) *Drill hole mode:* This mode occurs for certain entry velocity of the bullet. Bullet penetrates like a drill hole with clean entry and exit holes.
- (3) *Brittle fracture mode:* For a given bullet and certain range of entry velocity, the bone suffers radial fractures that are sometimes so bad that the whole bone disintegrates. The main mechanism for these fractures is the propagation of highly compressive and reflected tensile waves through the target.

We have successfully developed models which use an already existing two-dimensional code for determining the wound track in a homogeneous medium. This code is first used to determine the motion of the bullet just prior to hitting the bone. If the bullet velocity at this instant is below threshold velocity, the bullet will either rebound or turn. This produces some discontinuities in the bullet velocity (both translational and angular). These discontinuities have been calculated using impulse equations and then the data on linear and angular velocity of the bullet is fed to the above two-dimensional code as initial values for the calculation of the subsequent wound track geometry.

These cases of the drill-hole mode can also be handled the same way using the same code as above. In this case, however, the bullet continues to move in a straight line after entering the bone with different retardation coefficients than that of a gelatin target.

A possibility of a critical shear force model has also been tested for applications in the cases of drill-hole mode fractures for low velocities. Experimental data shows that for the osteoporotic bones, the average force of resistance is 11.68 lb. for 0.250-in diameter spherical projectiles while it is 12 lb. for 0.406-in diameter projectiles moving at 200-400 ft/sec. This data justifies a critical force criterion for low velocity penetration of bullets in bones.

2.4 KINEMATICS OF BULLET PENETRATION IN A GELATIN WITH EMBEDDED BONES

In general, when a projectile enters a target, it experiences resistance to penetration. The resistance comes from the contact area of the projectile with the target medium. The force of resistance is distributed over this contact area. If we know how these forces are distributed along with their directions and magnitudes we can exactly determine the path of the projectile inside the target. From the analysis that has been done, it has been found that the magnitude of the force of resistance at any point depends on the instantaneous velocity of the projectile at the point of contact while the direction is usually assumed to be in the direction of the normal component of the velocity with respect to the projectile surface. This is, however, not true in cases where high viscosity is present in the target medium and shear forces may contribute to the force of resistance. The generation of shear forces does not complicate the problem if the nature and magnitude of these forces are known in terms of the instantaneous velocity, v . Thus, when the projectile is completely immersed and moving in the target, the kinematics of the projectile can be calculated by writing down the equations of motion of the projectile for the center of mass and about the center of mass (CM). For the case of a projectile moving in an ordnance gelatin target, these equations are given by (Figure 12, page 28)

$$\begin{aligned} m\ddot{x}_G &= - \int_{-l}^l \rho R(|v_{pn}|) \operatorname{sgn}(v_{pn}) \cos \theta dr - m_f R(|v_{en}|) \operatorname{sgn}(v_{en}) \sin \theta \\ m\ddot{y}_G &= + \int_{-l}^l \rho R(|v_{pn}|) \operatorname{sgn}(v_{pn}) \sin \theta dr - m_f R(|v_{en}|) \operatorname{sgn}(v_{en}) \cos \theta \end{aligned} \quad (26)$$

The equation of motion about the CM can be obtained, as before, by taking moments of the equations of motion of the ensemble of particles constituting the projectile about the CM . This yields

$$I_G \ddot{\theta} = - \int_{-l}^l \rho R(|v_{pn}|) \operatorname{sgn}(v_{pn}) r dr \quad (27)$$

When a bullet or a projectile is entering a surface corresponding to a material discontinuity e.g., in the early phase of gelatin penetration from air or early phase of bone penetration from the gelatin/tissue side, the projectile kinematics is more complicated than of the completely immersed case. In this case, the part of the projectile in contact with the surface of material discontinuity suffers a different distribution of resistance forces than the rest of the projectile. Thus, Equations 26 and 27 should contain two integrals; one for the contact area of the material discontinuity and other for the area that has not yet penetrated the medium. This introduces discontinuities in the velocity distribution for both the linear and angular components of the projectile. It is necessary to analyze these issues in order to describe projectile penetration through a gelatin/soft tissue embedded bone. Below we give some analysis of this problem, which may yield some information about the physical nature of the force of resistance coming

from the surface of discontinuities. We also mention some of the fracture modes observed during bone penetration.

Analysis of Various Modes of Bone Fracture

It has not yet been conclusively established what parameters of the dynamic process of projectile penetration are responsible for bones to preferentially fracture in a specific mode. Two important parameters of penetration dynamics are projectile size and entry velocity. The kinetic energy of the projectile is directly proportional to both of these quantities. From ballistic impact experiments reported in the literature involving embedded bones in ordnance gelatin targets and spherical projectiles of various sizes; it is seen that increasing the size of the spherical projectile is effective in penetrating the bone with little or no radial fractures on the anterior side while a decrease in the size of the spherical projectile is less effective in penetration but effective in creating brittle mode radial fractures.

For example, an osteoporotic femur subject to impact by a 0.406-in. sphere at 600 ft/sec penetrates the bone with little or no radial fractures while a 0.250-in. sphere at 602 ft/sec did not penetrate but produced radial fractures emanating from the entrance hole. If we increase the speed of the smaller size sphere to 908 ft/sec, the projectile also stops but the bone is broken into two.³ This case has about 41% more kinetic energy than that of the larger size sphere but no penetration occurs. This shows that the distribution of energy for smaller size spheres is more focused towards radiation of energy than towards penetration. Hence the increase in kinetic energy alone does not necessarily guarantee penetration. We need to know how projectile size and its velocity affect the distribution of energy.

To calculate the radial fracture from compressive waves, MRC has developed a singular displacement model where, to the lowest order in singularity, the radial displacement decays like $1/r$ where r is the distance from the center of the projectile footprint. For smaller footprints, it radiates more intense compressive waves. This model gives the same qualitative result as observed in the above experiments. For fractures in coated and uncoated polycarbonate substrates, these models yield quantitative estimates of radial fracture that is in extremely good agreement with experiments.⁴ However, this mechanism of energy distribution has not yet been completely understood. More systematic impact experiments are needed where one parameter of impact should be changed while others remain unchanged so that the effect of a particular parameter on the penetration mechanism can be understood.

2.4.1 Characteristics of Bone Impact and Penetration

When a projectile penetrates a target modeled by an embedded bone in a gelatin/tissue, host matrix, and its penetration characteristics after it impacts the embedded bone depends mostly on the following quantities:

- a. Incident velocity of the projectile immediately before it impacts the bone
- b. Projectile material, shape and size
- c. Bone condition (Normal, Osteoporotic, Mildly Osteoporotic etc.)

Table 2. Energy and Velocity Data on Spherical Steel Projectiles Impacting Human Femurs

Energy and Velocity Data on Spherical Steel Ball Impacting Human Femurs					$mass =$	
0.406 inch diameter steel ball						
Entry velocity	Exit Velocity	Average Velocity	Energy loss	Energy Loss per projected area		
ft/sec	ft/sec	ft/sec	ft-lbf			
			ΔE		$\Delta E/d^2$	$(\Delta E/d^2) \cdot 54.64$
203	0	101.5	6.3		38.22	101.2
252	40	146	8.8		53.39	141.3
297	72	184.5	11.8		71.59	189.5
400	232	316	15.8		95.85	253.7
493	338	415.5	19.5		118.30	313.1
603	432	517.5	26.9		163.19	431.9
699	534	616.5	30.9		187.46	496.1
814	619	716.5	42.4		257.23	680.8
906	729	817.5	43.9		266.33	704.8
1011	801	906	57.7		350.04	926.4
1101	903	1002	60.6		367.64	973.0
1247	1045	1146	71		430.73	1139.9
1409	1186	1297.5	88.4		536.29	1419.3
1548	1310	1429	103.8		629.72	1666.6
			103.8		629.72	
0.250 inch diameter steel ball						
Entry Velocity	Exit Velocity	Average Velocity	Energy loss	Energy Loss per projected area		
ft/sec	ft/sec	ft/sec	ft-lbf			
207	0	103.5	1.5		24	24.1
255	29	142	2.2		35.2	35.3
294	46	170	3		48	48.2
350	81	215.5	3.8		60.8	61.0
398	88	243	5		80	80.3
434	95	264.5	6		96	96.3
504	155	329.5	7.7		123.2	123.6
591	263	427	9.7		155.2	155.7
701	363	532	12.6		201.6	202.3
806	456	631	15.3		244.8	245.7
904	558	731	17.6		281.6	282.6
1006	631	818.5	21.5		344	345.2
1104	747	925.5	23.3		372.8	374.1
1249	863	1056	28.5		456	457.6
1405	974	1189.5	35.9		574.4	576.4
1548	1115	1331.5	40.5		648	650.3
1697	1213	1455	49.6		793.6	796.4
1951	1453	1702	59.8		956.8	960.1
2198	1670	1934	72.3		1156.8	1160.8
			72.3		1156.8	

Table 2 shows data from ballistic tests performed on embalmed human femurs with spherical projectiles. These data were garnered from the literature and represent unloaded, normal femurs. The literature sources are between 14 and 50 years old and therefore limited in the types of data that could be extracted from these experiments.

From the data that has already been examined however, it appears that a specific impulse of 0.4 $\text{lbf}\cdot\text{sec/in}^2$ represents the threshold required to cause a spiral fracture in the femur. This corresponds to a dynamic pressure of 2.16 ksi. This is similar to what was recorded on ballistic experiments discussed earlier. A spiral fracture is the fracture mode typically observed when the projectile does not directly strike the bone but the projectile passes close to the bone. A point load of approximately 287 pounds appears sufficient to cause a complete tensile failure of the femur.

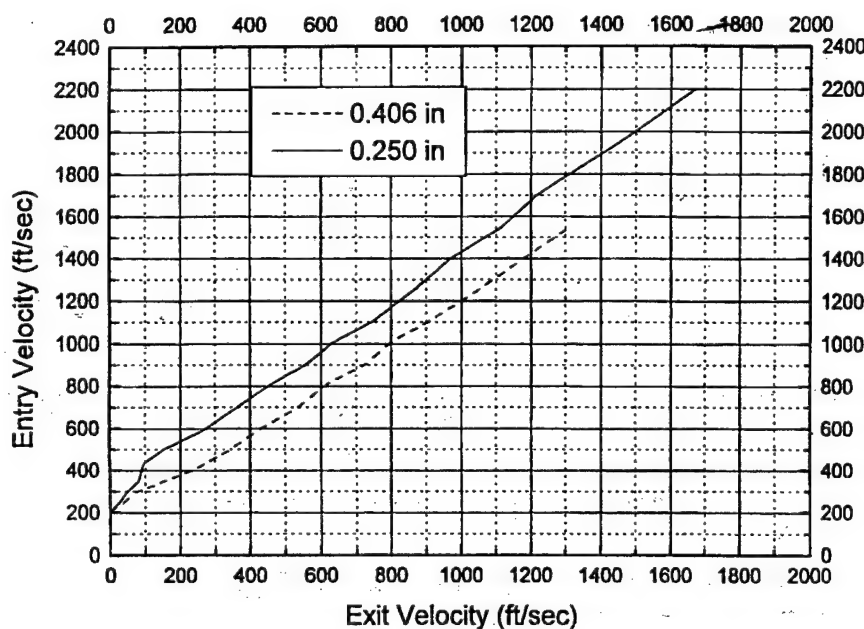


Figure 23. Entry and Exit Velocity of Steel Projectiles Striking Embalmed Human Femurs

penetration. In this case the results collapse onto each other. This is consistent with the mechanics of fracture where the "energy density" (i.e., energy loss per unit area) is a parameter used to describe fracture initiation and propagation. More generally, the criterion should be energy density per unit time. For spheres however the contact area per unit time is probably similar. We would expect to see profound differences however in the time history of the contact area for projectiles with different leading edge geometries.

We prepared a DARPA proposal with Dr. Paul Dougherty, Maj., USAMC (orthopedic surgeon at Fort Knox) to conduct ballistic testing of human femurs in a gelatin matrix while subject to a preload. This would provide an opportunity to validate analytical predictions and develop more relevant data that elucidate the issues above.

Figure 23 through Figure 25 reduce the data from this table in different ways. Figure 23 shows striking velocity versus exit velocity for two different diameter spheres. Figure 25 shows energy loss versus projectile average velocity during penetration of the bone. In these two plots the results show considerable divergence for the two different diameter spheres.

Figure 25 shows energy loss normalized to the projected area of the sphere versus average projectile velocity during

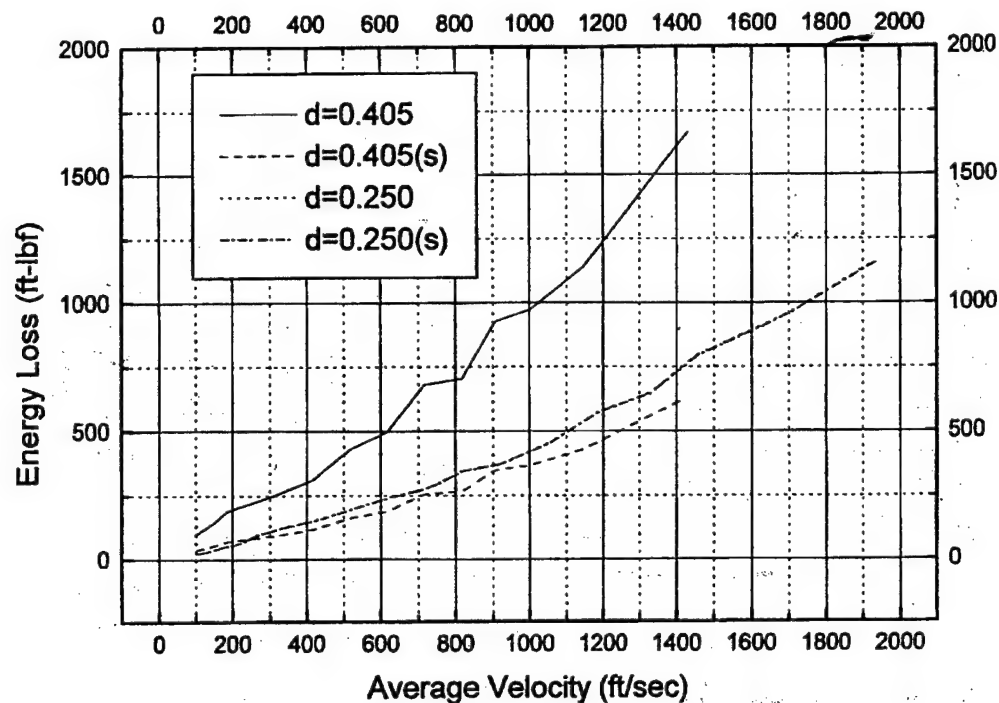


Figure 24. Energy Loss and Average Velocity (Scaled Display)

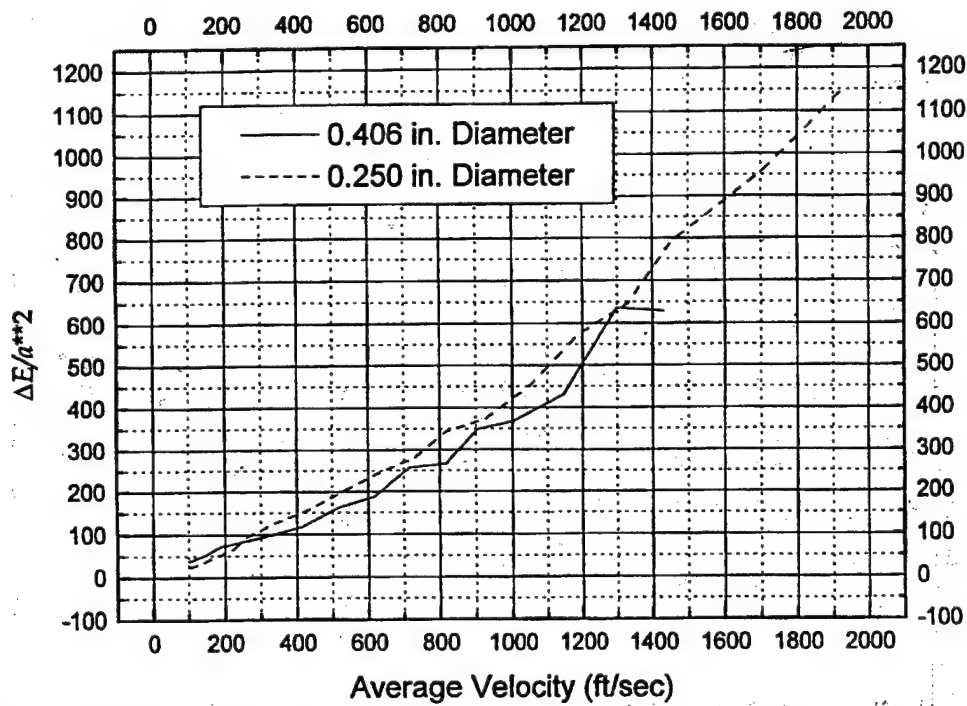


Figure 25. Energy Loss per unit Projected Area and Average Velocity

2.4.2 Bone Penetration Mode and Threshold Velocities

For a given target, the post impact phase of motion of the projectile depends on the pre-impact, incident velocity of the projectile. From an analysis of various experimental results reported in literature, we have concluded that various cases of bone impact modes emerge depending on the pre-impact, incident velocity, v_{in} , of the projectile. We have established the existence of two critical velocities – v_{1cr}, v_{2cr} – for normal bones, such that, after hitting the bone,

- i. rebounding of the projectile occurs if $v_{in} < v_{1cr}$
- ii. a clean-hole-bone-penetration mode occurs if $v_{1cr} \leq v_{in} \leq v_{2cr}$
- iii. a bone fragmentation mode occurs if $v_{in} > v_{2cr}$

2.4.3 Rebound Mode/Rebound Characteristic and Dynamics

In order to understand the nature of the force of resistance during the early phase of penetrating a material discontinuity, consider the following problem (see Figure 26). Let the projectile move with a velocity v in the x -direction just before it contacts the bone. We assume that at the point of contact on the surface of the discontinuity between the gelatin/tissue and a bone, the common normal makes an angle θ with the direction of the pre-entry projectile velocity. We also assume that the force of resistance, F , acts in the direction of a common normal (this is a condition that we can later relax). Since the velocity of the bullet suffers a discontinuity, let ϕ be the angle made by the post-entry velocity v' of the bullet. From Newton's laws of motion applied on the center of mass of the bullet, we have

$$m(\vec{v}' - \vec{v}) = \vec{F}\Delta t$$

which gives

$$\begin{aligned} v_x' &= v - \frac{F}{m} \cos \theta \Delta t \\ v_y' &= \frac{F}{m} \sin \theta \Delta t \\ \tan \phi &= \frac{\frac{F}{m} \sin \theta \Delta t}{v - \frac{F}{m} \cos \theta \Delta t} \end{aligned}$$

In the above equations, Δt is the transition time from v to v' .

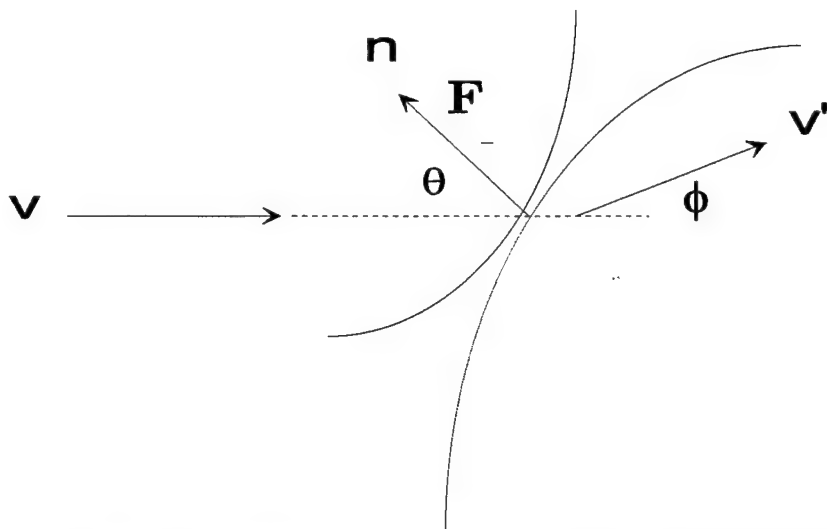


Figure 26. Nomenclature associated with pre- and post impact kinematics

If F is of the order $O(v^2)$, then $\phi = \pi - \theta$ and we have a complete rebound of the bullet. Thus, for penetration F is at least $O(v)$ that gives the new angle ϕ as

$$\phi = \frac{\frac{\alpha}{m} \sin \theta \Delta t}{1 - \frac{\alpha}{m} \cos \theta \Delta t}$$

$$F = \alpha v$$

If $F = O(v)$, then $\phi = 0$ so that bullet moves with unchanged direction.

Since the penetration of projectiles in gelatin are well understood and the associated algorithms at MRC give reasonably good results, we may solve the penetration problem up to the time it makes contact with the bone. After this, we need to establish the nature of the resistance force as a function of velocity in order to predict the projectile kinematics resulting from bone interaction. These distributions can be obtained from the geometry of the wound tract observed ballistic experiments involving targets with embedded bones and inversion of penetration depths under various impact scenarios.

2.4.4 "Drill Hole" Mode

This mode occurs when $v_{1cr} \leq v_{in} \leq v_{2cr}$. In this mode, the bullet leaves behind a wound tract similar to a drill hole with clean entry and exit holes.

2.4.5 Brittle Fracture Mode: Bone Fragmentation

When $v_{in} > v_{2cr}$, the bone manifests radial fractures that are so severe that the whole bone disintegrates. The main mechanism for these fractures is the propagation of highly compressive

waves through the target. Analytical models have been developed at MRC to interpret the existence of and to quantify such radial fractures. In the BONGEL Code (see Section 2.5), bone fragments and their final resting locations are modeled by a uniform random distribution.

2.4.6 Uniform Random Distribution

Since the injury data on bone fragmentation is very limited,⁵ it is not possible to determine the probabilistic distribution of fragment size, number of fragments and their final resting location in the body after bone disintegration takes place due to high velocity of impact. For the purpose of modeling, we have assumed that these distributions are uniformly random but some physical characteristics have been maintained to match experimental observations.

The maximum number of bone fragments used in BONGEL Code is 10. This result is in conformity with observations of reported bullet injuries that resulted in bone fragmentation. The energy partition and distribution of bone fragments is adjusted so that larger projectiles have a greater proportion of kinetic energy devoted to the penetration (as opposed to the brittle fracture process.

2.4.7 Final Location of Bone Fragments

The penetration depth of projectile and bone fragments is calculated in BONGEL using the previously described penetration algorithm with a known initial velocity. The circumferential and radial distribution along the mean fragment path is calculated from a random number generator using the assumption of a uniform random distribution.

2.5 DEVELOPMENT OF THE BONGEL CODE

MRC has developed the BONGEL code to analyze various aspects of the kinetics and kinematics of projectile penetration in a tissue target with embedded bone. To retain simplicity during the initial phase of the development, the bone is modeled as a right circular cylinder. In subsequent development, described in Section 4, the bone is allowed to take any other shape occupying a given volume of the target. In Section 4, the bone geometry is read from the virtual anatomy from the MGI *Lower Extremity Trauma Simulator*. Three types of projectiles can be used in the code; these are (1) bullets, (2) spherical projectiles, and (3) fragments.

In the code, these projectiles are identified by the code parameter PTYPE that takes the value 1, 2, or 3 for bullet, sphere or fragment type projectile, respectively. Since the input requirements for different types of projectiles may differ, for the ease of the user, projectile properties can be entered or modified independently. These files are BULLET.in, SPHERE.in and FRAGMENT.in, respectively. When the projectile type PTYPE is prescribed, the BONGEL code generates its own input file, BONGEL.in, by modifying the user specified projectile input files as necessary. These files also contain impact-scenario information, e.g., velocity, location and orientation of the projectile prior to impact.

Other than writing various graphics and other information files, this code is not a stand-alone code. The development has been done in modular forms so that each module can be modified independent of other modules. There are two screen utility codes that need to be present in the directory or file path. These files are necessary only when any modifications of this code are made and new compilation is performed. These two screen utility modules are CLS (clear screen) and TLOCATE (cursor positioning). These two modules are only provided in object-module forms so that only compilations can be done. No source codes for these two modules are either provided or deemed necessary.

Besides these two screen utility codes, other stand-alone modules are also used by the BONGEL code as necessary. When this is done, the BONGEL code creates the proper input files prior to running these codes. There are two such stand-alone codes that BONGEL uses; these are BULPENT2.for and CAVLOC2.for. The BULPENT2 code is used in the analysis of bullet penetration through tissue or bone medium while the CAVLOC2 code is used to generate temporary and permanent cavity locations as the projectile passes through the target. MRC has also developed a stand-alone code named MM4 that uses a one-dimensional, nonlinear spring model to calculate temporary and permanent cavity location for a chain of particles where only one end of the chain is given an initial velocity. Since the repeated use of the code in various directions at all locations of the projectile is necessary to generate the three-dimensional temporary and permanent cavity locations, and hence, is very much time consuming, BONGEL uses analytical fits obtained from MM4 code to predict temporary and permanent cavities. BONGEL prepares an input file for CAVLOC2 prior to calling this module for the calculation of three-dimensional temporary and permanent cavity surfaces.

As mentioned earlier, code developments are made in modular forms so that one module may execute another module if necessary. In order to implement such uses of other modules from any other module, BONGEL uses a SYSTEM command that is provided in the MICROSOFT FORTRAN Version 5 and above. Thus, other FORTRAN compilers lacking the SYSTEM command are not capable of compiling this version of the code. Some typical examples of such uses are shown in the following code lines

```
I=SYSTEM('COPY SXYD.PLT SXYD2.PLT')
I=SYSTEM('COPY SYYD.PLT SYYD2.PLT')
I=SYSTEM('COPY BULLIMP2.IN BULPENT2.IN')
I=SYSTEM('BULPENT2')
I=SYSTEM('CAVLOC2')
```

In the first three examples, the code uses the DOS copy command to copy some necessary files while in the last two examples, the code executes the modules BULPENT2 and CAVLOC2 using DOS commands.

A completely integrated version of this code can be generated easily if other compilers lacking the SYSTEM command are necessary.

The following files are necessary to run BONGEL:

BULLET.IN
SPHERE.IN
FRAGMENT.IN
BONGEL.EXE
BULPENT2.EXE
CAVLOC2.EXE

Other inputs files are automatically generated by BONGEL.

The following files are necessary to compile BONGEL:

BONGEL.FOR
CLS.OBJ
TLOCATE.OBJ

along with a FORTRAN compiler similar to Microsoft FORTRAN Version 5 and above.

A basic flowchart of BONGEL code is shown on the next page in Figure 27.

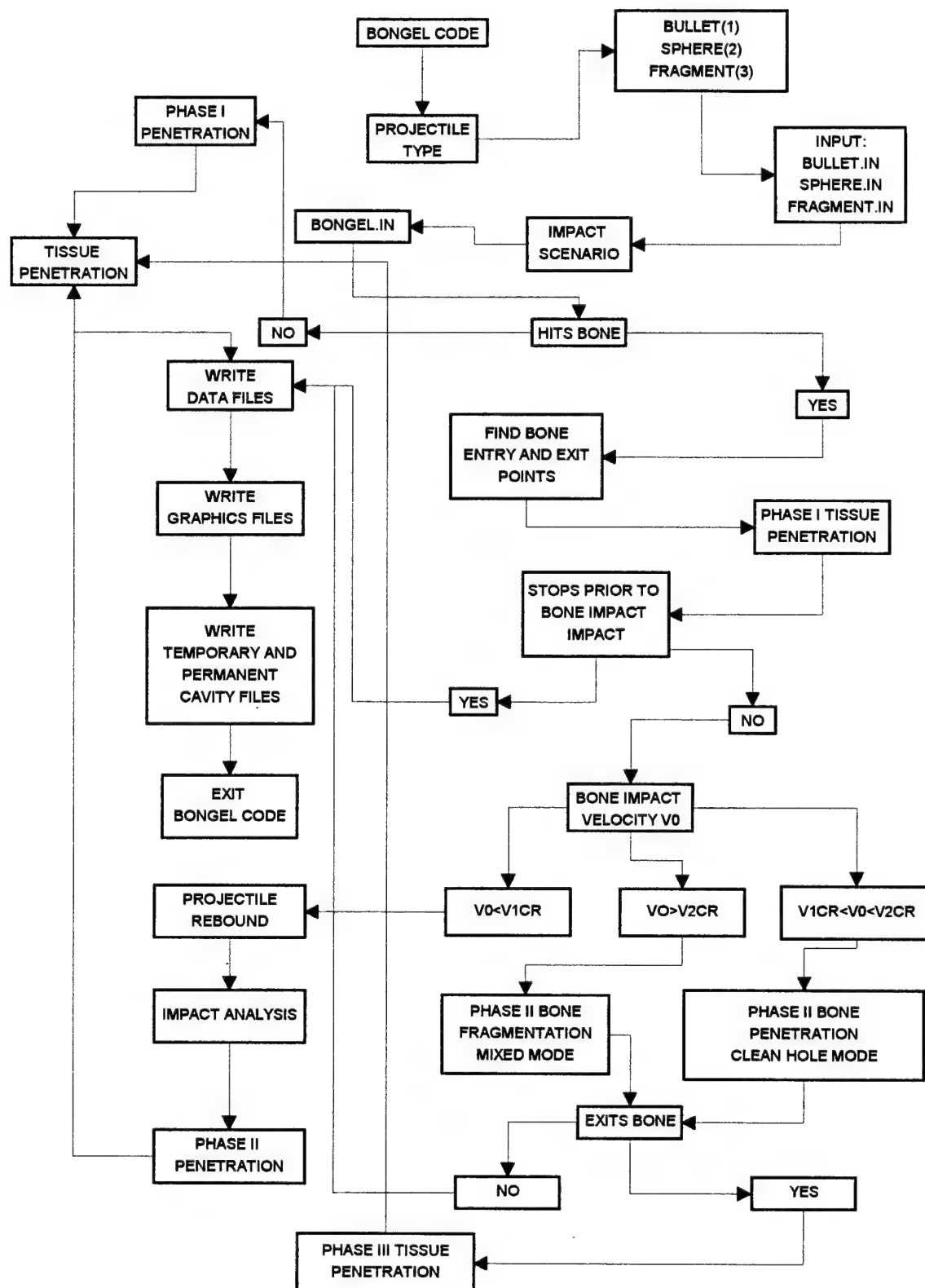


Figure 27. Flowchart of MRC BONEGEL code

2.5.1 Enhanced Tissue Damage due to Ejected Bone Fragments

When bone fragmentation occurs due to high impact velocity, these fragments move inside the tissue medium, and create additional damage. This damage is usually referred to as enhanced tissue damage. This part of the damage calculation is not incorporated in the current version of the code due to a lack of program resources. As previously mentioned there are no fundamental technical obstacles to incorporating this enhanced damage and this phenomenon could be incorporated at a future date.

2.5.2 Modifications Made to Incorporate Arbitrary Bone Shape and Location

The BONEGEL code includes an interface to the virtual anatomy included in the *MGI Lower Extremity Battlefield Trauma Simulator*. This interface is discussed further in Section 4. The virtual anatomy is available in a digitized form so that when a coordinate is specified with respect to a user defined rectangular coordinate system, the associated part can be identified. We therefore modified the BONGEL code so that for a given impact scenario, entry and exit points on the bone can be identified in cases where the projectile impacts the bone and a bone penetration may occur. This has been done as follows.

When the impact scenario is specified by the INFILCT module discussed in Section 4, the direction cosines (ℓ, m, n) and the coordinates (a, b, c) of the point of entry, A , in the body are known. Thus the coordinates (x, y, z) of any other point, P , on the line of penetration of the projectile can be written in terms of the distance $AP = r$ as

$$\begin{aligned}x &= a + \ell r \\y &= b + mr \\z &= c + nr\end{aligned}$$

By tracking the coordinates (x, y, z) as the projectile moves (gradual increase in r) along its line of penetration, we can determine in advance if bone impact occurs, and if so, its entry and exit points in cases where bone penetrations occur. This algorithm can replace the relevant part of the BONGEL code when the integration of BONGEL with the digitized database is made.

2.5.3 Axis Systems used in BONGEL Code

Frame F: (Oxyz) Global or User Defined Coordinate System
(Qx'y'z') Local coordinate system at the bone impact point Q
 (ℓ, m, n) direction cosines of the original bullet shot line with respect to the frame F.
 (α, β, γ) direction cosine of the impulsive force at Q with respect to F. This direction is along the outward normal direction to the bone surface at the impact point Q. Plane π is the plane containing the lines (ℓ, m, n) and (α, β, γ) .

(ℓ_1, m_1, n_1) direction cosines of the new direction of the projectile center of mass, G , velocity right after bone impact in the case where rebounding occurs after bone impact. This forms the new x' axis at Q . This is also referred to as LP,MP,NP in the BONGELT code.

Cross product of the lines (ℓ, m, n) and (α, β, γ) forms the new z' axis at Q .

The direction cosines of the Qz' axis are denoted as (ℓ_2, m_2, n_2)

The cross product of z' - and x' -axes at Q forms the new y' axis at Q .

The direction cosines of the Qy' axis are denoted as (ℓ_3, m_3, n_3)

2.5.4 File Structures in BONGEL Code

The generation of internal files in BONGELT and Other Called Programs (RK2S) and Codes (BULLPENT2)

RK2S Subroutine (For One dimensional motion $x = x(t)$, x -space, t -time)

File	Unit	Description
SXY.PLT	9	x vs. t
SXYD.PLT	10	$\frac{dx}{dt}$ vs. t
SYYD.PLT	11	x vs. $\frac{dx}{dt}$
STPHS.COD	15	Code Control Parameter

BULLPENT2 Code (Run by BONGELT2 Code, for Two-dimensional Motion

$x = x(t)$, $y = y(t)$; Subscript G indicates the center of mass of the bullet, subscript 1 indicates the front tip while subscript 2 indicates back tip of the bullet)

θ indicates bullet orientation with the x -axis.

File	Unit	Description
BXG.PLT	2	x_G vs. t
BXGD.PLT	3	$\frac{dx_G}{dt}$ vs. t
BYG.PLT	4	y_G vs. t
BYGD.PLT	5	$\frac{dy_G}{dt}$ vs. t
BTH.PLT	6	θ (deg) vs. t
BTHD.PLT	7	$\frac{d\theta}{dt}$ vs. t
BULLPENT2.DBG	8	Debug File
BXY1.PLT	9	(x, y) for tip 1
BXY2.PLT	10	(x, y) for tip 2
BXYG.PLT	11	(x, y) for the center of mass G
BYAW.PLT	12	Yaw angle vs. time t
BULLPEN.ANM	14	Graphic Animation File

STPHS.COD	16	Code control parameter
BXY1D.PLT	18	Velocity components for the front tip along the x- and y-axis.

Note: These file names have been modified by adding 1, 2 or 3 after their names to indicate the data obtained during phase 1, 2 or 3 of the projectile penetration where the different phases of motion are defined as follows:

Phase 1: Projectile motion prior to bone impact

Phase 2: Projectile rebound mode or penetration-through-bone mode

Phase 3: Projectile reentry in tissue medium after bone penetration is completed.

Significant efforts have been made in developing analytical models capable of calculating wound tract geometry for the motion of a bullet or other similar bodies of high aspect ratio in a bone-tissue environment. We assumed that the bullet suffered no rotation until it hits the bone so that its center of mass moves in a straight line. Although this is not the most general case, for extremities that tend to have short wound paths, more often than not, the projectile follows a rectilinear path unless an interaction with bone tissue occurs. This tends to not be true in other regions of the body where the wound tracts are substantially longer. We have modeled the three dimensional curvilinear path the projectile follows after bone interaction however we elected not to include non-rectilinear paths in soft tissue prior to bone interaction. This scope was defined in the proposal and does not represent any fundamental technical obstacles but merely a decision relative to managing resources.

It is possible to relax this condition on the projectile kinetics but the resulting problem becomes three-dimensional. Besides, for most problems of interest, this condition does not impose any limitations in applications of these models. The problem we are currently working on can be formulated as follows. We consider a target composed of tissue matrix where a cylindrical shaped bone is embedded. Here the tissue material is replaced with a 20% gelatin or any other suitable medium where the characteristic of the force of resistance as a function of instantaneous velocity is known. We should recall at this point that the coefficients appearing in the description of this force of retardation are influenced by the material properties of target and projectile as well as by the geometrical shape of the bullet tip. In our earlier analysis, we have developed a sufficiently accurate model that describes the force of retardation as a cubic polynomial in the instantaneous projectile velocity, v . For bullets impacting bones, depending on the entry velocity, v_c , of the bullet prior to hitting bone, three interaction modes can be classified as follows.

- (1) *No penetration of bone.* In this case, v_c is not sufficient to effect penetration so that the projectile either turns or rebounds. This threshold velocity, v_d , is approximately 200 ft/sec for osteoporotic bones and 700 ft/sec for normal bones.
- (2) *Drill hole mode.* This mode occurs for certain entry velocities where the projectile penetrates like a "drill hole" with clean entry and exit holes.

(3) *Brittle fracture mode*. For a given bullet and certain range of entry velocity, the bone suffers radial fractures that are sometimes so severe that the whole bone disintegrates. The main mechanism for these fractures is propagation of highly compressive and reflected tensile waves through the target.

We have successfully developed models that used an existing two-dimensional code for determining the wound track in homogeneous medium.⁶ This code is first used to determine the motion of the bullet just prior to hitting the bone. If the bullet velocity at this instant is below, v_d , the bullet will either rebound or turn. This produces some discontinuities in the bullet velocity (both transnational and angular). These discontinuities have been calculated using impulse equations and then the data on linear and angular velocity of the bullet is fed to the above two-dimensional code as initial values for the calculation of the subsequent wound track geometry.

The *drill-hole* mode can also be handled the same way using the same code as above. In this case, however, the bullet continues to move in a straight-line path after entering the bone with different retardation coefficients than that of a gelatin target.

A possibility of a critical shear force model has also been tested for applications in the cases of *drill-hole* mode fractures for low velocities. Experimental data shows that for the osteoporotic bones, the average force of resistance is 11.68 lb. for 0.250-in diameter spherical projectiles while it is 12 lb. for 0.406-in diameter projectiles moving at 200-400 ft/sec. This data justifies a critical force criterion for low velocity penetration of bullets in bones.

2.5.5 Some Additional Notes on the File Structures used in the BONGEL code

There are two main modules of the code. Both Codes are written in FORTRAN. One is called BONGELT2.FOR that is a preprocessor that processes the user input and generates the input code for the second module BULLPENT.FOR. This module actually calculates the velocity-time, space-time, paths of the projectile for the front tip, back tip and center of mass, G. Currently, the code works for a bullet or any other slender object with high aspect ratio (e.g., a flechette) as well as for spherical projectiles and fragment penetrations. The code uses a Microsoft SYSTEM command through I=SYSTEM('dos command'C) which may not be available to other compilers. This code also uses two FORTRAN object modules called CLS and TLOCATE. These subroutines are used to clear the screen and to locate the cursor on the screen, respectively. If necessary, the code can be modified to bypass these statements. Descriptions of the internal files and input files are as follows:

⁶ R. D. Eisler, A. K. Chatterjee, and G.H. Burghart, *Algorithm Development to Describe Retardation in Human Tissue of a 19.6 Grain Flechette*, Mission Research Corporation Report MRC-COM-R-93-0372, US Army Natick Technical Report TR-95/023L, May 1995 (Unclassified - Limited Distribution).

2.5.5.1 File Description for BONGELT2 Code

Files opened in Bone-Gelatin Interaction Code: BONGELT2.FOR

File	Unit	Description
BONGELT2.IN	1	Input File
BONGELT2.DBG	20	Debug File, if DEBUG.NE.0
BULLIMP1.IN	2	Phase I Input File for BULLPENT.for Code
BXYG1.PLT	9	First Phase X-Y data for the center of mass G
STPHS.COD	15	Projectile arrest flags
BXGD.PLT	10	Velocity vs. space data for G
BULLIMP2.IN	2	Phase II input file for BULLPENT
BXYG2.PLT	9	Second Phase X-Y data for G
STPHS.COD	15	Projectile arrest flags
BXGD.PLT	10	Described earlier
BULLIMP3.IN	2	Phase III input file for BULLPENT
BXYG3.PLT	9	Third Phase X-Y data for G
BULLIMP2.IN	2	Described above
BXY12.PLT	9	Front Tip X-Y data in Phase II
BXY22.PLT	10	Back Tip X-Y data in Phase II
BXYG2.PLT	11	X-Y data for G in Phase II
XYZ1.PLT	12	Front Tip XYZ-data
XYZ2.PLT	14	Back Tip XYZ-data
XYZG.PLT	16	XYZ-data for G
XYZALL.PLT	18	XYZ-data for Tip1(Front), Tip 2(Back) and G
TXYZ12.PLT	19	Time and XYZ-data for Tip 1, Tip 2 and G

Files copied through SYSTEM Copy Command in BONGELT2

```

I=SYSTEM('COPY BULLIMP1.IN BULLPENT.IN'C)
I=SYSTEM('COPY BXY1.PLT BXY11.PLT'C)
I=SYSTEM('COPY BXGD.PLT BXGD1.PLT'C)
I=SYSTEM('COPY BXY2.PLT BXY21.PLT'C)
I=SYSTEM('COPY BXYG.PLT BXYG1.PLT'C)
C I=SYSTEM('COPY BXG.PLT BXG1.PLT'C)           commented out
I=SYSTEM('COPY BULLIMP2.IN BULLPENT.IN'C)
I=SYSTEM('COPY BXY1.PLT BXY12.PLT'C)
I=SYSTEM('COPY BXGD.PLT BXGD2.PLT'C)
I=SYSTEM('COPY BXY2.PLT BXY22.PLT'C)
I=SYSTEM('COPY BXYG.PLT BXYG2.PLT'C)
C I=SYSTEM('COPY BXG.PLT BXG2.PLT'C)           commented out
I=SYSTEM('COPY BULLIMP3.IN BULLPENT.IN'C)
I=SYSTEM('COPY BXY1.PLT BXY13.PLT'C)
I=SYSTEM('COPY BXGD.PLT BXGD3.PLT'C)

```

```

I=SYSTEM('COPY BXY2.PLT BXY23.PLT'C)
I=SYSTEM('COPY BXYG.PLT BXYG3.PLT'C)
C  I=SYSTEM('COPY BXG.PLT BXG2.PLT'C)           commented out
I=SYSTEM('COPY BULLIMP2.IN BULLPENT.IN'C)
I=SYSTEM('COPY BXY1.PLT BXY12.PLT'C)
I=SYSTEM('COPY BXGD.PLT BXGD2.PLT'C)
I=SYSTEM('COPY BXY2.PLT BXY22.PLT'C)
I=SYSTEM('COPY BXYG.PLT BXYG2.PLT'C)
C  I=SYSTEM('COPY BXG.PLT BXG2.PLT'C)           commented out

```

2.5.5.2 File Description for Bullet Penetration Code BULLPENT

File	Unit	Description
BULLPENT.IN	1	Input File
BULLPENT.DBG	8	Debug File
BXY1.PLT	9	XY-File for Front Tip
BXY2.PLT	10	XY-File for Back Tip
BXYG.PLT	11	XY-File for the center of mass G
BYAW.PLT	12	Yaw Data
BULLPEN.ANM	14	Animation Data File
BXDX.PLT	15	Velocity vs. Space for G
STPHS.COD	16	Data File for Arrest Flags
BXG.PLT	2	X-Time File for G
BXGD.PLT	3	X-Velocity-Time File for G
BYG.PLT	4	Y-Time File for G
BYGD.PLT	5	Y-Velocity-Time File for G
BTH.PLT	6	Yaw-Time File
BTHD.PLT	7	Yaw Rate-Time File

2.5.5.2.1 Coordinate System Used in BONGEL Code

With reference to Figure 28, a description of the two reference frames that have been used in the development of BONGEL Code. All coordinate input to the BONGEL.IN file must be made in the user or global frame F. But the code uses some internal frame so that other modules of the code can be used. This is referred to as the local frame ($Qx'y'z'$) with origin at the bone impact point Q. A description of the shotline in the local coordinate frame and the impact direction for the rebound mode is shown in Figure 29.

Frame F: (Oxyz) Global or User Defined Coordinate System

($Qx'y'z'$) Local coordinate system at the bone impact point Q

(ℓ, m, n) direction cosines of the original bullet shot line with respect to the frame F.

(α, β, γ) direction cosine of the impulsive force at Q with respect to F. This direction is along the outward normal direction to the bone surface at the impact point Q.

Plane π is the plane containing the lines (ℓ, m, n) and (α, β, γ).

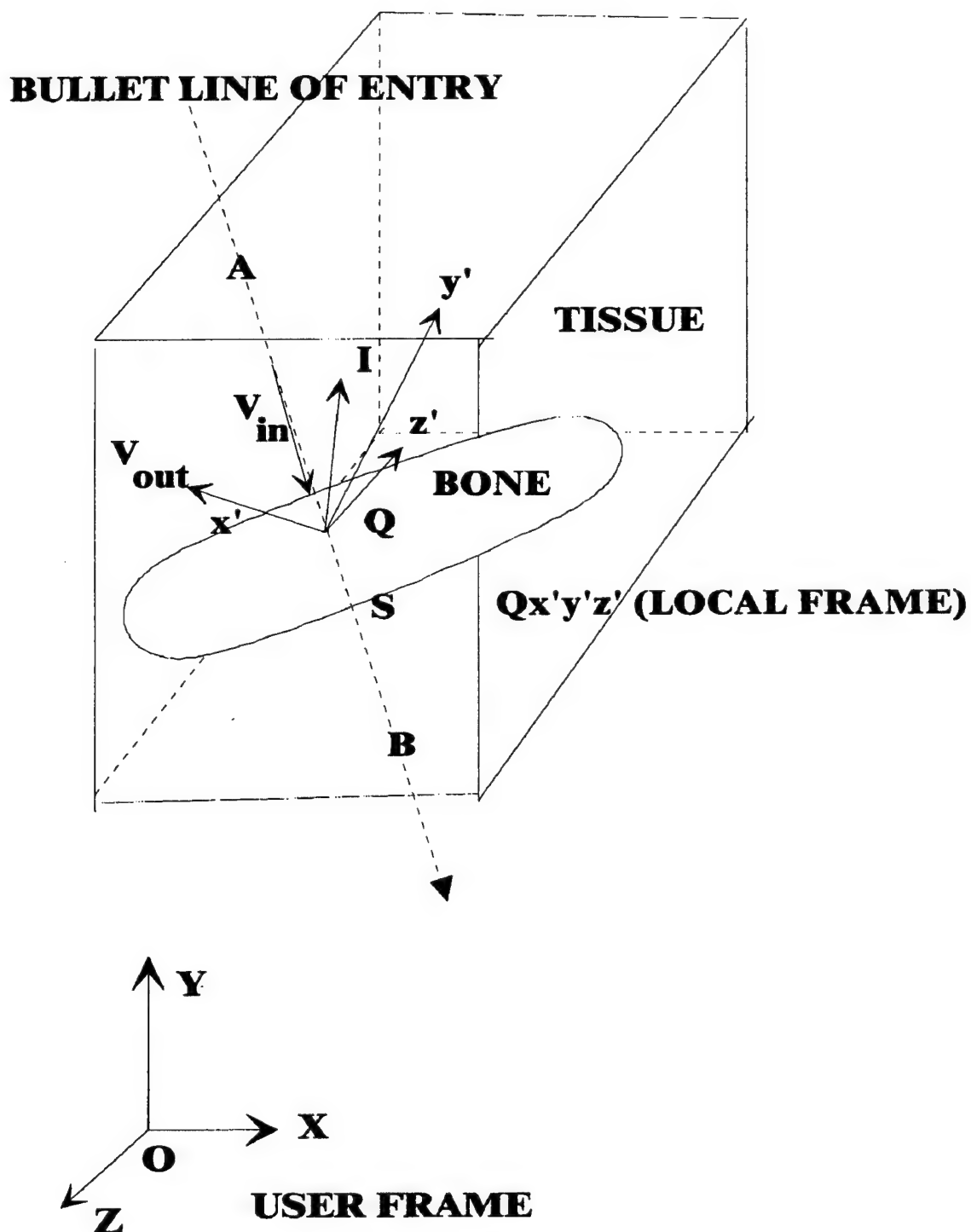
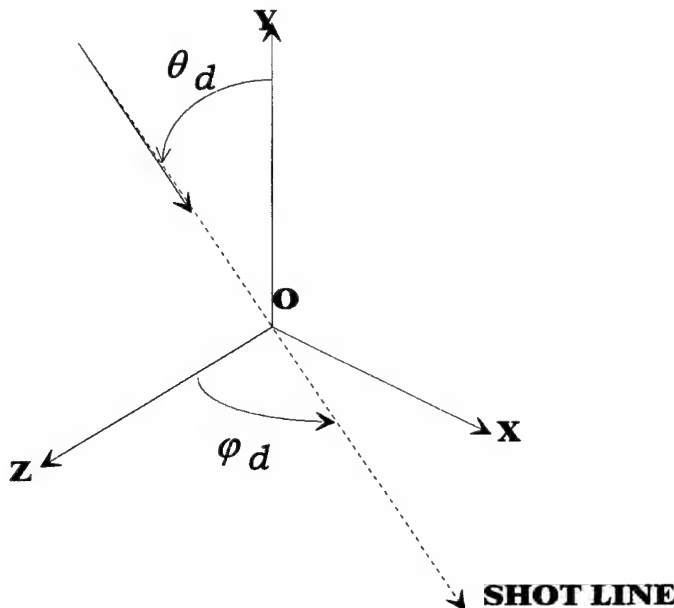


Figure 28. Coordinate Systems Used in BONEGEL Code



OXYZ (USER FRAME)

Figure 29. Shotline and Impact Direction in the Local Frame System

(ℓ_1, m_1, n_1) direction cosines of the new direction of velocity of the center of mass G right after bone impact in the case where rebounding occurs after bone impact. This forms the new x' axis at Q. This is also referred to as LP, MP, NP in the BONGELT code.

Cross product of the lines (ℓ, m, n) and (α, β, γ) forms the new z' axis at Q.

The direction cosines of the Qz' axis are denoted as (ℓ_2, m_2, n_2)

Cross product of z'- and x'-axes at Q forms the new y' axis at Q.

The direction cosines of the Qy' axis are denoted as (ℓ_3, m_3, n_3)

2.5.5.2.2 Generation of Internal Files in BONGELT and Other Called Programs (RK2S) and Codes (BULPENT2)

RK2S Subroutine (For One dimensional motion $x = x(t)$, x -space, t -time)

File	Unit	Description
SXY.PLT	9	x vs. t
SXYD.PLT	10	$\frac{dx}{dt}$ versus t
SYYD.PLT	11	x versus $\frac{dx}{dt}$
STPHS.COD	15	Code Control Parameter

BULLPENT2 Code (Run by BONGELT2 Code, for Two-dimensional Motion
 $x = x(t), y = y(t)$; Subscript G indicates the center of mass of the bullet, subscript 1 indicates the front tip while subscript 2 indicates back tip of the bullet)
 θ indicates bullet orientation with the x-axis.

File	Unit	Description
BXG.PLT	2	x_G vs. t
BXGD.PLT	3	$\frac{dx_G}{dt}$ vs. t
BYG.PLT	4	y_G vs. t
BYGD.PLT	5	$\frac{dy_G}{dt}$ vs. t
BTH.PLT	6	θ (deg) vs. t
BTHD.PLT	7	$\frac{d\theta}{dt}$ vs. t
BULLPENT2.DBG	8	Debug File
BXY1.PLT	9	(x, y) for tip 1
BXY2.PLT	10	(x, y) for tip 2
BXYG.PLT	11	(x, y) for the center of mass G
BYAW.PLT	12	Yaw angle vs. time t
BULLPEN.ANM	14	Graphic Animation File
STPHS.COD	16	Code control parameter
BXY1D.PLT	18	Velocity components for the front tip along the x- and y-axis.

Note: These file names have been modified by adding 1, 2 or 3 after their names to indicate the data obtained during phase 1, 2 or 3 of the projectile penetration where the different phase of motion are defined as follows:

Phase 1: Projectile motion prior to bone impact

Phase 2: Projectile rebound mode or penetration-through-bone mode

Phase 3: Projectile reentry in tissue medium after bone penetration is completed.

2.5.6 Units Used in the BONGEL Code

Unless otherwise specified, the following units are used for all input and output data:

Length (L) in centimeters (cm)

Time (T) in seconds (s)

Mass (M) in grams (gm)

All other units are consistent with the above units. For example, velocity $\left(\frac{L}{T}\right)$ is measured in $\frac{cm}{s}$, acceleration $\left(\frac{L}{T^2}\right)$ is in $\frac{cm}{s^2}$, force F $\left(\frac{ML}{T^2}\right)$ is in $\frac{gm \cdot cm}{s^2}$, impulse (F.T) is in $\frac{gm \cdot cm}{s}$ etc.

3 BALLISTIC TESTING

Table 3 shows a complete log of ballistic test implemented under this program. The purpose of the ballistic testing is fourfold: (1) determine for a spherical projectile the threshold velocity required to penetrate – i.e., inelastically deform – various formulations of gelatin targets with parametrically varied mechanical properties, (2) collect data relative to the effect of leading edge projectile geometry on target transient response, (3) collect data relative to target boundary effects; and, (4) segregate *pressure drag* versus lateral surface viscous effects.

Item 1 was investigated by using spherical projectiles with two diameters and the same material density. The striking velocity required to enter 10, 15, and 20% gelatin targets was experimentally determined. Since concentrations less than 20% are sensitive to temperature variations, testing was accomplished at controlled temperatures.

Items 2, 3, and 4 involved investigating the transient response of the gelatin for two different gelatin formulations and variable projectile and target geometries (gelatin blocks of different sizes and with different support conditions). This phase of the experimental effort involved collecting high frequency pressure measurements supplemented with temporally correlated flash photography.

An analytical model of dynamic pressure was developed to support investigation of issues 2, 3, and 4. The dynamic pressure model describes the early time distribution of pressure promoted by interaction of the projectile and target medium. By modeling attenuation characteristics of the target material and experimentally determining pressures at some distance away from the wound tract, the dynamic pressure model was used to determine time resolved pressure distributions local to the projectile. This enabled segregation of *base pressure drag* from lateral surface viscous effects in the retardation algorithm and contributed to development of a non-linear spring lattice that simulates projectile-soft tissue interaction and response. The data also enable a physical interpretation of parameters governing retardation of the projectile. This physical interpretation of model parameters is necessary to extend models initially being developed to describe projectile interaction with biosimulants, to human tissue.

From previous work (U.S. Army Natick Research, Development, and Engineering Center Contracts DAAK60-92-C-0003 and DAAK60-92-C-0008) an algorithm describing the retarding force per unit mass, $R(v)$, as a function of projectile velocity for a sphere in 20% ordnance gelatin was developed. This algorithm had the form of an n-dimensional polynomial in terms of the instantaneous velocity of a spherical projectile; i.e., $R(v) = a + bv + cv^2 + \dots$. The constant coefficients, a, b, c, \dots , were empirically determined and were specific to the projectile geometry-target medium combination.

In this effort, a second order polynomial was used to describe penetration of a sphere into 20% ordnance gelatin. In this polynomial, the a and cv^2 terms can be shown to be of similar magnitudes and identically equal for a projectile velocity of 873 fps. If the retarding force is divided by the presented area of the projectile, A , in the direction of motion to obtain pressure immediately in front of the projectile, the implausible result that pressure is of similar magnitudes at very high and very low projectile velocities, is obtained. This problem was

Table 3. Summary Descriptions of Ballistic Tests Implemented

SHOT #	TARGET	PROJECTILE	VELOCITY	RESIDUAL	TEMP.	DEPTH	PHOTO	INSTRUMENTATION	LOCATION	RANGE	PRESSURE
			(FPS)	(FPS)	(deg. F)	(IN.)			(IN.)	(IN.)	(PSI)
7/10/01	20%	1/4" STEEL SPHERE	490				YES	NONE	N/A	N/A	N/A
7/10/02	20%	1/4" STEEL SPHERE	1550				YES*	NONE	N/A	N/A	N/A
7/18/01	20%	1/4" STEEL SPHERE	1370				YES	FEMUR (LPT)	2.0	1	N/A
7/18/02	20%	1/4" STEEL SPHERE	1750				YES	FEMUR (LPT)	2.0	1/4	1240*
7/19/01	20%	1/4" STEEL SPHERE	1300				YES	2 PT'S IN FROM TOP	2.3/5.0	1/4	N/A
7/26/01	20%	1/4" STEEL SPHERE	2270				NO	HPT IN FROM TOP	2.4	1/4	2390
7/26/02	20%	1/4" STEEL SPHERE	1630				NO	HPT IN FROM TOP/LPT ON REAR	2.4/4.8	1/2	1070 / 240
7/26/03	20%	1/4" STEEL SPHERE	2160				YES	FEMUR (LPT)	2.0	3/4	1410*
7/31/01	20%	1/4" STEEL SPHERE	1840				YES	FEMUR (HPT)	2.0	3/4	N/A
7/31/02	20%	1/4" STEEL SPHERE	2170				NO	HPT IN FROM TOP	2.4	1/2	1250
7/31/03	20%	1/4" STEEL SPHERE	1760				NO	HPT IN FROM TOP	2.4	1/2	1100
7/31/04	20%	1/4" STEEL SPHERE	1870				YES	HPT IN FROM TOP	2.4	1/2	940
8/7/01	20%	1/4" STEEL SPHERE	2060*				YES	FEMUR (HPT)	1.7	3/4	2070
8/7/02	20%	1/4" STEEL SPHERE	160			0.35	NO	LPT IN FROM TOP	2.4	1/2	2.4
8/8/01	20%	1/4" STEEL SPHERE	205			0	NO	LPT IN FROM TOP	2.4	1/2	1.9
8/8/02	20%	1/4" STEEL SPHERE	320			0.65	NO	LPT IN FROM TOP	2.4	1/2	8*
8/8/03	20%	1/4" STEEL SPHERE	170			0	NO	LPT IN FROM TOP	2.4	1/2	1.7
8/8/04	20%	1/4" STEEL SPHERE	440			1.53	NO	LPT IN FROM TOP	2.4	1/2	12*
8/8/05	20%	1/4" STEEL SPHERE	250			0.54	NO	LPT IN FROM TOP	2.4	1/2	5.0
8/8/06	20%	1/4" STEEL SPHERE	2270				NO	2 PT'S IN FROM TOP (HPT & LPT)	2.3/5.0	1/2	1650 / 930
8/10/01	10%	1/4" STEEL SPHERE	1530				NO	HPT IN FROM TOP	2.4	1/2	N/A
8/10/02	10%	1/4" STEEL SPHERE	1610	890*			NO	HPT IN FROM TOP	2.4	1/2	660
8/10/03	10%	1/4" STEEL SPHERE	1570	770*			NO	HPT IN FROM TOP	2.4	1/2	1340
8/14/01	10%	1/4" GLASS SPHERE	2080			2.4/2.5	NO	2 PT'S IN FROM TOP (HPT & LPT)	2.3/5.0	1/2	424 / 120
8/14/02	10%	1/4" GLASS SPHERE	390			1.04	NO	NONE	N/A	N/A	N/A
8/17/01	20%	1/4" STEEL SPHERE	1940		9.8/9.6	YES	HPT IN FROM TOP*	2.4	1/2	1160	
8/17/02	20%	1/4" STEEL SPHERE	930			4.7	NO	NONE	N/A	N/A	N/A
8/17/03	20%	1/4" STEEL SPHERE	320			0.8	NO	NONE	N/A	N/A	N/A
8/17/04	20%	1/4" STEEL SPHERE	750			3.3	YES	NONE	N/A	N/A	N/A
8/17/05	20%	1/4" STEEL SPHERE	1150			5.6	YES	NONE	N/A	N/A	N/A
8/21/02	10%	1/4" STEEL SPHERE	1060	470*			NO	LPT IN FROM TOP	2.4	1/2	N/A
8/21/03	10%	1/4" STEEL SPHERE	370	< 50*			NO	LPT IN FROM TOP	2.4	1/2	N/A
8/21/04	10%	1/4" STEEL SPHERE	1230	550*			NO	LPT IN FROM TOP	2.4	1/2	N/A
8/21/05	10%	1/4" STEEL SPHERE	840	370*			NO	LPT IN FROM TOP	2.4	1/2	301
8/21/06	10%	1/4" STEEL SPHERE	2690	790*			NO	HPT IN FROM TOP	2.4	1/2	1915
8/23/01	20%	ALUMINUM CONE	1210			5.30*	YES	LPT IN FROM TOP	2.4	0	570
8/23/02	20%	ALUMINUM CONE	2050			*	NO	HPT IN FROM TOP	2.4	1/2	1950
8/23/03	20%	ALUMINUM CONE	2200			*	YES	HPT IN FROM TOP	2.4	1/2	4500
8/24/01	20%	BB	1320*		38	6.17*	NO	HPT IN FROM TOP	2.4	1/2	N/A
8/24/02	20%	BB	560		44	1.25	NO	NONE	N/A	N/A	N/A
8/24/03	20%	BB	560		56	1.73	NO	NONE	N/A	N/A	N/A
8/24/04	20%	BB	560		62	1.80	NO	NONE	N/A	N/A	N/A
8/24/05	20%	BB	560		70	2.25	NO	NONE	N/A	N/A	N/A
8/28/01	20% (COOL)	BB	560		44	1.17	NO	NONE	N/A	N/A	N/A
8/28/02	20% (COOL)	BB	N/A		44	5.49	NO	NONE	N/A	N/A	N/A
8/28/03	20% (COOL)	BB	1780		44	5.48	NO	NONE	N/A	N/A	N/A
8/28/04	20% (COOL)	BB	2010		44	6.20	NO	NONE	N/A	N/A	N/A
8/28/05	20% (COOL)	BB	1910		44	5.77	NO	NONE	N/A	N/A	N/A
8/28/06	20% (COOL)	1/4" STEEL SPHERE	1780			8.68	YES	HPT IN FROM TOP	2.4	1/2	910
8/28/07	20% (COOL)	BB	560		55	1.28	NO	NONE	N/A	N/A	N/A
8/29/01	20% (COOL)	BB	560		74	2.54	NO	NONE	N/A	N/A	N/A
8/31/01	20% (COOL)	1/4" STEEL SPHERE	1020		36	5.04	NO	NONE	N/A	N/A	N/A
8/31/02	20% (COOL)	1/4" STEEL SPHERE	1330		36	6.6/6.4	NO	NONE	N/A	N/A	N/A
8/31/03	20% (COOL)	1/4" STEEL SPHERE	740		36	3.28	NO	NONE	N/A	N/A	N/A
8/31/04	20% (COOL)	BB	560		36	1.17	NO	NONE	N/A	N/A	N/A
8/31/05	20% (COOL)	1/4" STEEL SPHERE	N/A		36	8.96	NO	NONE	N/A	N/A	N/A
8/31/06	20% (COOL)	1/4" STEEL SPHERE	1700		37	8.75	NO	NONE	N/A	N/A	N/A
9/5/01	20%	BB	2230		40	6.40	NO	NONE	N/A	N/A	N/A
9/6/01	20% (SMALL)	1/4" STEEL SPHERE	1570			8.3/8.1	NO	NONE	N/A	N/A	N/A
9/6/04	20% (LARGE)	1/4" STEEL SPHERE	840			3.6	NO	NONE	N/A	N/A	N/A
9/6/05	20% (LARGE)	1/4" STEEL SPHERE	1170			6.3/6.1	NO	NONE	N/A	N/A	N/A
9/12/02	20%	1/4" STEEL SPHERE	1520			7.5/7.3	NO	NONE	N/A	N/A	N/A
9/12/03	20%	1/4" STEEL SPHERE	1550	1000*		7.7/7.5	DOUBLE	None	N/A	N/A	N/A
9/18/01	20%	1/4" STEEL SPHERE	470			1.6	NO	NONE	N/A	N/A	N/A
9/18/02	20%	1/4" STEEL SPHERE	1350	933*		6.9/6.7	DOUBLE	None	N/A	N/A	N/A
9/18/03	20%	1/4" STEEL SPHERE	1510	641*		7.6/7.3	DOUBLE	None	N/A	N/A	N/A
9/26/01	20%	1/4" AL CONICAL ROD	N/A			10+	NO	HPT IN FROM TOP	2.4	1/2	1290
10/5/01	20%	1/4" AL CONICAL ROD	1710			10+	YES	HPT IN FROM TOP	2.4	1/2	1010

corrected by segregating dynamic and static components of pressure. That is, total pressure was scaled by the relative magnitude of the dynamic pressure that must be a maximum at the time of projectile entry into the target. This is shown below

$$\left(\frac{R(v)}{A}\right)\left(\frac{\rho v}{\rho v_0}\right)^2 = \left(\frac{R(v)}{A}\right)\left(\frac{v}{v_0}\right)^2$$

where v_0 is the projectile striking velocity and ρ is the target media density.

Another enhancement included addition of the following term

$$\exp\left[\frac{-\alpha R}{Q(\omega)}\right]$$

to describe pressure attenuation with distance and dispersion or frequency dependence of attenuation. In this expression α is the attenuation coefficient, αR describes attenuation due to geometric scattering where R is radial distance, and $Q(\omega)$ describes dispersion of pressure as a function of frequency, ω . In the dynamic pressure model the resulting expression is integrated over time for a moving line source. The waves arriving from the various sources are then accumulated at field points to describe time-resolved pressure at a particular location away from the wound tract.

The approach described above was used to predict pressure away from the projectile trajectory for the experimental configuration shown in Figure 30. Calibration tests were conducted using, pressure transducers that were not cast in the gelatin (as they were in subsequent tests) but were bonded to plates that rested on the free surfaces of the gelatin. (The transducers were therefore held in compression and wave reflection between the free surface and the transducer configuration promoted occurrence of high frequencies in the traces shown in Figure 31 and Figure 32).

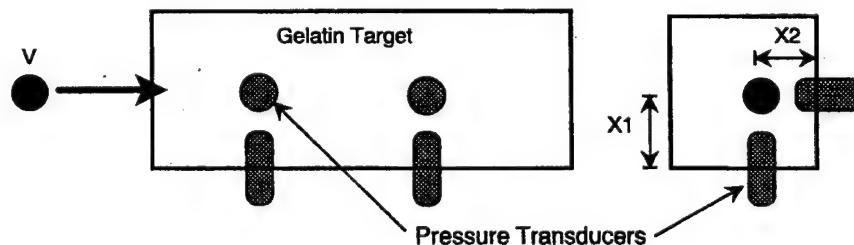


Figure 30. Ballistic Test Configuration

The calibration experiment involved ballistic penetration of a 1.04 gram, 0.250-inch diameter steel sphere striking 20% ordnance gelatin at 1370 feet per second. The total penetration of the sphere was 7.0 inches. Pressure transducers were located at three and six inches from the struck edge of the 4.5 x 5 x 9.75-inch gelatin target. The x_1 and x_2 dimensions were 1.5 and 3.2 inches.

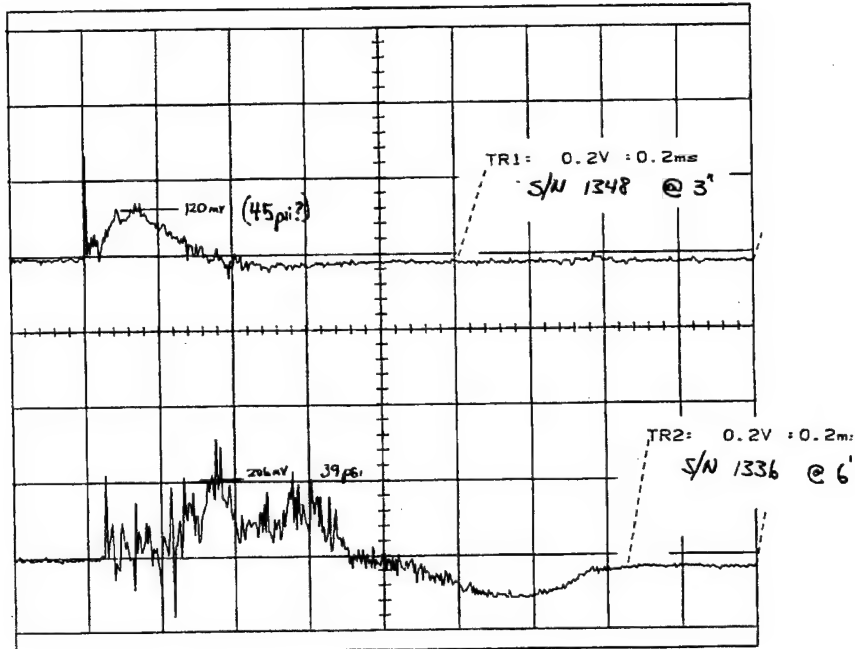


Figure 31. PCB Transducers 1.5 inches from Trajectory at 48 μ sec

The purpose of this calibration experiment was to define time synchronization and frequency response requirements for subsequent experiments since instrumentation circuitry had to be built and the frequency response (and filter strategy) of the pressure transducers had to be determined. Since data was generated however, albeit difficult to interpret, the data was used to determine if order-of-magnitude agreement could be obtained by exercising preliminary models.

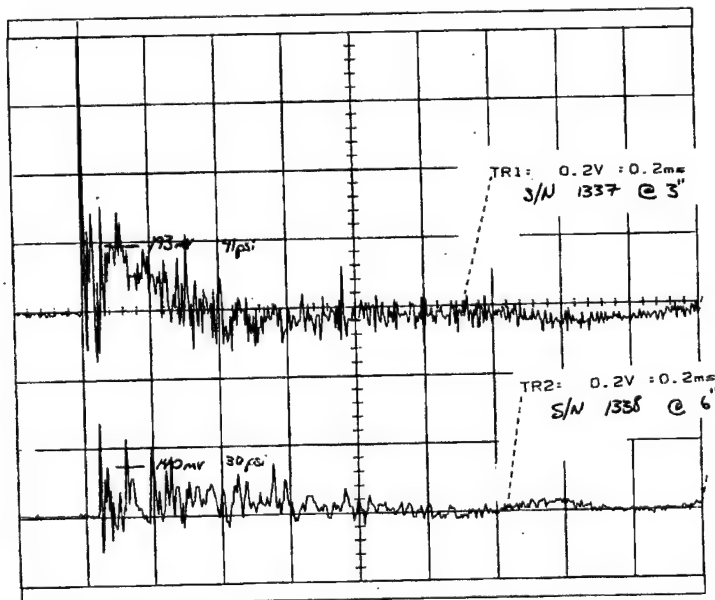


Figure 32. PCB Transducers 3.2 inches from trajectory at 40 μ sec

Traces from the four transducers are shown in Figure 31 and Figure 32. Figure 31 shows traces of pressure versus time from sensors located on a plane 1.5 inches from the trajectory at 3 and 6 inches from the impact surface of the gelatin target. The peak pressures associated with the initial expansion of the temporary cavity are 45 psi at 3 inches and 30 psi at 6 inches. These peaks occur at 0.6 and 1.8 msec, respectively. Similar results for a plane 3.2 inches from the trajectory is shown in Figure 32 where peak pressures of 41 and 30 psi is developed at 0.5 and 0.6 msec.

A comparison of Figure 31 and Figure 32 show in both cases an initial high frequency peak which is not very well resolved and low frequency response where associated amplitudes are attenuated between 10 and 30%. The analytical model predicts peak dynamic pressures at these locations between 40 and 80 psi. The prediction assumed that the attenuation coefficient was identically equal to zero and the velocity of the displacement field normal to the projectile motion was between 0.1 and 0.2 of the projectile velocity. This estimate was based on empirical observation of high-speed movies of other experiments. As explained below the displacement field normal to the projectile motion is critical for determining the initial conditions for the non-linear spring lattice. Figure 33 and Figure 35 show predicted pressure versus change in velocity and projectile velocity versus time.

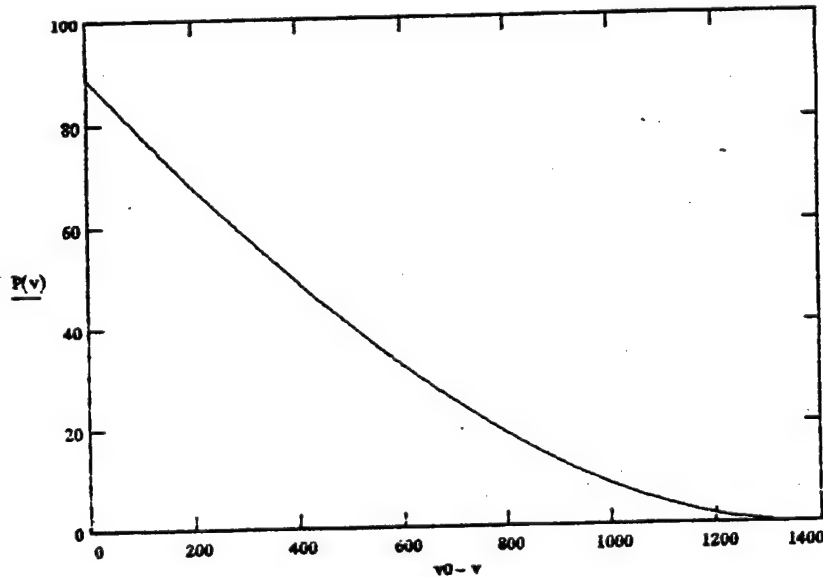


Figure 33. Predicted Pressure versus Change in Velocity (v_0 is the striking velocity and v is the instantaneous projectile velocity)

A lattice of non-linear springs is envisioned to describe the mechanical response of soft-tissue. This is depicted in Figure 34. The high frequency portion of the power spectrum promotes damage and the energy content of these frequencies dissipate rapidly due to conversion of energy into mechanical work. The initial model was one-dimensional where spring constants were modeled as a quadratic equation: $k_1x + k_2x^2$ and assumed elastic unloading. This model was expanded to a two and then three-dimensional lattice. A more general formulation of the spring

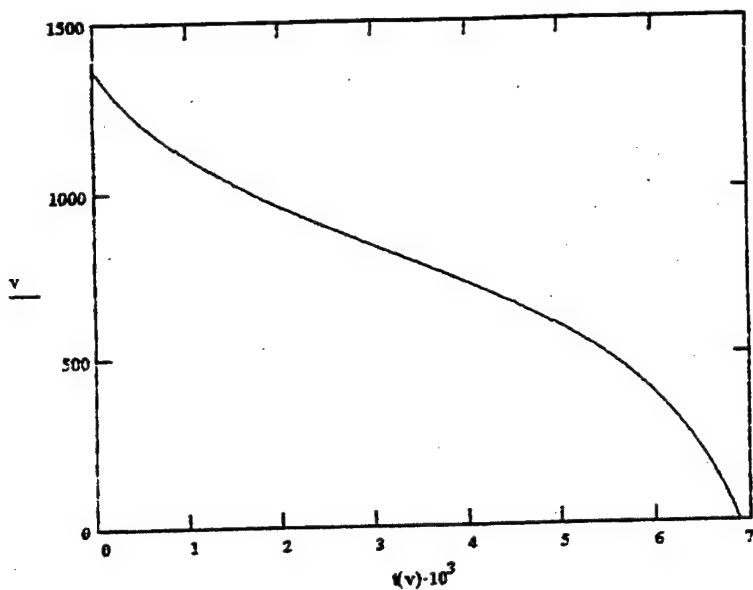


Figure 35. Predicted Velocity in Feet per Second versus Time in Milliseconds

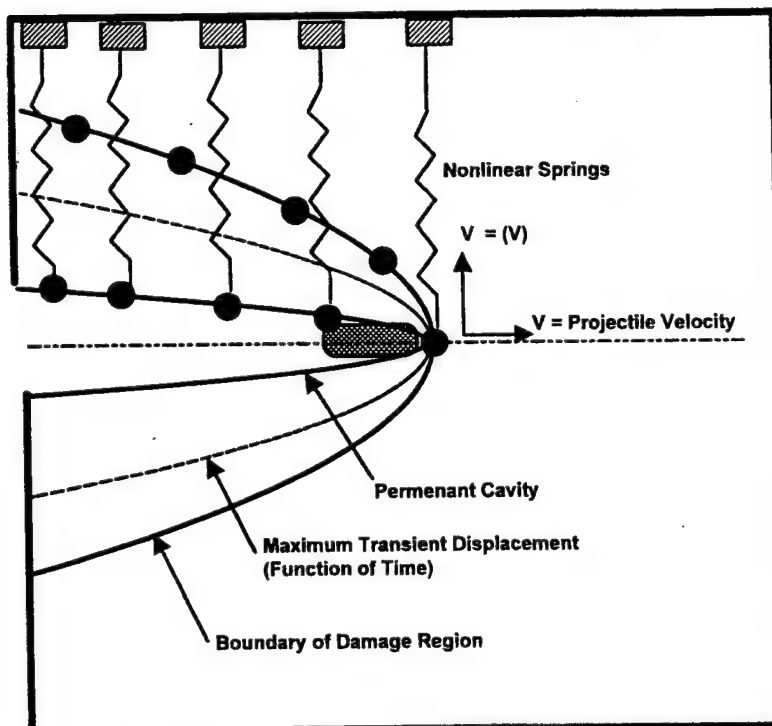


Figure 34. Schematic of Non-Linear Spring Model

constants and unloading function was also developed based on the mechanical stress-strain curve of relevant tissue. Development of the model depicted in Figure 34 highlights four theoretical issues discussed in items *i* through *iv* below.

(i) ***Development of the Projectile Retardation Algorithm.*** The first problem concerns development of the projectile retardation algorithm. Two insights from previous work at MRC (DAAK60-92-C-0003 and DAAK60-92-C-0008) demonstrated that: (a) Close approximations of the retarding force on spheres of different dimensions can be obtained by knowing the retarding force on a prescribed sphere and scaling the force by the ballistic coefficient of the unknown sphere, and, (b) For certain velocity regimes, lift and drag forces on a projectile penetrating a tissue simulant can be determined by representing a projectile as an ensemble of spheres and integrating the retarding force on each sphere over the geometry of the projectile. This last problem is a complicated highly non-linear integration since the center of projectile rotation and integration limits change with time. These two insights however reduce the original problem of determining the detailed forces acting on a projectile during penetration (which is probably intractable) to the problem of determining the retarding force per unit mass on a sphere.

Currently, the model used to determine the retarding force on a sphere is semi-empirical and is described in detail in Section 2. A goal of the current effort is to develop the retardation model in terms of physical properties of the projectile and target media so that the model can be used to describe what occurs in a living person with the appropriate substitution of tissue properties. A problem that frustrates this strategy is the fact that target properties change with projectile penetration velocity. To circumvent this difficulty, properties of the target medium at limiting physical states (i.e., a viscous fluid at high penetration velocities and a viscoplastic solid at low penetration velocities) where target properties are well defined (and a database exists for human tissue); are used to construct a relation between retarding force and penetration velocity.

It was shown in Section 2 that the low and high velocity asymptotes that describe projectile retardation can be represented as an infinite series where the first term in each series dominates. It was further shown that the first term in the high velocity asymptote could be related to the physical density of the target medium and the drag coefficient of the projectile. Further, the ultimate mechanical static can be related to the first term of the low velocity asymptote. However, this property(s) was not well defined and remained to be established. Without this set of properties being rigorously defined, the models being developed in this effort can not be confidently extrapolated to human tissue.

(ii) ***Determination, as a Function of Projectile Velocity, Initial Particle Velocity Transverse to Projectile Motion.*** This problem concerns determination of the initial velocities on the various chains of the non-linear spring lattice intercepted by the projectile (see Figure 34). A videotape acquired from Dr. Ronald Bellamy, Col., USAMC shows an AK74 projectile penetrating 10% ordnance gelatin photographed at 20,000 frames a second. Unfortunately, no timing information was conveyed on the tape and the framing rate is non-uniform (since it takes time for the camera to accelerate to the prescribed rate of 20K frames per second). However, it is estimated that the displacement velocity normal to the projectile trajectory is approximately 10 to 20% of the projectile penetration velocity.

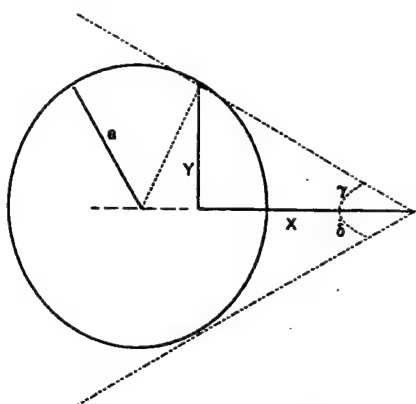


Figure 37. Schematic and Nomenclature of Boundary Layer Separation from Sphere

The problem of developing a model to more generally describe the transverse displacement field is alluded to in Figure 37 where a schematic of a sphere penetrating a viscous medium is shown. The dashed triangular region with subtended angles γ and δ represent the boundary layer. If the transverse particle velocity of the target medium can be represented as $\dot{y} = \beta v$ where v is the projectile velocity and β is an undetermined coefficient and the point at which the boundary layer separates from the surface of the sphere. The boundary layer separation can be further represented by the subtended angle α that is a free parameter. The α and β parameters can be shown to be related as shown in Figure 36. Analytically Predicted $\beta = \beta(\alpha)$. In Figure 36. Analytically Predicted $\beta = \beta(\alpha)$, for $\beta = 0.2$ (i.e., transverse particle velocity of target media is 20% of projectile velocity) the point of boundary layer separation corresponds to subtended angle of $\alpha = 0.02$.

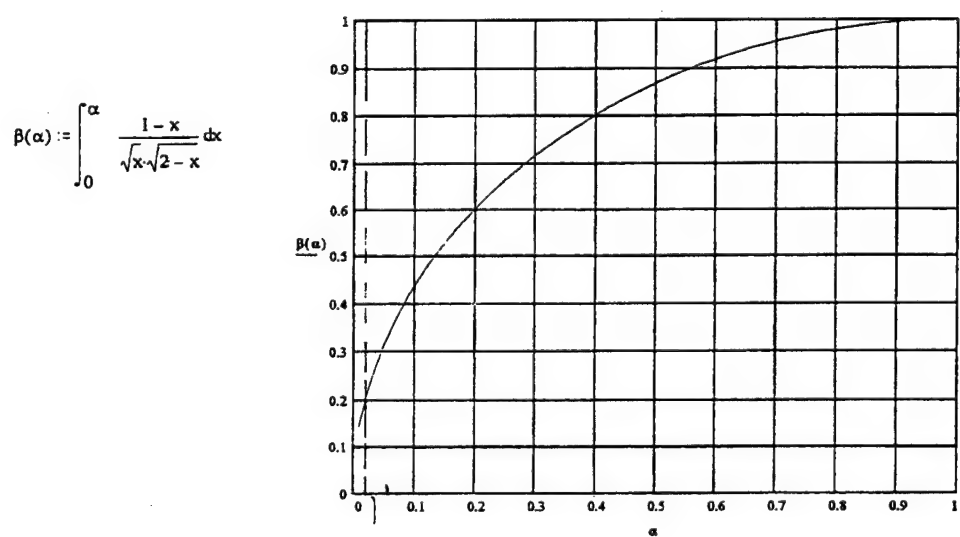


Figure 36. Analytically Predicted $\beta = \beta(\alpha)$

The problem then reduces to two issues. The first issue is how to predict α for different projectile geometries, striking conditions, projectile velocities, and target media. Second, knowing the distribution of $\alpha = \alpha(v)$ and v as a function of penetration depth, transverse velocities must be mapped onto the correct chain of springs. This issue is related to the viscosity of the tissue and how much the boundary region stretches and sticks to the surface of the projectile before the boundary layer sheds. Ballistic experiments were designed to gain insight into both of these issues and are explained below.

Projectile geometries included a sphere, conically sharp cylinder that was confined to prevent yaw, and a cylinder launched at a prescribed yaw. Each of these geometries was expected to produce very different trends in transverse target particle velocity. For example, the boundary layer should remain attached to the conical surface of conically sharp cylinder. In the expression $\dot{y} = \beta \dot{x}$ described earlier where \dot{x} is the projectile velocity in the direction of the projectile motion and \dot{y} is the transverse particle velocity promoted in the target by the projectile motion, β should be a constant. The maximum extent of the temporary cavity and the extent of the residual cavity should therefore be linearly proportional to the velocity history of the projectile. In the case of a sphere the separation point will be a function of velocity and therefore $\beta = \beta(v)$. The cylinder will be the most challenging geometry in that the rotational kinematics of the cylinder will result in a time dependent leading edge geometry.

From ballistic experiments using military bullets, the permanent wound tract is seen to be highly non-uniform. This is due to the rotational kinematics of the projectile changing the leading edge geometry and presented area of the projectile in the direction of motion as well as the variation in projectile velocity. Second, there are a lot of radial fractures associated with passage of the projectile. The presence of these radial fractures highlights two additional issues. First, how does this type of mechanical damage translate to the human body? Second, how is the size of the temporary cavity measured. Traditionally, this has been based on photographically observing a discontinuity in the optical properties of the target or change in the target index of refraction over time.

This may be very misleading however since the fractures form at about the bulk sound speed of the material (about 5,000 ft/sec). This is on the order of tens of microseconds. The temporary cavity however forms on the order of milliseconds. The observed changes in target optical properties are therefore very likely due to diffraction patterns caused by pre-existing fracture planes opening and closing. These diffraction patterns may completely obscure observation of the temporary cavity.

These difficulties were addressed by construction of an array of light tubes that will back light the target and are located perpendicular to the film plane. The tubes were made from ABS plastic with stainless steel shim stock inserts. The tubes were 3.5 inches in diameter and 13 inches long with xenon flash lamps (1 microsecond on/off). The purpose of these tubes was to produce an intense highly diffuse light source that will tend to demphasize diffraction effects when photographed. Additionally, gelatin targets were constructed with specific types of defects fabricated into the targets. The pre-damaged blocks were photographed with the constructed light source so that more reliable inferences can be made regarding the interpretation of photographed features.

(iii) **Tissue Damage Criteria.** The residual cavity from a penetrating injury results from initial damage promoted by the distribution of pressure associated with the projectile motion. The damage can also be enhanced after passage of the projectile. This later damage is associated with transient displacement of the target medium and elastic recovery of the material behind the projectile. In both cases a stress field is promoted which can strain tissue beyond the elastic limit of the respective tissue. When tissue damage occurs, elastic properties of the tissue can be degraded and/or stress concentrations can be promoted. This alters the time-resolved description of the stress and strain fields in the neighborhood of the wound tract. The accumulation of inelastic strain over time however governs the geometry of the wound tract and adjacent tissue damage. Therefore, damage criteria are required for the various tissues affected which describe the nature of the damage and at what levels of stress/strain the damage occurs.

This issue also relates to the initial velocity promoted by the projectile motion in the transverse direction. When the projectile interacts with the target, material stretches around the projectile and eventually breaks. The tensile stress at which the target material around the projectile eventually breaks can be analytically related to the transverse particle velocity of the target material, the subtended angle on the projectile surface at which the boundary layer separates, and initial conditions on the various chains of springs in the lattice.

(iv) **Tissue Prestress.** *In vivo* tissues are generally stressed. If an artery is cut, it will shrink away from the cut. A broken tendon retracts and the lung is in tension at all times. Pre-stress at the time of wounding may significantly influence the geometry of the wound. This is particularly true since biological materials deviate from Hooke's law (i.e., the relation between stress and strain is non-linear). At a minimum, some approximation of the pre-existing stress state of the affected tissues may have to be superimposed on the stress field resulting from the projectile interaction with the tissue. This pre-existing stress state may vary with activity as different muscles and tendons react during task performance. At a maximum, the pre-stress may influence the mode of damage. This is likely to be the situation with bone tissue where the fracture mode can be affected. Unfortunately, virtually all of the ballistic testing reported in the literature has been done on unstressed tissue. In the case of autopsies, the activity, and therefore kinematic state of the various muscles and tendons at the time of wounding is not known.

3.1 BALLISTIC IMPACT OF SPHERICAL PROJECTILES INTO 10% AND 15% ORDNANCE GELATIN

Tests were conducted at a nominal striking velocity of 1,400 feet per second, using 1/4-inch spherical steel projectiles. Ordnance gelatin targets were fabricated in the shape of rectangular prisms, measuring nominally 5 x 5 x 10 inches. All but two blocks were cast with two pressure probes installed, on centerline and nominally 0.5 inches above the projectile trajectory. Spacing from the striking surface was 1.50 and 4.20 inches respectively. The extent of the temporary cavity was assumed to be given by the dimensions of the diffraction pattern recorded on film, using backlit flash photography. Testing started testing with 10% gelatin and then progressed to 15% and 20% gelatin.

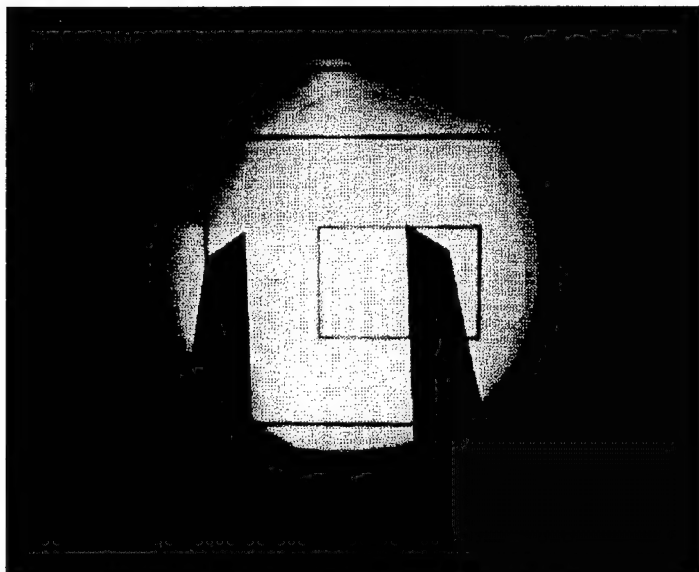


Figure 38. Shadowgram to show scale of subsequent photos (caliper open 1 inch)

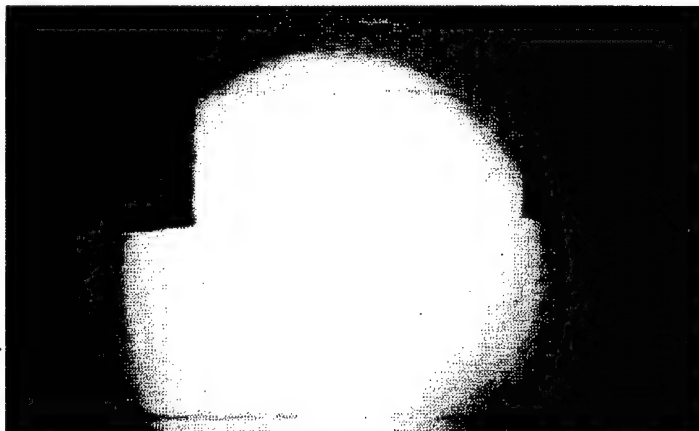


Figure 39. Shadowgram at 0 microseconds in 10% ordnance gelatin

287 microseconds after impact; the first transducer showed a rise 47 microseconds after impact and transducer two responded 66 microseconds later, or somewhat slower than the sound speed. Based on the photo in Figure 41, the temporary cavity has nearly engulfed the first transducer at that time and the transducer shows near zero pressure.

We then progressed to 15% gelatin. It had become clear that the temporary cavity would continue to expand, well after the times that were documented and therefore was not of interest. The photo of Figure 42 was recorded 286 microseconds after impact on a 15% gelatin block at a somewhat lower velocity (nominally 1,200 Ft/sec). Pressure pulse arrival times were 29 and 71 microseconds later. It was noted with interest that the presence of the pressure probe influences the growth of the temporary cavity. To address this issue, we attempted to record a late time photo of the temporary cavity that would engulf the probes. The photograph of Figure 43 resulted when the flash was fired 2,095 microseconds after impact.

Figure 38 was taken to establish proper scaling of detail in the photographs. It shows a backlit image of calipers, opened to 1.000 inches, placed in the position of the projectile trajectory. The rectangular patterns visible in the photograph are present on the optical random diffuser used in the illumination beam and are not used in these experiments.

The photographs in Figure 39 through Figure 41 are from different shots but may be viewed as the progression of the development of the temporary cavity, which has been defined here as the boundaries of the recorded optical diffraction patterns in 10% ordnance gelatin. Figure 39 shows the image of the two pressure probes in the gelatin target, before impact. Figure 40 was recorded 106 microseconds after impact, with the projectile clearly visible directly below the first transducer. The first transducer showed a pressure pulse arriving 35 microseconds after impact and transducer two showed a pressure rise 55 microseconds later, or 16 microseconds before the flash recorded the picture of Figure 40. The arrival times of these pressure pulses were consistent with sound speeds in the target material. Figure 41 was recorded



Figure 40. Shadowgram at 106 microseconds in 10% ordnance gelatin

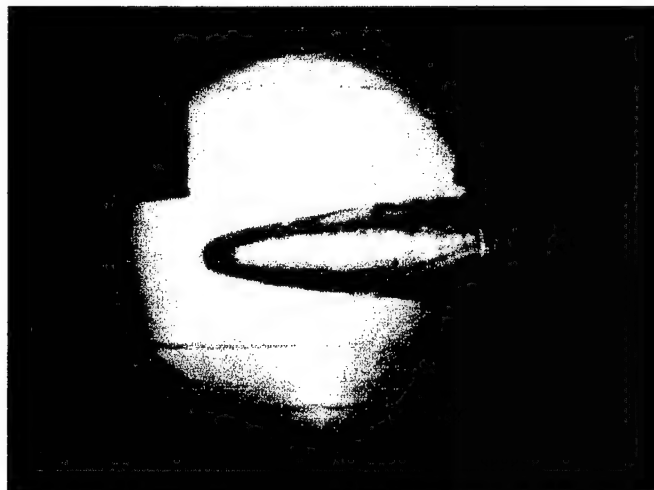


Figure 41. Shadowgram at 287 microseconds in 10% ordnance gelatin

The influence of the probes on the geometry of the temporary cavity is spectacular. Also it is clear that contact between the gelatin and probes cannot be assured for late time events. Pressure traces recorded after the arrival of the temporary cavity are clearly not useful.

To document the growth of the temporary cavity in the absence of probes we recorded the shadowgram of Figure 44, also 2,095 microseconds after impact, into an uninstrumented gelatin block. It seems that the diameter would continue to grow; we estimate to 2.0 inches maximum or 8 projectile diameters.

Measurements of the permanent wound track, unfortunately, are difficult because the target material easily tears and also changes shape due to moisture loss. Figure 45 contains back lighted photographs of the permanent wound tracks, one with pressure probes and the other without. There appear to be no significant differences between the two tracks. It can then be concluded that the effect of the presence of the pressure probes is limited to the formation of the temporary cavity.

Figure 46 was obtained during a check-out shot. Here we used a previously tested gelatin block with a permanent wound track and a spherical projectile imbedded in it, turned on its side. The shadowgram was recorded 2,000 microseconds after impact. The temporary cavity looks quite similar to the late time cavity of Figure 42, except near the rear (exit) surface of the block. It seems that the free surface effects have created the necked down temporary cavity structure visible and are also responsible for the appearance of the dark ring, concentric with projectile trajectory and visible on the rear surface. The cause of the ring's appearance is currently not definitively known.

It is also interesting to observe that the previously straight, pre-existing wound track was displaced on the order of 1/4 inch in the direction of the bullet travel. Thus, the gelatin is not only moving radially outward to form the temporary cavity, but also longitudinally, in the



Figure 42. Shadowgram in 15% gelatin recorded 286 micoseconds after impact

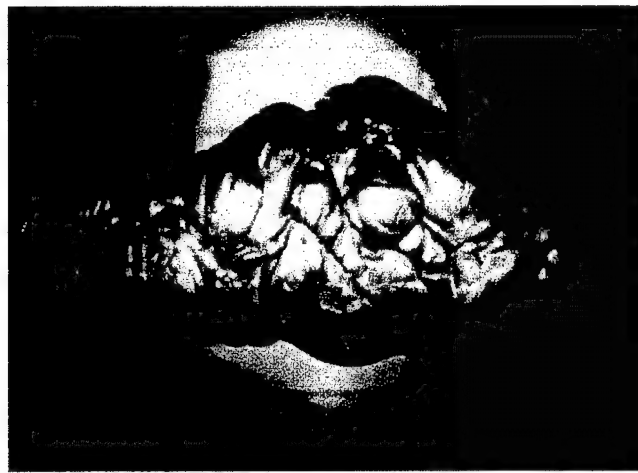


Figure 43. Shadowgram in 15% gelatin with pressure transducers and recorded 2.095 msec after impact

projectile entering the block on the lower trace and the response of the first transducer. The elapsed time from screen to transducer is 29 microseconds which is consistent with the sound speed of the material. The amplitude of the first peak is nominally 900 psi and the second peak is 1,200 psi. The early arrival time of pressure pulses of this magnitude is not consistent with our expectations for striking velocities well below the sound speed in the target material. The total duration of the pressure pulse is on the order of 140 microseconds which is probably dominated by reflected waves from the boundaries of the block.

Figure 48 shows data from the same test; the lower trace shows the time firing of the flash correlated with the response of the second transducer. The pressure pulse shape is quite different from the first pulse and the maximum pressure reached is 1,350 psi. that is probably to be taken as equal to the first pulse. The difference in the profile shape is probably attributable to the influence of reflected waves from the sidewalls. The flash, which yielded the photo of Figure 42

direction of projectile travel, as discussed in Section 2 relative to the "sticking hypothesis" of the target medium on the projectile.

The absolute magnitudes of the pressures recorded are probably not meaningful except for the very first response of the pressure probes. After that, the large-scale displacement of the material around the probes and probe mounts will cause local and temporary separation of the material from the transducers, followed by the unpredictable collapse of these cavities. We are comfortable only reporting the magnitude of the first pressure spike that arrives at each probe. The rest of the traces may not be useful. Unfortunately we have also consistently underestimated the magnitudes of the early time spikes so that the traces initially exceeded the range available in the storage medium. From these traces we have only retrieved arrival times of the pressure pulses at the transducers, as correlated with the entry event (ballistic screen) and firing of the Xenon flash producing the shadowgrams.

For run 5-22-01, which produced the late time image of the temporary cavity, as shown in Figure 42, we reduced the sensitivity of the storage scope to reveal the peaks as seen by the two pressure probes. Figure 47 shows the screen event of the

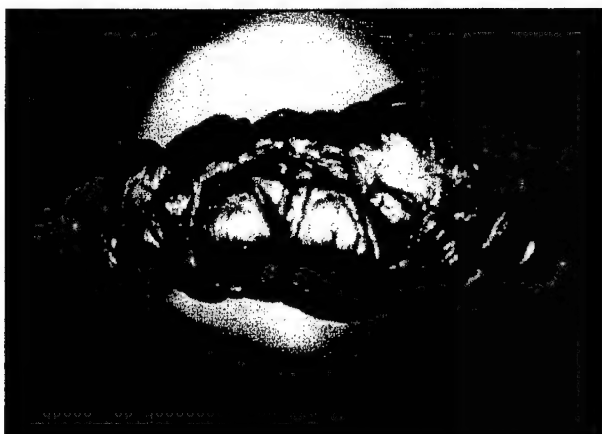


Figure 44. Shadowgram recorded 2.095 msec after impact in 15% gelatin without pressure transducers

uncertainties from events that do not have a very crisp rise and are recorded at rather slow writing speeds.

It seems quite clear from the above considerations that high-pressure pulses are observed that are transmitted at or near sound speed and are not significantly attenuated over distances on the order of inches. The physical significance of pressure indications after this postulated shock passage is unclear. The arrival of the boundary of the temporary cavity at the transducer face does not appear to be accompanied by a significant pressure rise. Pressures measured at late time, typical of maximum temporary cavity extent are near zero and slightly negative; i.e., sub-atmospheric. As stated previously, at the present time we cannot be sure that these measurements have physical significance.

It is expected that the response of the instrumented gelatin targets may be analogous to what can be expected when bone is present, surrounded by large amounts of soft tissue, like a thigh. If the projectile does not impact the femur, then initial damage to the femur must be the result of the pressure loading from the striking event. If the earlier claim of minimal attenuation over short distances is valid, then

is seen to have occurred much later than the pressure pulses, 2.020 milliseconds after pulse arrival at the second transducer. Thus the growth of the temporary cavity is seen to lag far behind the pressure pulse.

The data presented in Figure 47 and Figure 48 is temporally correlated by an independent measurement (not shown) of the elapsed time between ballistic screen and flash; in this case, 2.095 milliseconds. The time between pressure pulse arrival at probes one and two is calculated by subtracting two large numbers, yielding an interval of 41 microseconds. This would suggest faster than sound speed transmission but is more likely attributable to measurement

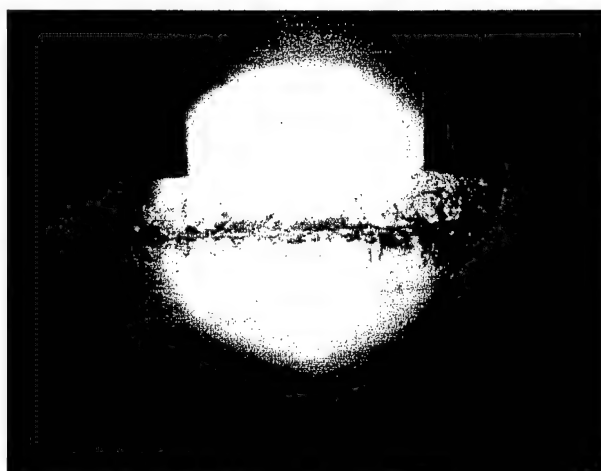


Figure 45. Residual cavities in 15% ordnance gelatin. (Top) in presence of pressure transducer, and (Bottom) without probes.

the probability of a femur fracture is not strongly dependent on close proximity of the femur to the wound tract. Rather, the striking conditions seem to dominate. Based on very limited data at this point, it seems that a pressure pulse on the order of 1,000 psi with tens of microseconds duration might cause a bone fracture. Further, analysis and testing is required to substantiate this however.

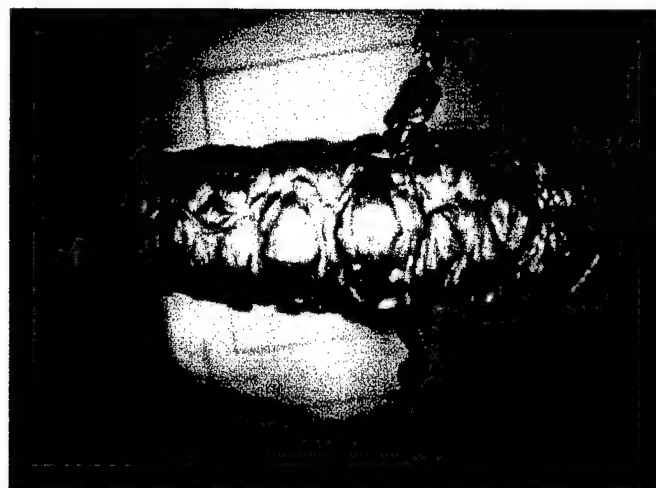


Figure 46. Late-time cavity in 15% gelatin target with pre-existing residual cavity orthogonal to trajectory

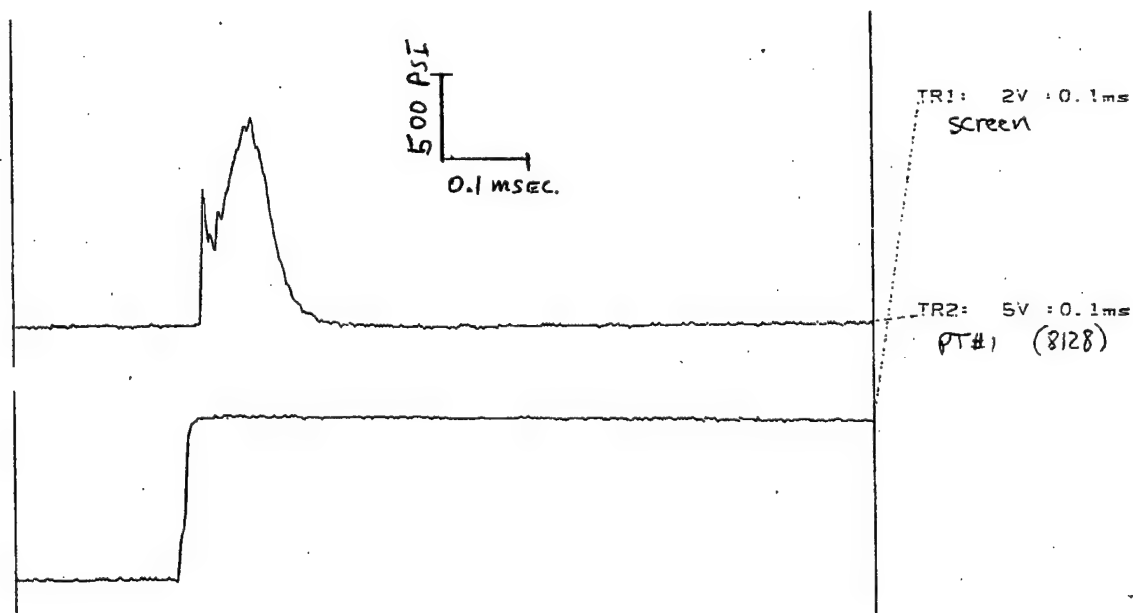


Figure 47. Traces from Break Screen and Pressure Transducer 1

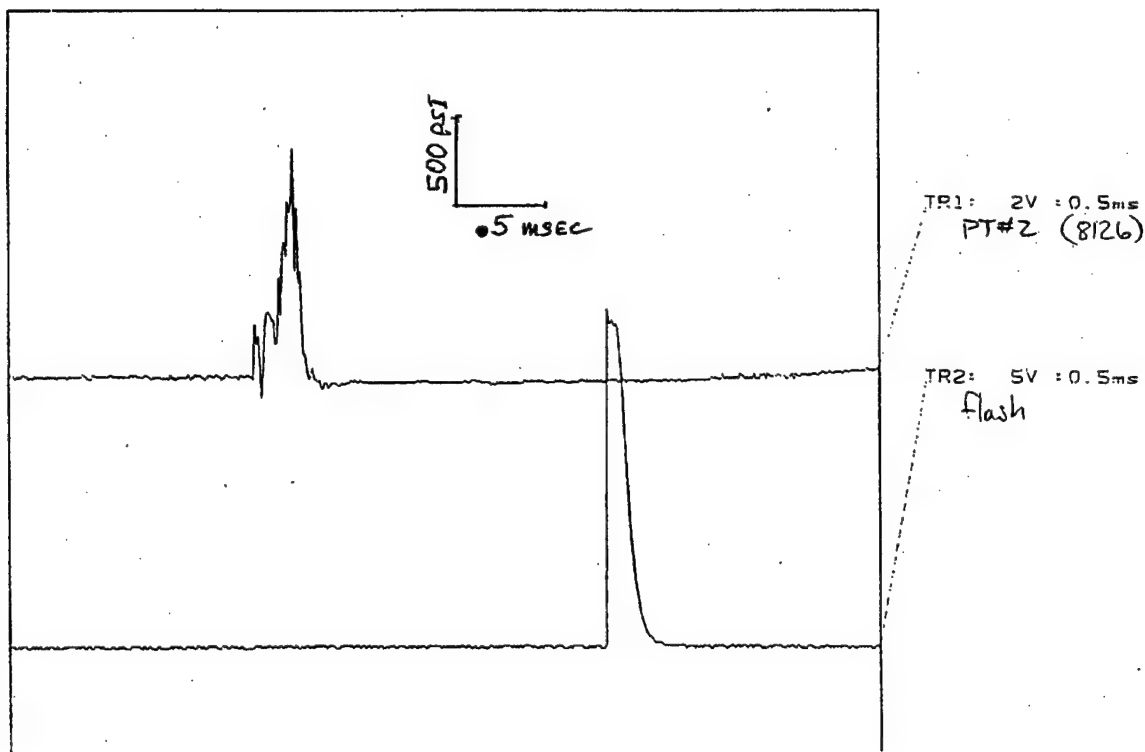


Figure 48. Traces from Flash Detector and Pressure Transducer 2

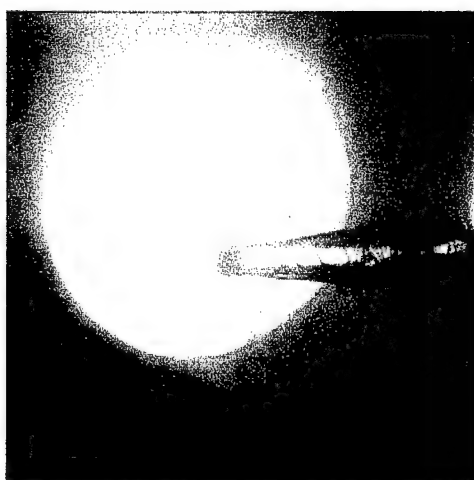


Figure 49. Spherical projectile with impact velocity of 490 fps at 1.1 msec after impact



Figure 50. Spherical projectile with impact velocity of 1,870 fps 107 microsec after impact

3.2 BALLISTIC IMPACT OF SPHERICAL PROJECTILES INTO 20% ORDNANCE GELATIN



Figure 51. Residual cavity in 20% gelatin target



Figure 52. Spherical projectile with impact velocity of 1,300 fps 220 microsec after impact

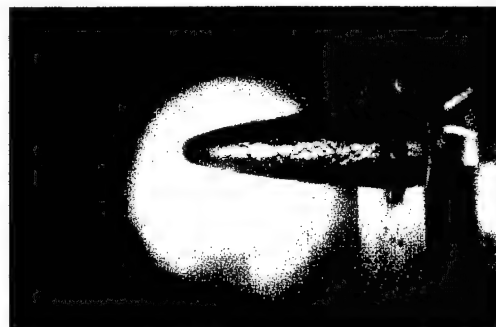


Figure 53. Spherical projectile with striking velocity of 1,870 fps 107 microsec after impact

Testing was initiated on 20% gelatin blocks, some with and some without pressure probes. The target geometry remained the same, namely a rectangular block, 5 by 5 by 10 inches, with the first and second pressure probes located 2.4 and 5.0 inches downstream of the impact surface. The photographic scale remained identical to the fiducial shown in Figure 38. Some photographs include a shadow image of a vertical needle. This fiducial is located 2.00 inches downstream from the impact surface.

The shadowgraph of Figure 49 shows a typical diffraction pattern resulting from a low impact velocity in 20% gelatin. The appearance of the temporary cavity is quite similar to typical, early time, cavities produced in 10% and 15% gelatin with little detail visible. A more revealing picture is shown in Figure 50 for a significantly higher impact. The similarity with the late time pictures of Figure 43 and Figure 44 for 15% gelatin is apparent. Basically, the extent of the cavity is a little smaller in 20% gelatin as expected but the scale of "turbulence", i.e., the size of the diffraction cells is similar. A post test photograph (Figure 51) recorded at the same location reveals the permanent cavity which is also similar to the 15% data of Figure 45.

It was pointed out in that pressure response, as measured by the probes installed in the gelatin targets occurs quite early in the penetration process. It was therefore reasonable to attempt to record the early time response of the temporary cavity coinciding with the pressure rise and fall indicated by the pressure transducers. The temporary cavity, recorded 0.22 msec. after impact is

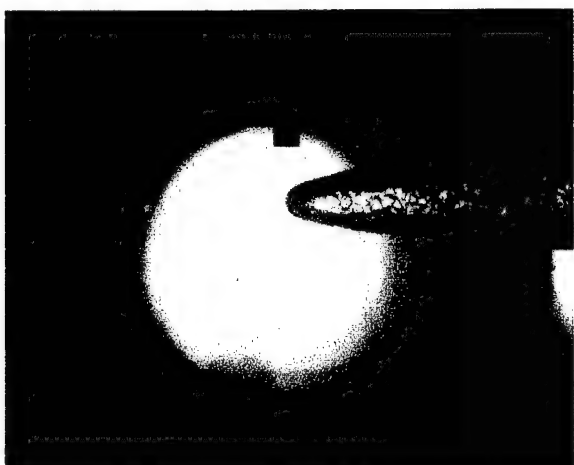


Figure 54. Spherical projectile with striking velocity of 1,940 fps 133 microsec after impact (small probe)

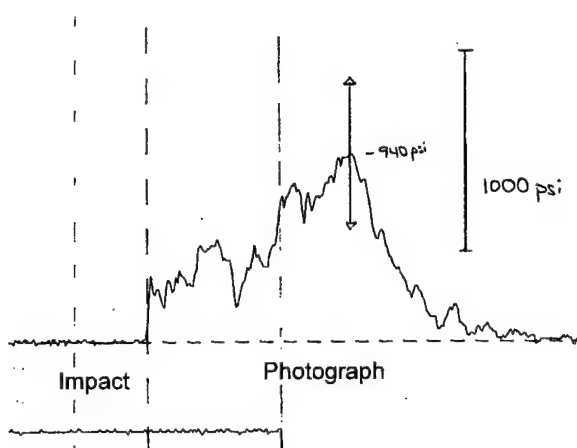


Figure 55. Time resolved pressure pulse for Figure 7 test

the different amplification and magnification of the two figures but show good agreement. From these observations it was concluded that the size of the probe mounting structure does not alter the measured response of the transducer. Testing was therefore continued using the rigid structures.

To complete the pictorial presentation of the growth and collapse of the temporary cavity we conducted tests at very early and very late times. Temporary cavities in 20% gel were recorded without pressure probes, at a nominal striking velocity of 1,000 ft/sec.

nicely depicted in Figure 52; unfortunately the pressure transducer failed to trigger the recording medium. The test was then repeated with a shorter delay to attempt to capture the shadowgram near the peak pressure. A predictable temporary cavity was recorded in Figure 53 and the recorded pressure response is shown in Figure 55. The transducer started to respond about 60 μ sec before flash and reached a peak value of 940 psi, about 40 μ sec. after flash. The onset of the pressure rise is consistent with shock arrival times, based on wave speeds. The peak pressure value is typically observed when the projectile is closest to the probe.

The mounting structure designed and built for the purpose of installing and protecting the piezoelectric transducers from pressure pulses that might exceed several thousand psi or direct particle impacts were relatively rigid and massive. To investigate possible importance of these structures in influencing the gelatin response, a test was performed using a minimal supporting structure on one of the transducers. The resultant shadowgram of Figure 54 was recorded 133 μ sec after impact, and shows the extra light structure of the transducer mount. The temporary cavity in Figure 54 is very similar to those shown in Figure 52 and Figure 53 with large probes. The pressure measurement obtained with the "light" probe is shown in Figure 56. A comparison of this trace with that of Figure 55 is a little complicated by

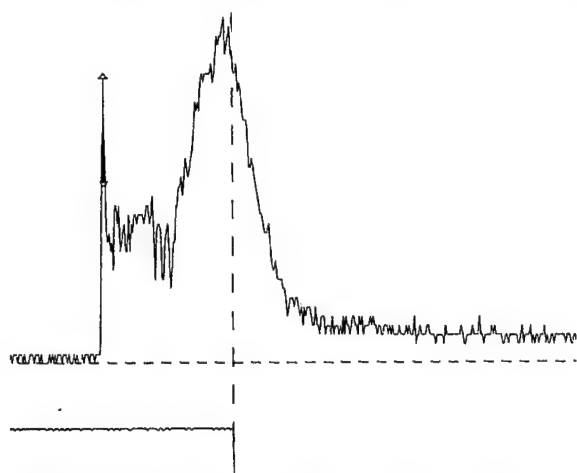


Figure 56. Time resolved pressure pulse for experiment in Figure 8

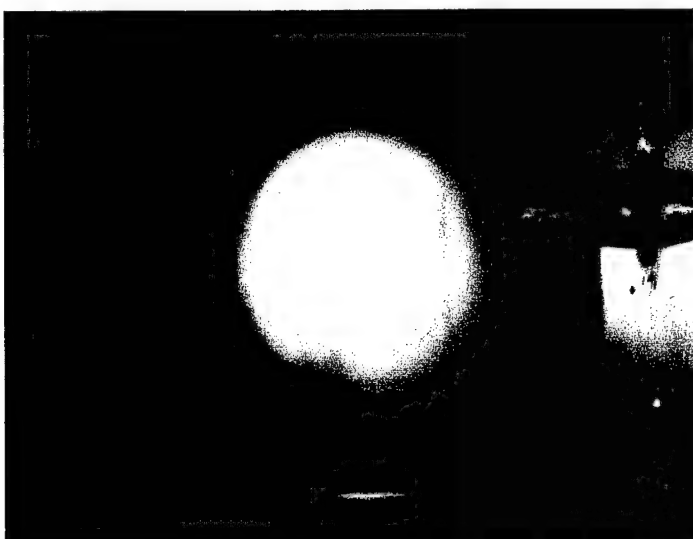


Figure 58. Spherical projectile with striking velocity of 750 fps 88 microsec after impact



Figure 57. Spherical projectile with impact velocity of 1,150 fps 2.730 msec after impact

Figure 58 shows the temporary cavity recorded 88 μ sec after impact and Figure 57 shows a cavity recorded nearly 2.73 msec after impact. The early cavity is much as expected. The partial mirror image of the cavity seen on the impact surface is not fully understood however. That surface also seems to be showing an upheaval, typical of a surface wave or crater formation.

The late time photo shows a substantially collapsed cavity, which seems to have closed at the entrance site. The evident fringe-like rings on the impact surface would also seem to be the result of a surface wave, radiating outward from the impact site. Further studies would seem to be of interest, in particular, since impacts on live tissue are known to produce significant surface upheavals and ejecta.

To further address issues of wave propagation, transit times and arrival times, a single test was conducted with one pressure probe in the forward (2.4") in depth installation and a second probe mounted flush on the rear surface of the gelatin block. The response of the first transducer (standard location) is shown in Figure 59 to be similar to the pulses from similar experiments. The trace shown in Figure 60 was recorded with the transducer on the rear surface, some

5 inches from the impact site. The two traces are temporally correlated by the flash event. The two peaks marked in Figure 60 are consistent with the arrival times of the first compression wave from the impact and the reflection of that wave off the striking surface. The significance of the amplitudes of anything but the first pulse may be questioned. A schematic of the temporal correlation of the various events derived from these pressure traces and other fiducials used in the recording is shown in Figure 61.

3.2.1 Pressure Measurements from Ballistic Testing

The pressure data presented here was recorded using a Kistler piezoelectric transducer. Two pressure ranges were used; a high sensitivity transducer, calibrated to 500 psi and a high range transducer, calibrated to 5,000 psi. Typically, these types of transducers can be over-ranged by

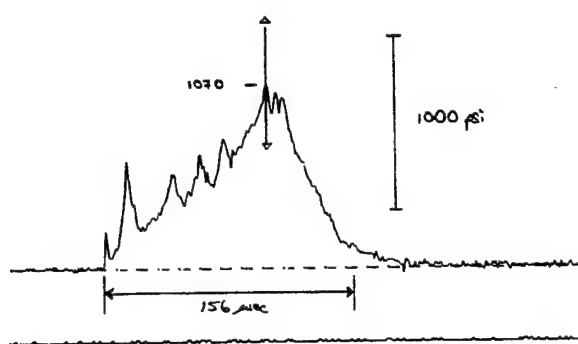


Figure 59. Time resolved pressure pulse from first transducer

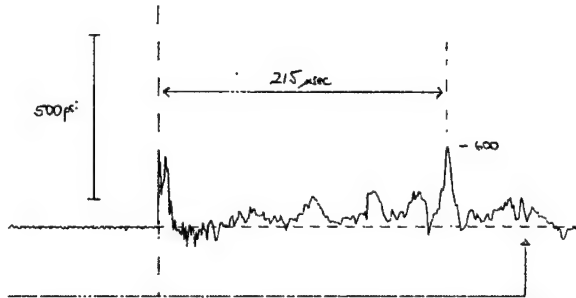


Figure 60. Time resolved pressure pulse from rear surface transducer

factors of 2 and 3. All pressure data presented here was recorded 1/2 inch above the projectile trajectory, unless noted otherwise, with the transducer

installed 2.40 inches downstream of the impact site. The recorded pressure traces are basically similar in shape. They exhibit an initial fast rise to some level, typically less than 1/2 of the later peak value. A drop follows the first peak and then a gradual rise to a second peak that is also the maximum pressure recorded. This second peak is then followed by an expansion to zero. It is this second peak, or the absolute peak value recorded that will be used in the subsequent presentation. It can also be said that the generalized description above, applies both to the 20% and 10% gelatin data.

It should be pointed out here that the absolute accuracy of these pressure measurements is very difficult to quantify. The greatest complication arises from the fact that ordnance gelatin is not a fluid under normal conditions. Assuming that even if a well coupled interface between transducer and gelatin exists at the onset of testing, it is unclear that this interface will remain fully in tact during initial, and, in particular later

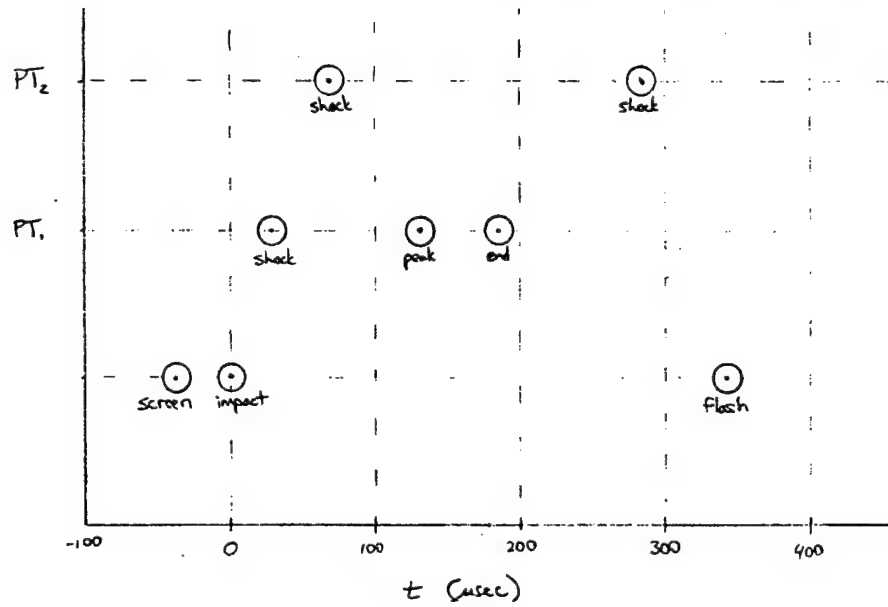


Figure 61. Temporal correlation of pressure histories

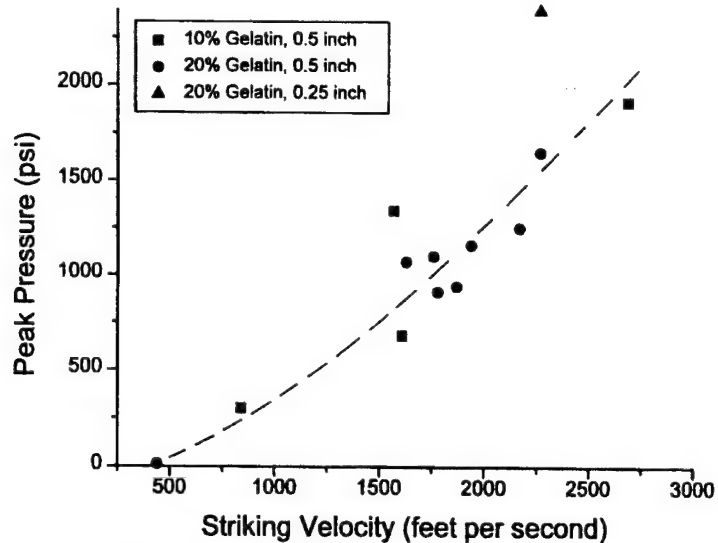


Figure 63. Peak pressure is proportional to striking velocity squared

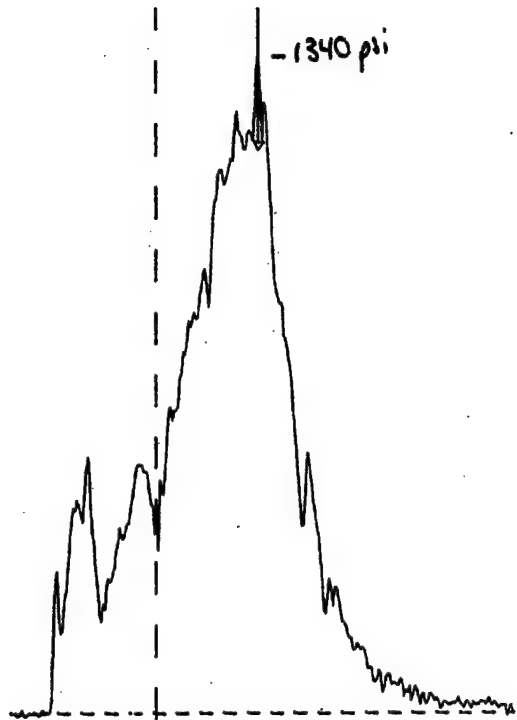


Figure 62. Time resolved pressure for spherical projectile striking 10% gelatin at 1,570 fps

shock passages. We have reasoned that during periods of increasing pressure it should be possible to sustain a well-coupled interface. It is therefore suggested that rising pressures be reasonably well represented. Rarefactions on the other hand are probably not well tracked. A totally confusing picture results when gross motion of the gelatin material, adjacent to the transducer, has initiated. The material now has to flow past or around the obstacle caused by the transducer and that becomes a troublesome event especially for a semi-solid material.

The pressure profiles recorded often exhibit rather sharp spikes. The transducers are capable of responding in the Megahertz regime but the recording/storage medium is limited in its storage capacity. A limited number of data points can be stored at any one time. The resultant temporal resolution of the recorded data is therefore dependent on the recording rate. Our storage oscilloscopes are 10-Megahertz devices however at the recording speeds typical of this data, much lower sampling rates are used because of the limited memory

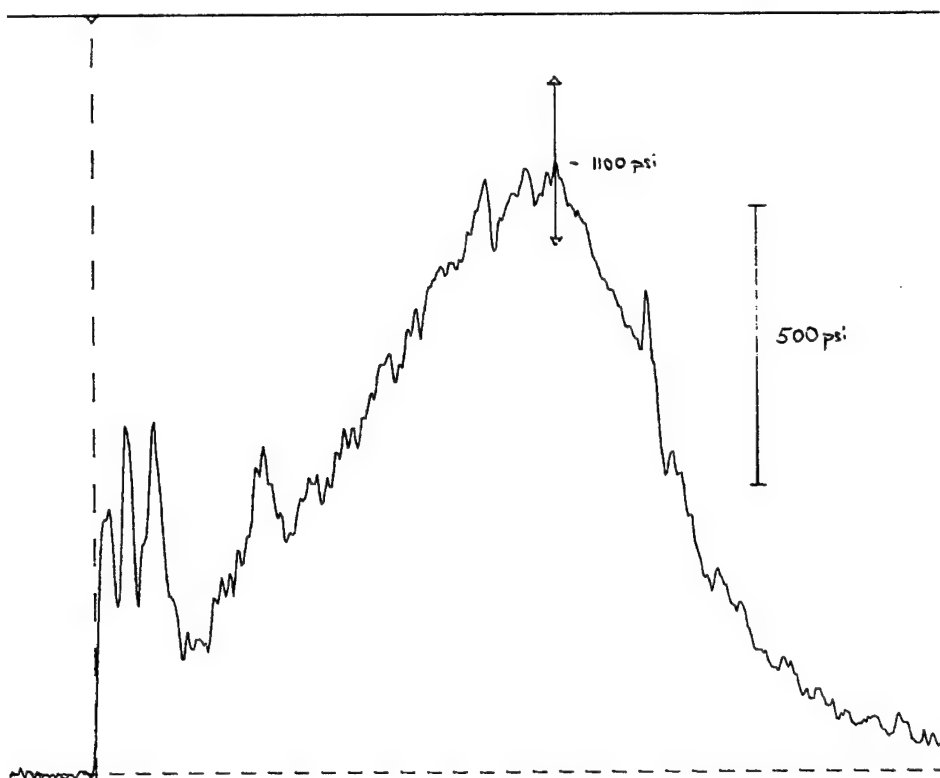


Figure 65. Time resolved pressure for spherical projectile striking 20% gelatin at 1,760 fps

capacity. It must therefore be expected that certain short duration peaks from the transducers will not be accurately replicated in the data as it relates to peak values. For the interpretation of the present data this does not appear to present a significant problem. The pressure peaks used here are typically of rather long duration and profound accuracy is neither claimed nor required.

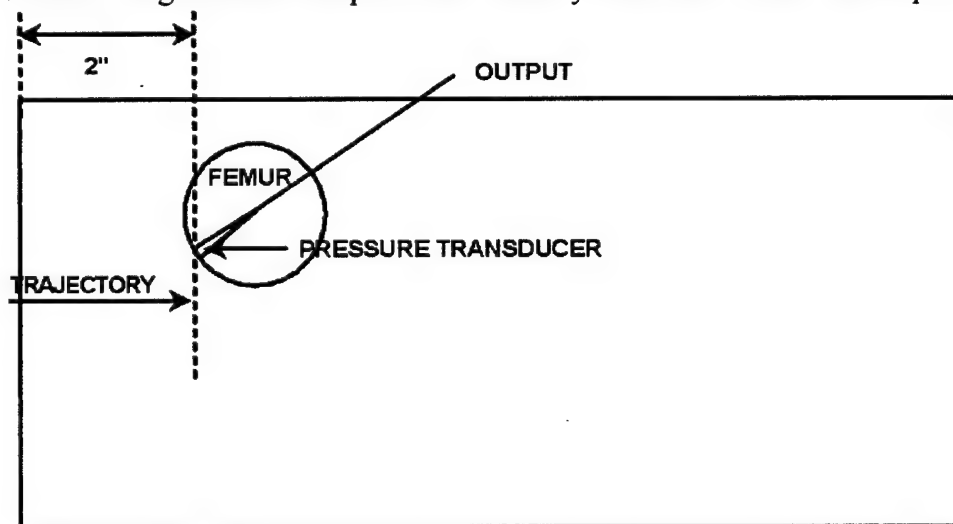


Figure 64. Configuration of Simulated Femur Ballistic Experiments

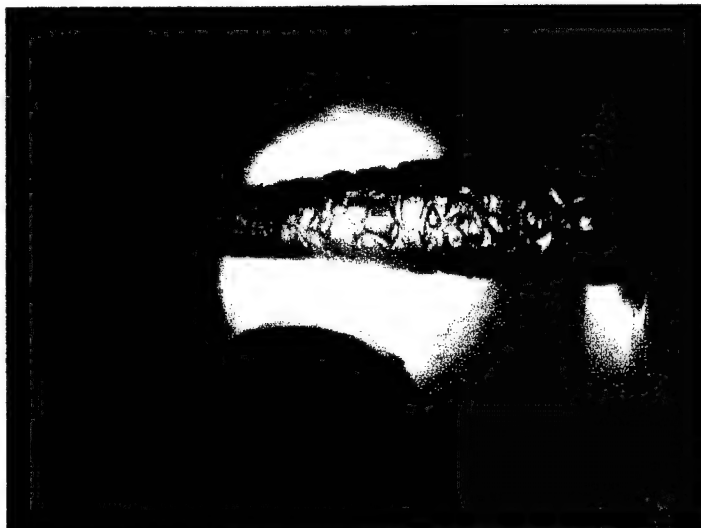


Figure 66. Spherical projectile incident at 1,370 fps,
320 microsec after impact

striking velocities. Peak pressure data recorded for 10% and 20% gelatin appears to coincide. The data scatter in data is large, however no trends can be detected that would distinguish between 10% and 20% data. A series of tests at low striking velocities were also performed but their inclusion in the presentation of Figure 63 is not practical. For striking velocities up to 440 ft/sec. we recorded pressures less than 20 psi in 20% gelatin and that result is indicated.



Figure 67. Spherical projectile incident at 1,750
fps 332 microseconds after impact

data probably no better than an arbitrary linear fit, but it seems more gratifying from a physics stand point for the reason given above and because it will go to zero in a consistent fashion and also seems to lend itself to extrapolation to higher values of velocity.

Peak pressures recorded are plotted as a function of striking velocity in Figure 63. The data identified by circles is for 20% gelatin and triangular symbols represent 10% gelatin data. All pressure data was recorded 1/2 inch removed from the trajectory of the 1/4 inch spherical projectile except for the data point represented by the triangle; this data was recorded closer in, nominally 1/4 inch removed from the trajectory. This point falls well above all other data that we have attributed to the close proximity to the trajectory for this point. If this trend is confirmed, it will be very desirable to systematically vary the distance of the transducer from the trajectory, for constant

Since the recorded peak pressures presented are not the result of the material being shock-loaded, but what seems to be related to the passage of the projectile, i.e., a fluid-mechanical pressure, it seemed reasonable to check for a velocity squared dependence of the peak pressure. In fluid mechanics this would be equivalent to a dynamic pressure, which includes a velocity squared and density term. Data scatter would obscure any possible density differences for 10% and 20% gelatin (specific gravity of 1.02 versus 1.06). This forced a velocity-squared curve through a well-anchored point in the middle of the densest data scatter (no other justification) and calculated the remainder of the parabola. This second order dependence on velocity fits the

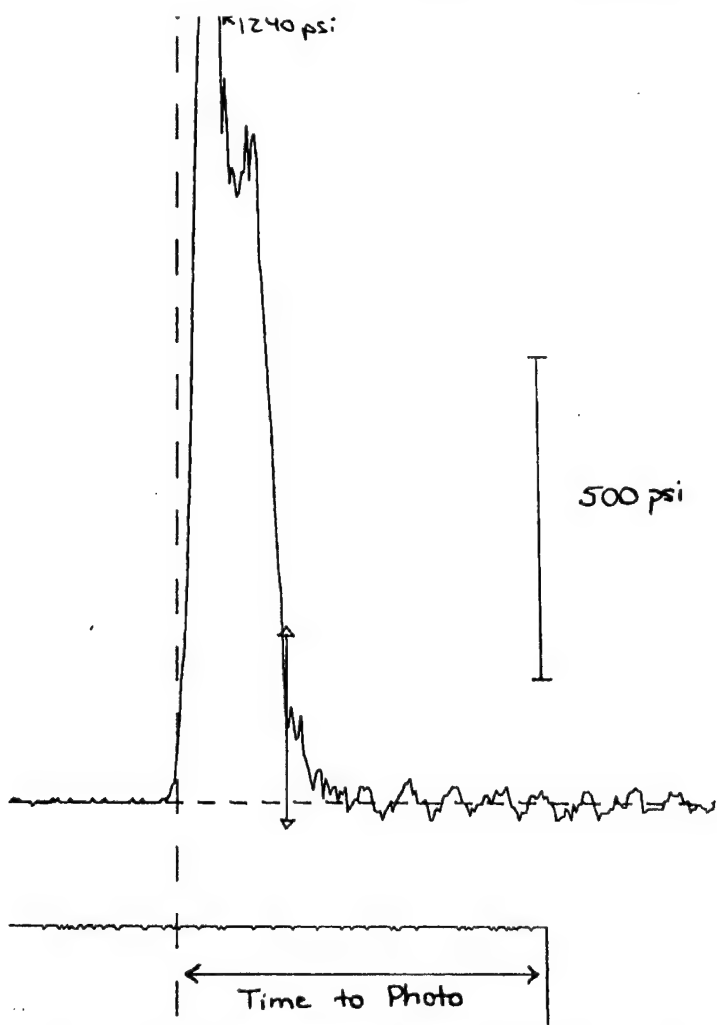


Figure 68. Time Resolved Pressure for Glancing Impact on Instrumented "Femur" at 1750 fps

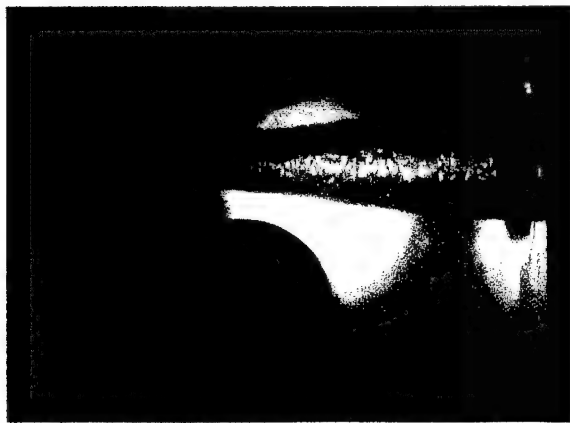


Figure 69. Spherical projectile incident at 2,160 fps 178 microsec after impact

It does not seem desirable to include all recorded pressure traces but a comparison of typical pressure traces is informative. The pressure trace recorded in 10% gelatin, from Run 8-10-03, for a striking velocity of 1,570 ft/sec. is shown in Figure 62. A similar test, at a slightly higher striking velocity of 1,760 ft/sec., is shown in Figure 65 for 20% gelatin from Run 7-31-03. A comparison of the two traces, which is somewhat complicated by the fact that different recording speeds were used, shows that the traces are quite similar in shape and duration, with a marginal match in peak pressure.

3.2.2 Ballistic Test Data For Simulated Femur

A preliminary effort was made to investigate the pressure field experienced by a simulated bone, embedded in the ordnance gelatin. We nominally attempted to approximate femur in size, with the gelatin matrix being representative of soft tissue surrounding the femur. The femur was simulated using a 1.50-inch diameter aluminum cylinder, embedded in gelatin as shown in Figure 64. The cylinder was instrumented with a single, flush mounted, piezoelectric transducer on the curved surface. The axis of the transducer was at 45 degrees to the projectile trajectory in all but one test, where it was parallel.

For the first test on a simulated femur, the trajectory of the projectile was 3/4 inches removed from the femur surface. It yielded the temporary cavity photograph of Figure 66, recorded 320 μ sec. after impact. Unfortunately, the pressure level was not sufficient to trigger the recording medium so that no

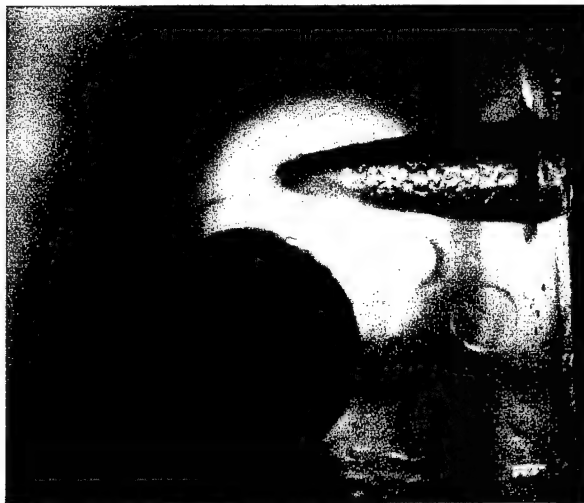


Figure 70. Spherical projectile incident at 2,060 fps

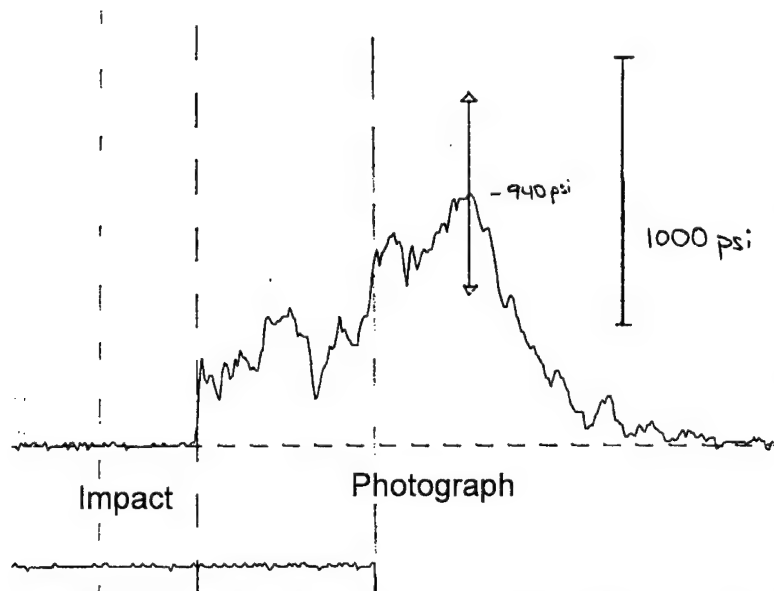


Figure 71. Time Resolved Pressure for 2,160 fps Striking Velocity

would be parallel to the projectile trajectory, i.e., so that the diaphragm would be facing the projectile (perpendicular). The shadowgram of Figure 70 shows a typical temporary cavity and the pressure trace, shown in Figure 72, depicts a rather different response than was seen from the pressure probes tested. A preliminary observation is that the pressure experienced at this location, with an indicated peak of nearly 2,100 psi and a very rapid rise to this peak, followed by an equally sharp drop, is typical of shock loading and reflection. The large femur, compared to the transducer or pressure probes is a much more efficient surface for shock reflection, at this orientation. This may explain the high spike. The second peak, seen on the pressure probes, is not expected to be dominant here because of the much greater distance from the trajectory and the 90-degree rotation of the transducer.

pressure was recorded. The second attempt represented an over-correcting and resulted in a glancing impact on the femur, as seen in Figure 67. The pressure trace recorded for this test is shown in Figure 68 and seems to be revealing a structural shock from the solid impact, superimposed on the pressure trace. The response went off-scale at an indicated pressure level of 1,240 psi.

The test was then repeated two times with only partial success. Figure 69 shows the temporary cavity, recorded 178 μ sec. after impact, for a striking velocity of 2,160 ft/sec. Unfortunately, the pressure trace presented in Figure 71 shows that the transducer went into saturation at an indicated 1,410 psi. The third attempt yielded a good photograph of the temporary cavity, but once again, the transducer failed to trigger the storage scope so that the pressure data was lost.

Since these tests were considered exploratory, we felt justified in changing a basic condition, before we ever had a complete success with the original configuration. For this test we rotated the femur so that the axis of the transducer

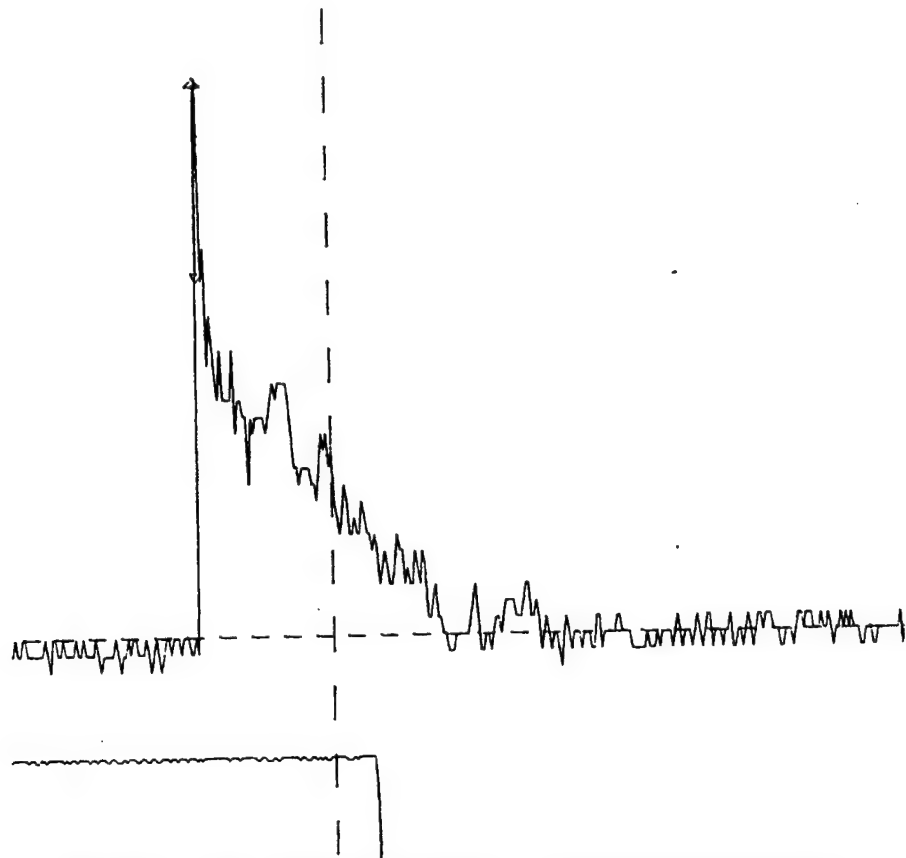


Figure 72. Time Resolved pressure for Ballistic Experiment in Previous Figure.

3.3 BALLISTIC IMPACT OF PROJECTILES WITH VARIOUS GEOMETRIES AND CONSTITUENT MATERIALS

If projectile retardation within ordnance gelatin targets can be viewed as a fluid mechanical event, basically dependent on a drag coefficient, an area, and a dynamic pressure (proportional to density and velocity squared), then the ballistic coefficient, β , which is the weight of the projectile, W , divided by its drag coefficient, C_D , and representative area, A ($\beta = \frac{W}{C_D A}$), should correlate projectiles that differ in mass and geometry. In the case of spherical projectiles, the drag coefficient, C_D , should be constant over a reasonable size range so that the scaling parameter is reduced to W/d , where d is the diameter of the projectile.

This β -scaling approach appeared to be reasonably successful for addressing projectile geometry related issues. However, when current data, produced with 1/4-inch diameter steel spheres was scaled for comparison with 17 caliber BB data, it was found that about a 10% discrepancy was present. The 1/4-inch spheres penetrated 10% deeper. This observation prompted us to carefully reexamine our present data as well as older BB data.

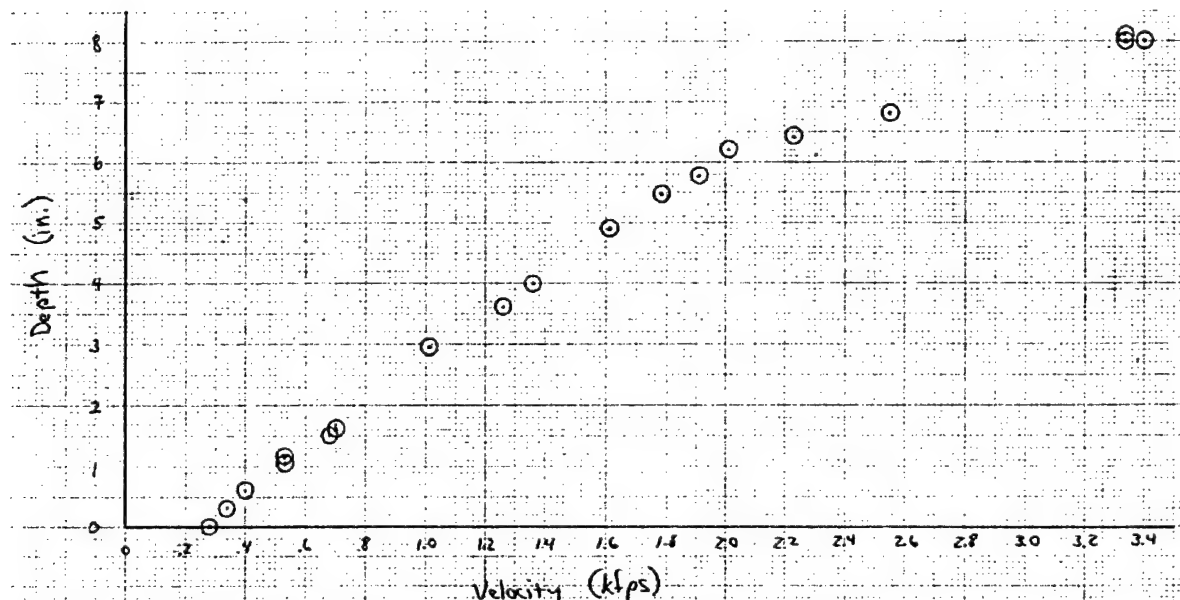


Figure 73. Ballistic Penetration of BBs into 20% Ordnance Gelatin

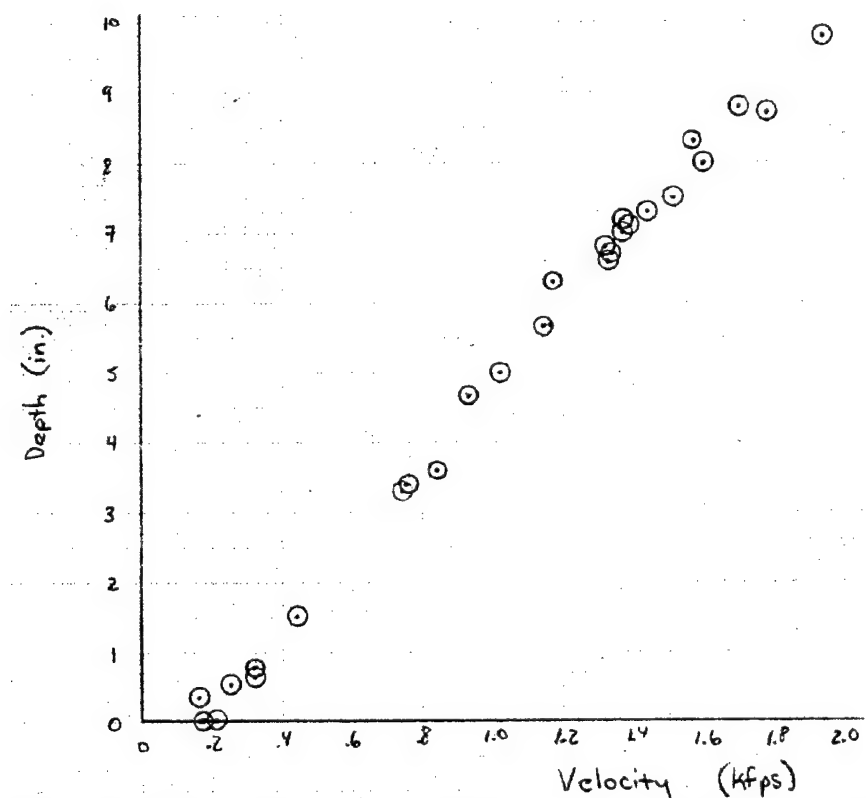


Figure 74. Ballistic Penetration of $\frac{1}{4}$ " spheres into 20% ordnance gelatin

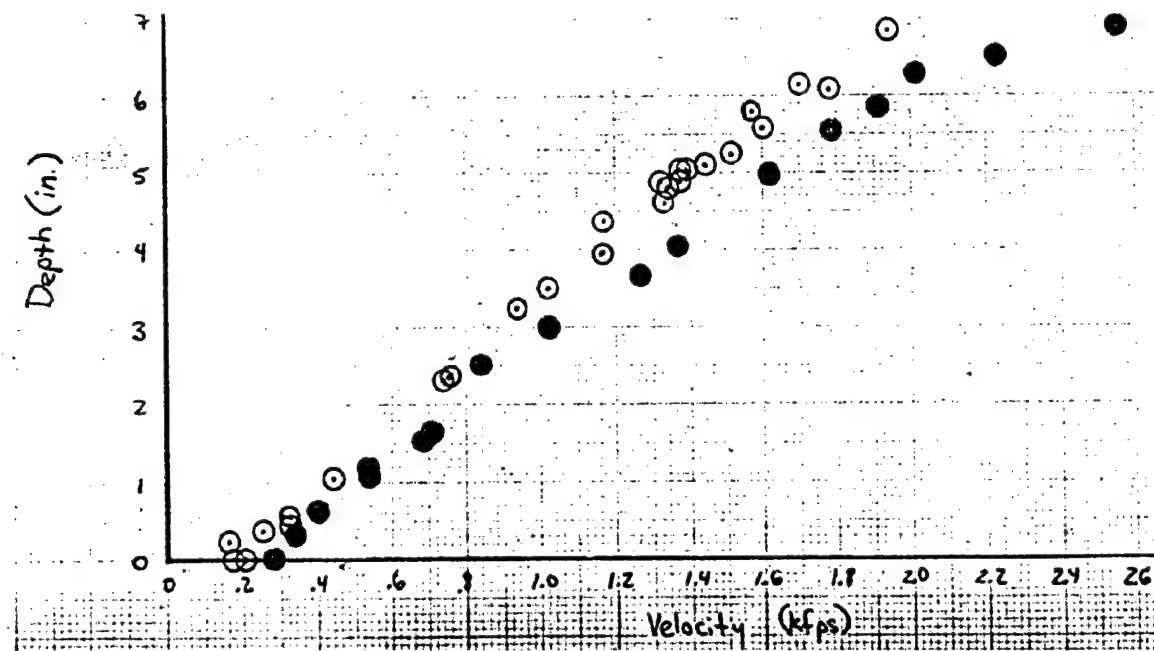


Figure 75. $\frac{1}{4}$ " steel sphere data (open circles) β -scaled to BB (filled circles) ballistic penetration data

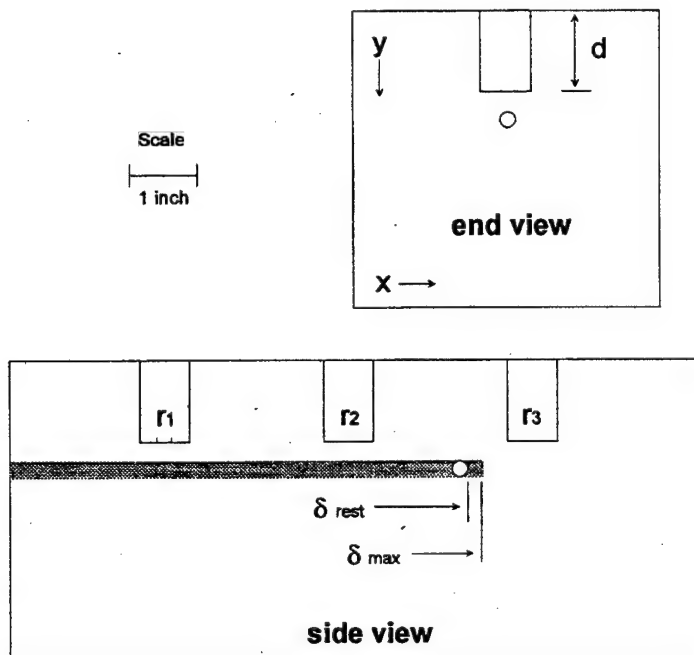


Figure 76. Configuration of In-Situ Experiments and Variance between Maximum Penetration Depth and Final Resting Location

The results of this investigation, shown in Figure 73 through Figure 75, confirmed that no differences could be attributed to differences in preparation. Figure 73 shows the penetration data for BB's into 20% gelatin, all at temperatures between 37 and 44 degrees F. Data from previous tests as well as 14 tests performed under this program are shown. Old and new data are indistinguishable. The penetration depths for 1/4-inch steel spheres, all generated under this program, are shown in Figure 74 and are basically unremarkable. The relatively large data scatter near zero penetration depth is not unexpected.

This data was then scaled by ballistic coefficient to correspond to BB-conditions.

Table 4. Depth of Penetration Data for $\frac{1}{4}$ " Steel Sphere
in 10, 15, and 20% Gelatin

SHOT #	TARGET	V-STRIKING (FPS)	DEPTH (IN.)	V-RESIDUAL (FPS)
12/14/01	20%	1510	7.5	
12/14/02	20%	1600	8.0	
12/14/03	20%	1370	7.0	
3/8/02	20%	1320	6.8 / 7.0	
3/9/01	20%	1390	7.1 / 7.2	
3/13/01	15%	1370	9.4	
3/13/02	15%	1210	8.8	
3/21/01	20%	1440	7.3	
3/21/02	20%	1340	6.7 / 6.9	
5/17/03	15%	1200	8.8	
7/18/01	20%	1370	7.2	
8/7/02	20%	160	0.35	
8/8/01	20%	205	0	
8/8/02	20%	320	0.65	
8/8/03	20%	170	0	
8/8/04	20%	440	1.53	
8/8/05	20%	250	0.54	
8/10/02	10%	1610	4.8	890
8/10/03	10%	1570	4.8	770
8/17/01	20%	1940	9.8 / 9.6	
8/17/02	20%	930	4.7	
8/17/03	20%	320	0.8	
8/17/04	20%	750	3.3	
8/17/05	20%	1150	5.6	
8/21/02	10%	1060	4.8	470
8/21/03	10%	370	4.8	<50
8/21/04	10%	1230	4.8	550
8/21/05	10%	840	4.8	370
8/21/06	10%	2690	4.8	790
8/28/06	20%	1780	8.7	
8/31/01	20%	1020	5.0	
8/31/02	20%	1330	6.6/6.4	
8/31/03	20%	740	3.3	
8/31/05	20%	N/A	9.0	
8/31/06	20%	1700	8.8	
9/6/01	20%	1570	8.3/8.1	
9/6/04	20%	840	3.6	
9/6/05	20%	1170	6.3/6.1	
9/12/02	20%	1520	7.5/7.3	
9/12/03	20%	1550	7.7/7.5	
9/18/01	20%	470	1.6	
9/18/02	20%	1350	6.9/6.7	
9/18/03	20%	1510	7.6/7.3	

This scaled data is superimposed on the penetration data of Figure 73 and presented as Figure 75. The BB-data is presented as solid symbols and falls about 10 per cent below the penetration data for scaled spheres. This discrepancy is real and must be taken to mean that β -scaling is not entirely valid, or that the drag coefficients are not constant. One factor contributing to this

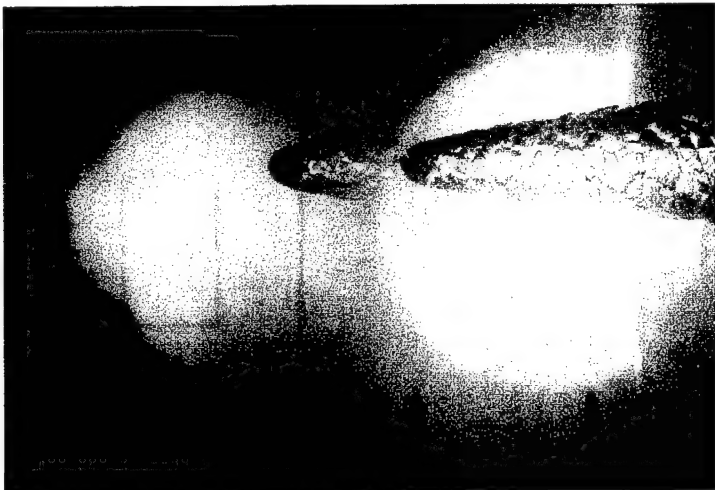


Figure 77. Experiment 9-12-03



Figure 78. Experiment 9-18-02

discrepancy is illustrated in Figure 76 where it was observed that the final resting location of the projectile does not correspond to the maximum depth of penetration. The reason for this is that the target material recoils as the projectile slows down and causes the projectile to rebound. This appears to be about a 3% effect in 20% gelatin penetration depth measurements and substantially less than this in 10 and 15% formulations where penetration depth is greater and material elasticity less.

Impacts on lower concentration gelatin produce far greater penetration depths than impacts in 20% gelatin. A limited number of tests performed on 15% gelatin came to rest within the 10-inch long model for velocities below 1,400 ft/sec. For 10% gelatin the problem was greater. We therefore decided to address the penetration issue by measuring the residual projectile velocity after penetration of a block of gelatin in the transverse direction (4.80 inches). The data from these tests is tabulated in the summary tabulation (Table 4) of all 1/4-inch steel sphere penetration data. Two tests performed using 1/4-inch glass sphere produced data that should not be used here; the high velocity test resulted in a shattered projectile and the low velocity test falls in a region of large data scatter.

3.3.1 In-Situ Velocity of the Penetrating Projectile.

The mathematical model to describe the retardation of the spherical projectile in gelatin has used final penetration depth data, for a given striking velocity, to describe the retardation process. This approach must assume that the instantaneous velocity/penetration depth is given by the final penetration depth versus striking velocity. To test the validity of this approach we recorded double flash photographs of the projectile during the penetration process. The distance between the two photographic images of the projectile, properly scaled, and the known temporal separation of the two flashes yield a mean velocity over the distance between the two images.



Figure 79. Experiment 9-18-03

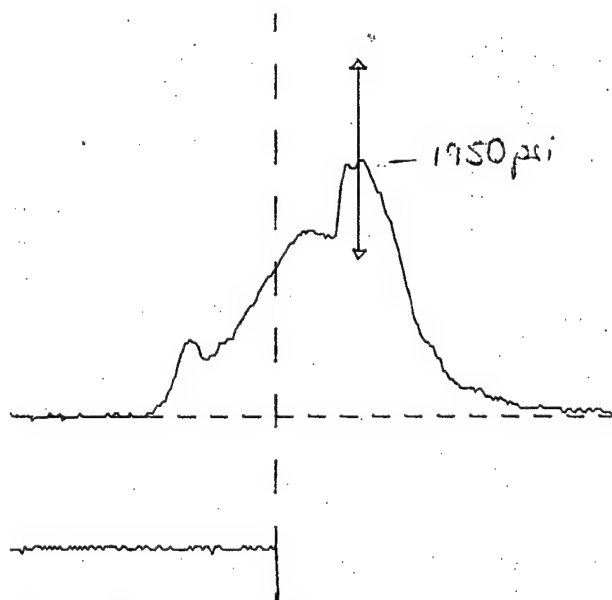


Figure 80. Pressure Pulse from Experiment 8-23-02

The results from three tests that yielded usable images are shown in Figure 78 through Figure 79 and in the summary of runs performed (Table 3 and Table 4), as runs 9-12-3 and 9-18-2 and -3. The instantaneous velocity/penetration data shows that the velocity loss per distance of gelatin penetrated is not constant, as might be deduced from an examination of the final penetration versus velocity plot of Figure 74. At higher velocities the velocity loss per distance penetrated is greater than at low velocities.

3.3.2 Tests Using Conical Projectiles

Testing using conically sharp, cylindrical projectiles was initiated on 20% gelatin, instrumented with high-speed pressure transducers. One of the obvious problems encountered here was the expected pitching/yawing motion of this type of projectile, especially after entering the gelatin block. To alleviate this problem we launched projectiles that were over 4 inches long and placed the muzzle close to the gelatin target so that yawing motion would be minimal during the early phases of penetration. The first test (8-23-01) yawed excessively and curved away from the transducer. Shot 8-23-02 produced the pressure trace of Figure 80 but failed to yield a photograph. Also, the rod nearly impacted the transducer that accounts for the high peak pressure shown. For 8-23-03 the projectile pitched up and struck the transducer mount, as seen in the rather spectacular picture of Figure 82.

It became clear that an even longer projectile, with very little free-flight distance would be required to assure minimal pitch and yaw. Run 9-26-01 produced the pressure trace of Figure 81, but failed to yield a photograph or a striking velocity. A peak pressure of 1,290 psi was recorded.

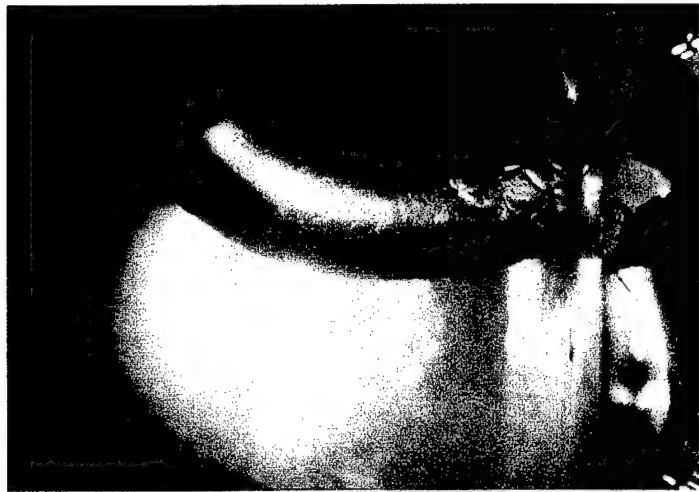


Figure 82. Shadowgram from Experiment 8-23-03

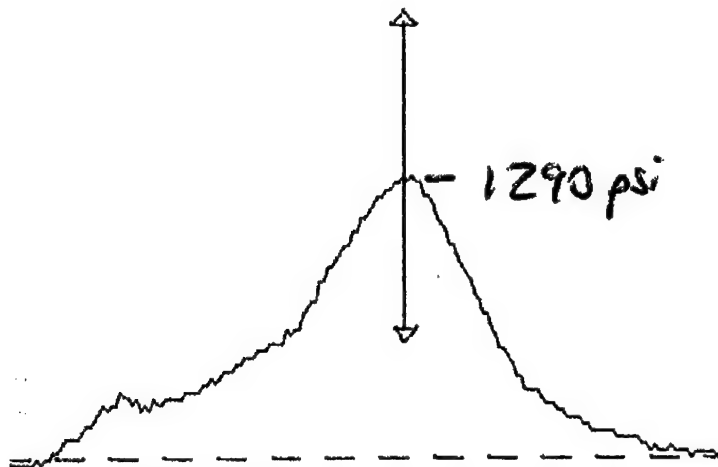


Figure 81. Pressure Pulse from Experiment 9-26-01



Figure 83. Shadowgram from Experiment 10-05-01

pronounced peaks are seen for the blunt spherical projectile than for the sharp cone, which is consistent with wave propagation/expansion considerations.

This test was then repeated as run 10-05-01, using identical gun conditions. This test yielded a velocity of 1,710 ft/sec, and the photograph of Figure 83. The flow field visible about the projectile is typical of a sharp cone in a fluid medium. The temporary cavity evolves more slowly than for spheres which is also consistent with travel through a fluid. The faint image to the left of the projectile is the result of a late time, inadvertent second flash and should be ignored.

The pressure trace recorded for this sharp cone test is shown in Figure 84 and again in Figure 86 after amplification. A peak pressure of 1,010 psi is indicated. The shape of the pressure profile repeats quite well the profile shown in Figure 81 for a similar projectile. Comparison with sphere data shows significant similarity, as expected, if the response is fluid mechanical in nature. The sphere-generated pressure profile of Figure 85 is somewhat difficult to compare to that of the cone, in Figure 84, because of the different recording amplitudes and writing speeds. The amplified cone pressure profile of Figure 86 is better suited for this comparison. Clearly, the peak pressure agrees very well with the peak pressure recorded for a sphere, at nearly identical striking

velocity. The pressure profiles are also similar; pulse durations are nearly identical as are the times to reach the peak value. The primary difference is in the early time pressure peaks that are typical of the arrival of the shock from the impact of the projectile on the gel block. Higher, more

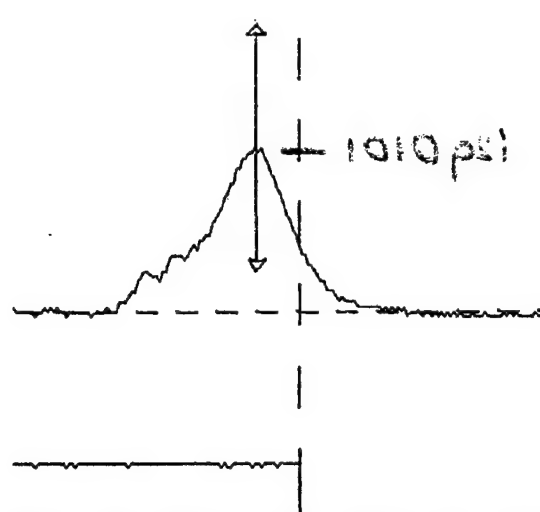


Figure 84. Pressure Pulse from Experiment
10-5-01

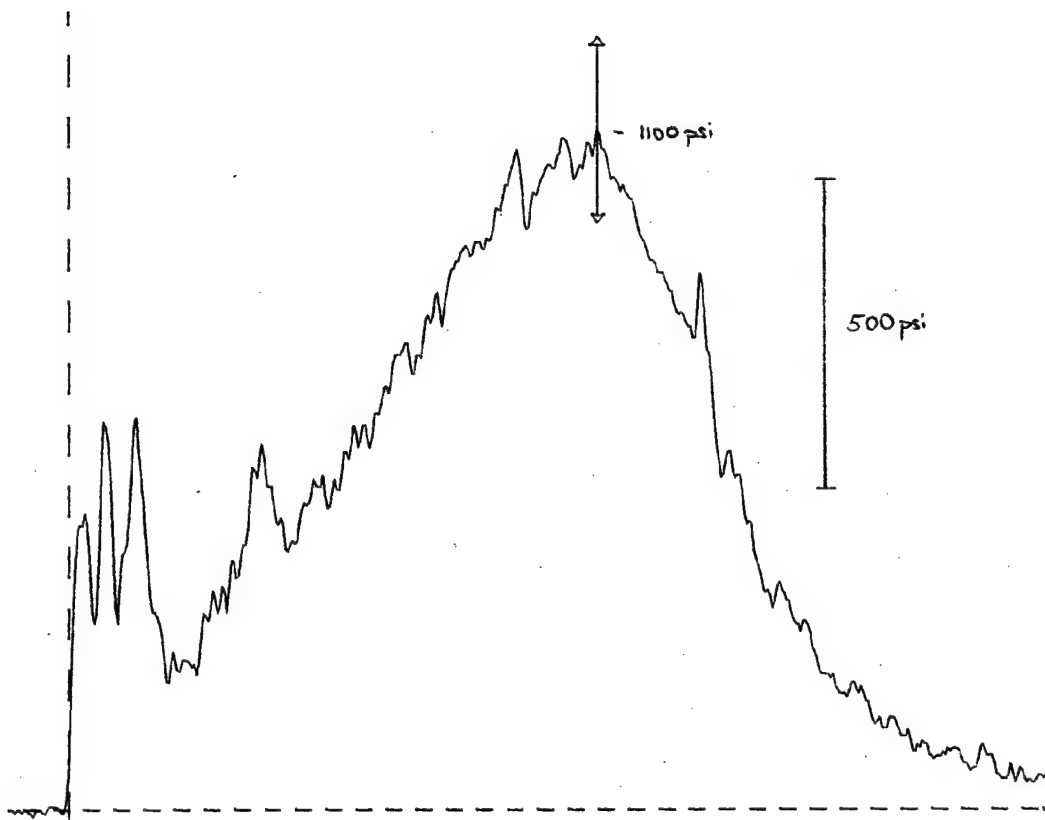


Figure 85. Pressure Pulse from Experiment 7-31-03

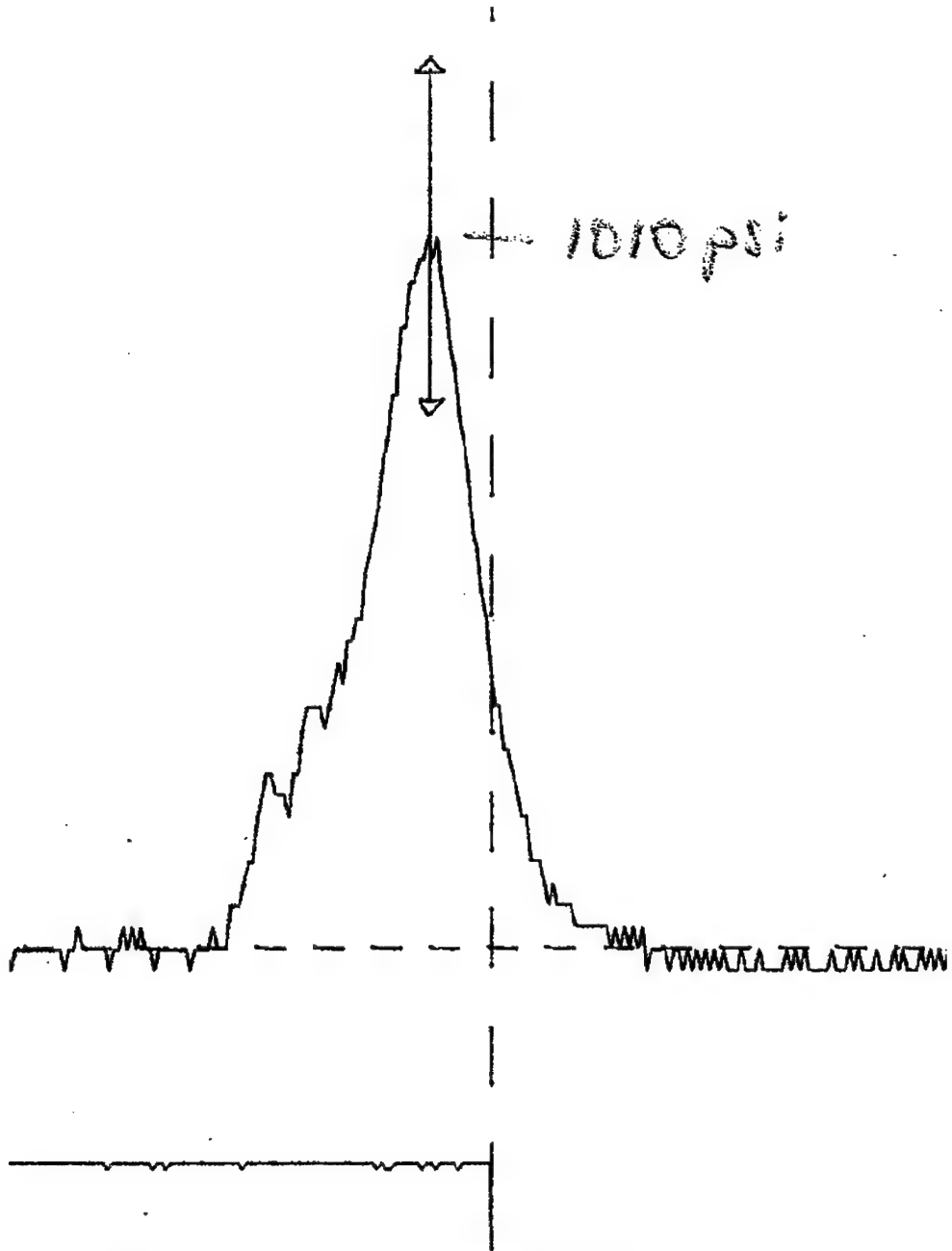


Figure 86. Pressure Pulse from Experiment 10-5-01

4 GRAPHICAL INTERFACE

4.1 SOFTWARE INTERFACE

The injury modeling software is organized into four separate programs, or modules, as shown in Figure 87 below. The programs use a consistent input/output file format so that the output of one module can be loaded as input to the next module. This enabled a script to be used to automate the execution of the four modules.

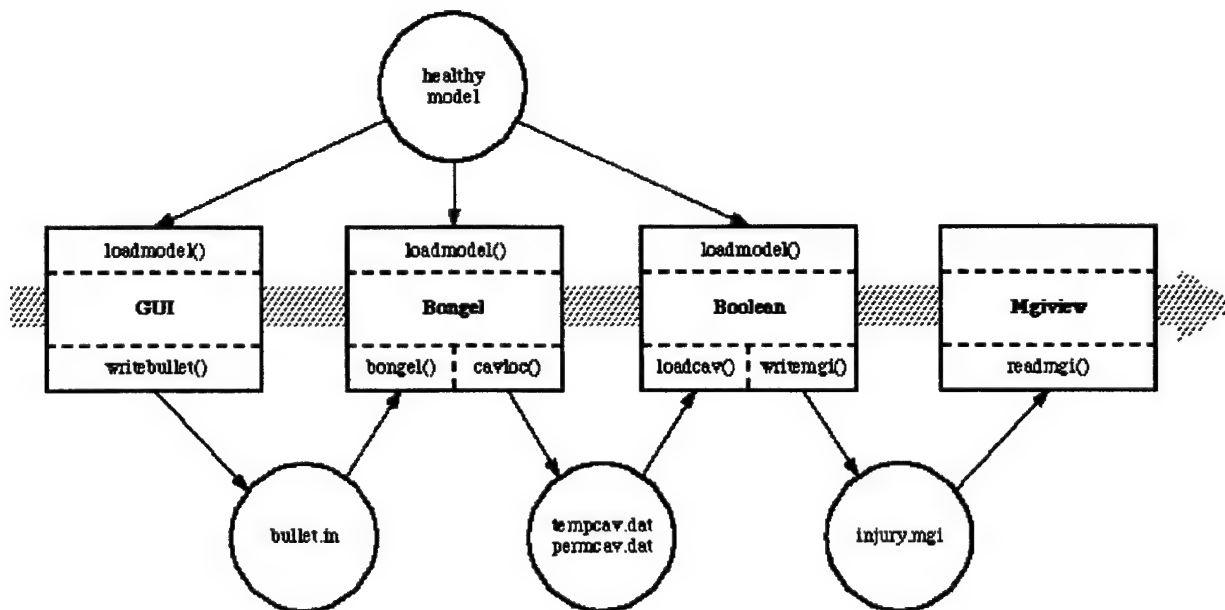


Figure 87. Injury Modeling Software

GUI

This graphical interface, written in C++, lets the user aim a generic weapon at the limbs (upper arm or upper leg). It uses *loadmodel()* to load polygonal descriptions of the tissue surfaces, and uses *writebullet()* to write out the projectile parameters to a file (*bullet.in*) that *bongel* can read. A description of the graphical user interface of this module is contained in the next section.

Bongel

This module contains the three programs (*bongel*, *bulpent*, and *cavloc*) for calculating the shapes of the temporary and permanent wound cavities. It queries the healthy model for material properties of the tissue along the projectile path, and writes out a polygonal description of the surface of each cavity. A complete description of its design and implementation is given below.

Boolean

This Boolean geometry software, written in C, loads descriptions of the temporary and permanent cavities (using *loadcav()*), as well as the healthy anatomy models, and uses a Boolean subtraction algorithm to remove the tissue within the permanent cavity. It also marks the tissue in the temporary cavity as devitalized using a Boolean intersection algorithm. It writes *.mgi* files (MGI Inventor-like format) that can be read by *mgiview* for display purposes.

Mgiview

Mgiview is a graphical display utility that had been previously developed by MusculoGraphics. For this project, it was enhanced to display two windows, one containing the 3D surface models of the temporary and permanent cavities (created by module 2), and one containing the injured limb model (created by module 3). It reads one or more ".mgi" files, which can contain polygons, colors, and textures.

4.2 GRAPHICAL INTERFACE

The graphical user interface is divided into three windows, as shown in Figure 88 below. The large window on the left contains a 3D surface model of a human figure. The model is low-resolution so that it can be manipulated quickly and easily (the high-resolution model is used for the resulting injury calculations). Also, in this window, a virtual rifle, represented by the 3D arrow at the right edge of the window in Figure 88. A dotted line extends from the tip of the arrow to the human figure. A cross-hair target indicates the point of contact with the body (in the picture below the line contacts the middle of the right thigh). The dotted line represents the bullet path preceding impact with the body, and the cross hairs represent the impact location of the bullet on the surface of the body. The user can change the view of this model interactively, but the rifle and body move together during the view manipulations.

To aim the rifle at a different portion of the body, the user moves the body within the window in the lower right corner of the screen. This window displays a view from the rifle barrel and down the bullet path towards the body. The cross hairs remain in the center of the window, and the user can translate the body in 3 dimensions to change the impact point of the bullet. As the body is moved, the coordinates of the gun direction, impact location, and list of tissues in the line of fire are updated in the upper right of the screen. If the user wants to model an injury involving bullet-bone contact, he can move the body until the label *bone* appears in the tissue list. The information window in the upper right also contains two interface elements that allows the user to change the properties of the bullet. The user can choose from one of four bullet types (AK47, AK74, M16, hollow point – currently only the AK47 is implemented), and the user can set the speed of the bullet at the time of impact with the body (from 200 - 2000 feet/sec). When satisfied with the bullet properties and direction, the user can press the *shoot* button to write the parameters to a file and then run a script that will execute the other three modules of the program. After the three modules are finished, two windows will be displayed on the screen, one containing the 3D surface models of the temporary and permanent cavities, and one containing a 3D model of the injured limb.

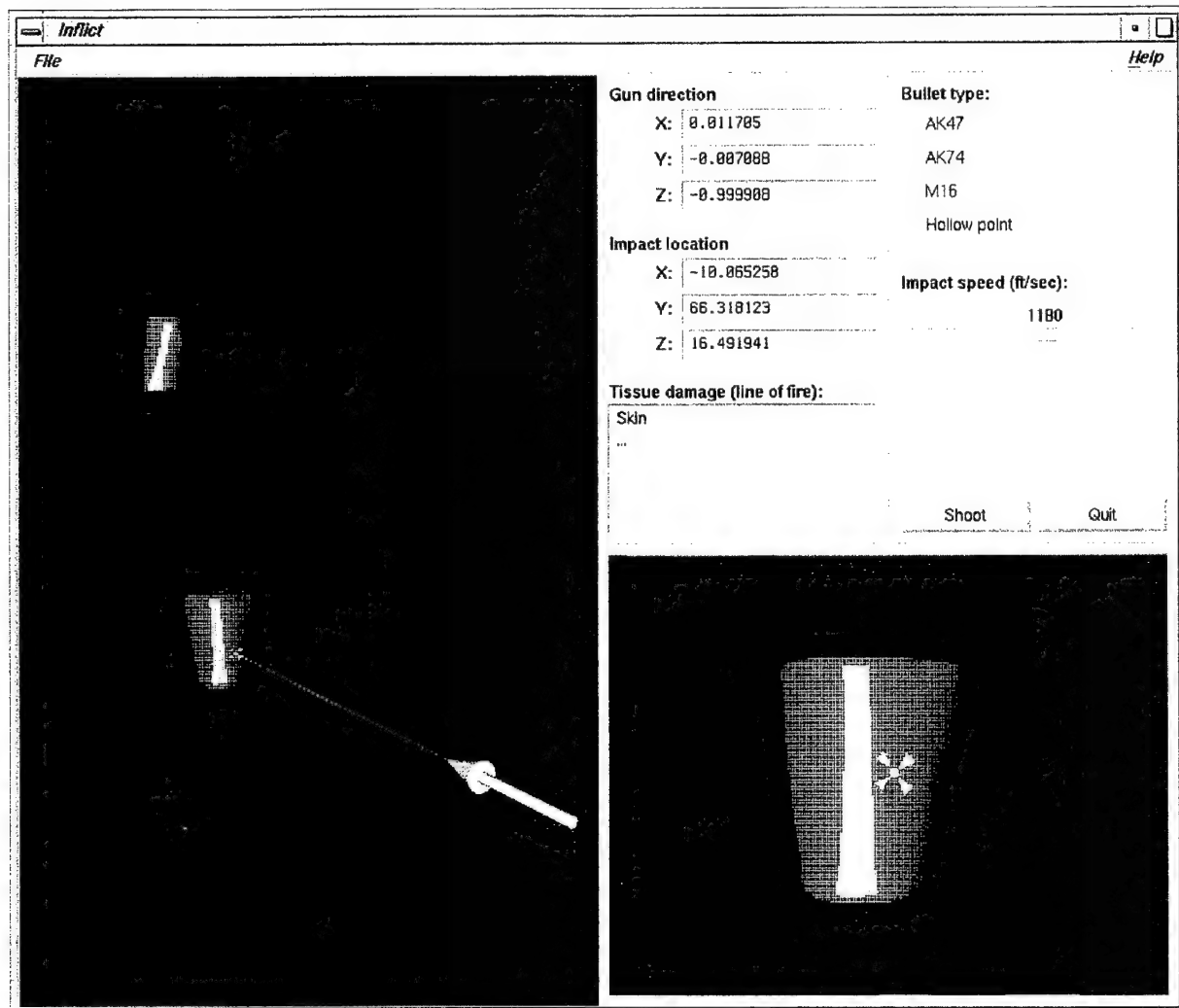


Figure 88. User Interface for the INFILCT module of Injury code

4.3 BOOLEAN CODE FOR INJURY CREATION

As described above, module 3 is Boolean software that uses the injury cavities and healthy limb model to create an injured limb model. In the first step, The volume of tissue from the healthy model that lies within the permanent cavity is removed (subtracted) from the model (call the result, *model M*). The second step is to determine the region of tissue in *model M* that lies within the temporary cavity, and to label it as devitalized. This is done with a Boolean intersection algorithm. Devitalized tissue is usually darker and stiffer than live tissue, so its color and texture are changed to reflect these changes. The third step is to subtract the temporary cavity from

model M , and then add the devitalized tissue model to it. Boolean addition is not needed for this step because there is no overlap between the two model portions. The result is an injured limb model containing a wound cavity surrounded by devitalized tissue. The equations defining this Boolean process are shown below:

H_i = one tissue (e.g., skin, femur) from healthy limb model containing n tissues

$$H = \text{healthy limb model} = \sum_{0 < i < n} H_i$$

P = permanent wound cavity

T = temporary wound cavity

$$M_i = H_i - P$$

$$\text{injured limb model} = \sum_{0 < i < n} (M_i - T) + (M_i \cap T)$$

To perform these operations, we implemented Boolean subtraction and intersection algorithms. The algorithms operate on two closed polyhedra ($P1$ and $P2$) of arbitrary shape. The polyhedra can contain any number of vertices and planar polygons, and can be convex or concave. Both algorithms begin by calculating the intersections of each polygon in the first polyhedron ($P1$) with the polygons in the second polyhedron ($P2$). In the general case, a polygon either lies completely inside the other polyhedron, completely outside the other polyhedron, or it intersects it and is divided into two or more pieces. For Boolean subtraction, the set of polygons representing $P1 - P2$ are collected and formed into a polyhedron. For intersection, the polygons representing $P1 \cap P2$ are collected in a similar fashion.

Much of the design and implementation of these algorithms was performed by MGI for another project, but several enhancements were necessary in order to use the code in this project. Specifically, the numerical robustness of the geometric intersection code was increased so that it would work on models with vertex coordinates much less than one (the models are in units of meters) without losing accuracy. Also, the error checking and error recovery routines were improved so that the code better recognized ill-formed polyhedra, attempted to correct the defects, and printed informative error messages when it was unable to recover. Finally, several bugs were fixed so that once a polyhedron was loaded, several Boolean operations could be performed on it in sequence without having to write it to a temporary data file and then reload it between operations.

4.4 CODE TO ASSEMBLE INJURED LIMB MODEL WITH TEXTURE MAPS

Much of the work for this task had to be skipped for budgetary as well as scientific reasons. With a reduced scope, we did not create complete 3D models of each tissue (skin, muscle, fat, fascia, and bone) in both limb models, nor were realistic texture maps created for each tissue type for healthy and devitalized conditions. As a result, the limb models were simplified to contain just

models of the soft tissue and bone. All of the material between skin and bone was assumed to consist of a generic soft tissue. We believe that although this simplification is a large one, it does not prevent the software from producing realistic injury models in some cases. Much of the tissue in the upper arm and upper leg is muscle, whose retardation coefficients are similar to those of generic soft tissue model employed.

4.5 MODEL QUERY CODE

The primary interface between the *bongel* code in module 2 and the healthy limb model is the *material_at()* function. This function, written in C++, is used by the *bongel* code to determine the material properties of the tissue at the tip of the bullet as it travels through the limb. The prototype for this function is:

```
int material_at(double modelpt[], double tissue_coeff[], char *tissue_type);
```

This function takes as input the X, Y, Z coordinates of the point at which you want to know the material properties (modelpt[]), and returns as output the retardation coefficients of the material (tissue_coeff[]) and the type of tissue (tissue_type) at the given point. *Material_at()* keeps track of the previous point queried, and when it is called again, it forms a line segment from the previous point to the current point. It then checks to see if this line segment crosses any tissue boundaries. If it does not, then the current point is in the same tissue that it was in last time. If the line does cross one or more boundaries, the sequence of boundary crossings is used to determine the current tissue. The retardation coefficients and type of this tissue are then returned to the *bongel* code.

4.6 MATERIAL PARAMETERS

The material properties that MRC calculated from the gelatin experiments were the same as the properties that *bongel* needs to calculate the wound cavities. Thus we did not have to do any further processing of the values. We inserted them into the healthy model file, assigning them to the skin and muscle tissues. When *bongel* queries the model for the current tissue and its material properties, these values are returned without modification.

4.7 CURVATURES AND SURFACE NORMALS

The normal vector at each point on the surface of the skin and the bone is needed in order to calculate the bullet trajectory through the limb. The healthy model file contains normal vectors for each polygon in each 3D-tissue model. These normals were calculated using a polyhedron processing utility that had been developed at MusculoGraphics. Surface curvature values are not currently used in the injury modeling software.

Module 1 uses the surface normal at the point of impact between the bullet and the skin to calculate several parameters that are written to BULLET.IN, and subsequently used by module 2. The code that calculates the intersection between the line of fire and the skin model returns the

impact point as well as the polygon in which the impact occurred. The normal vector for this polygon can then be looked up from the list stored in the healthy model file. This normal vector, the line of fire, and a vector in the plane of the impacted polygon are used to calculate THD and PHD, which describe the angles between the reference frame of the bullet and the reference frame of the skin and bone model.

4.8 GRAPHICAL DISPLAY OF INJURED LIMB

The work for this task centered on mgiview, a graphical display utility that had been previously developed by MusculoGraphics. For this project, it was enhanced to display two windows, one containing the 3D surface models of the temporary and permanent cavities (created by module 2), and one containing the injured limb model (created by module 3). It reads one or more ".mgi" files, which can contain polygons, colors, and textures. Due to funding limitations, the tissue models and texture maps that are displayed, while accurately representing the injury shape, do not present a realistic image of a penetrating injury.

4.9 INTEGRATION OF HEALTHY LIMB MODELS INTO BOOLEAN CODE

3D geometric models of the skin and bone of the upper arm and leg were obtained from the Visible Human male. These models were processed with a commercially available polygon editor to make sure that they had no holes or seams, and that the polygons were all triangles with counter-clockwise vertex ordering and outward-facing normals. They were then put into an Inventor-like format so that they could be loaded into each of the first three modules of the injury modeling software. Shown below is an abridged version of the model file:

```
#Inventor V2.1 ascii
Separator {
    Separator {
        Label {
            label "Body"
        }
        DEF Tissue Separator {
            DEF Bone Group {
                Label {
                    label "Humerus"
                }
                MaterialProperties {
                    coefficients [ 0.00329 0.0 5660000.0 ]
                }
                Material {
                    ambientColor 1 1 1
                    diffuseColor 1 1 1
                }
                Separator {
                    Coordinate3 {
                        point [ -0.08689 0.14564 0.09006, ... -0.18034 0.11287
0.95479 ]
                    }
                    ShapeHints {
```

```
        vertexOrdering COUNTERCLOCKWISE
    }
    Normal {
        vector [ 0.337718 -0.821392 -0.459632, ... 0.255227 -
0.962267 -0.0943473 ]
    }
    NormalBinding {
        value PER_VERTEX_INDEXED
    }
    IndexedFaceSet {
        coordIndex [ 0, 1, 2, -1, ... 31, 30, 25, -1 ]
        normalIndex [ 0, 1, 2, -1, ... 62, 52, 51, -1 ]
    }
}
}
DEF Tissue Separator {
    DEF Muscle Group {
        Label {
            label "Upper Arm"
        }
        MaterialProperties {
            coefficients [ 0.284 -11300.0 148000000.0 ]
        }
        Material {
            ambientColor 1 0.5 0.5
            diffuseColor 1 0.5 0.5
        }
        Separator {
            Coordinate3 {
                point [ 0.17224 0.11403 0.13076, ... 0.13139 0.14543
0.14347 ]
            }
            ShapeHints {
                vertexOrdering COUNTERCLOCKWISE
            }
            Normal {
                vector [ -0.660695 0.739354 -0.129756, ... -0.456261
0.838466 -0.297993 ]
            }
            NormalBinding {
                value PER_VERTEX_INDEXED
            }
            IndexedFaceSet {
                coordIndex [ 0, 1, 2, -1, ... 35, 34, 29, -1 ]
                normalIndex [ 0, 1, 2, -1, ... 65, 55, 54, -1 ]
            }
        }
    }
}
DEF Tissue Separator {
    DEF Bone Group {
        Label {
            label "Femur"
        }
        MaterialProperties {
            coefficients [ 0.00329 0.0 5660000.0 ]
        }
    }
}
```

```
        }
        Material {
            ambientColor 1 1 1
            diffuseColor 1 1 1
        }
        Separator {
            Coordinate3 {
                point [ -0.17939 -0.59382 0.00347, ... -0.16927 -0.63917
0.01092 ]
            }
            ShapeHints {
                vertexOrdering COUNTERCLOCKWISE
            }
            Normal {
                vector [ 0.337718 -0.821392 -0.459632, ... 0.255227 -
0.962267 -0.0943473 ]
            }
            NormalBinding {
                value PER_VERTEX_INDEXED
            }
            IndexedFaceSet {
                coordIndex [ 0, 1, 2, -1, ... 31, 30, 25, -1 ]
                normalIndex [ 0, 1, 2, -1, ... 62, 52, 51, -1 ]
            }
        }
    }
}
DEF Tissue Separator {
    DEF Muscle Group {
        Label {
            label ."Thigh"
        }
        MaterialProperties {
            coefficients [ 0.284 -11300.0 148000000.0 ]
        }
        Material {
            ambientColor 1 0.5 0.5
            diffuseColor 1 0.5 0.5
        }
        Separator {
            Coordinate3 {
                point [ -0.17472 -0.58372 0.00852, ... -0.16927 -0.60936
0.01638 ]
            }
            ShapeHints {
                vertexOrdering COUNTERCLOCKWISE
            }
            Normal {
                vector [ -0.660695 0.739354 -0.129756, ... -0.456261
0.838466 -0.297993 ]
            }
            NormalBinding {
                value PER_VERTEX_INDEXED
            }
            IndexedFaceSet {
                coordIndex [ 0, 1, 2, -1, ... 35, 34, 29, -1 ]
                normalIndex [ 0, 1, 2, -1, ... 65, 55, 54, -1 ]
            }
        }
    }
}
```

4.10 PORT MRC CODE TO SGI AND INTEGRATE INTO MGI CODE

The injury modeling code developed by MRC works as three separate programs (*bongel*, *bulpent*, and *cavloc*). The Fortran source code for each of these programs was ported to the MGI SGI workstation (Indigo2 Max Impact running IRIX 6.2). The port required minimal changes to the source code and it was a straightforward process to compile and run the programs on the SGI.

The next step was to make changes to the code so that it worked in conjunction with modules 1 and 3 as outlined in the software design. The interactive, command-line interface that prompted the user for bullet characteristics was removed and instead all of the necessary input variables were defined in a single data file (which is generated by module 1). The assumptions in *bulpent* were then addressed, i.e., that the limb model is a right, circular cylinder of soft tissue with a

right, circular cylinder of bone in the middle of it. Instead of making these assumptions, the code was changed to load a user-defined 3D-limb model, and query it for tissue shapes and material properties. This query code is also used to determine whether or not the bullet hits the bone. A description of this query code is included above.

The final change that was made was to alter the format of the injury cavity files that are output by *cavloc* and loaded into module 3, the Boolean software. *Cavloc* was enhanced to create closed polyhedra containing counter-clockwise triangles for both the permanent and temporary cavities. These files could then be loaded directly into the Boolean software without further processing.

The injury depicted in Figure 89 and Figure 90 was generated using a bullet with cross-sectional radius of 0.254cm and an impact velocity of 2000 m/s. The bullet was aimed such that it did not impact the femur. It had enough speed to exit the thigh; hence there is an exit wound as well as entrance wound.

The wire-frame picture (Figure 89) shows the permanent and temporary cavities clipped to the surface of the thigh. The wider section of the temporary cavity is at the entrance wound. Because the bullet did not have time to tumble within the soft tissue of the thigh, the permanent cavity remains small. Figure 90 shows the thigh with tissue within the permanent cavity removed, and tissue within the temporary cavity colored darker than the rest. The view is of the entrance wound.

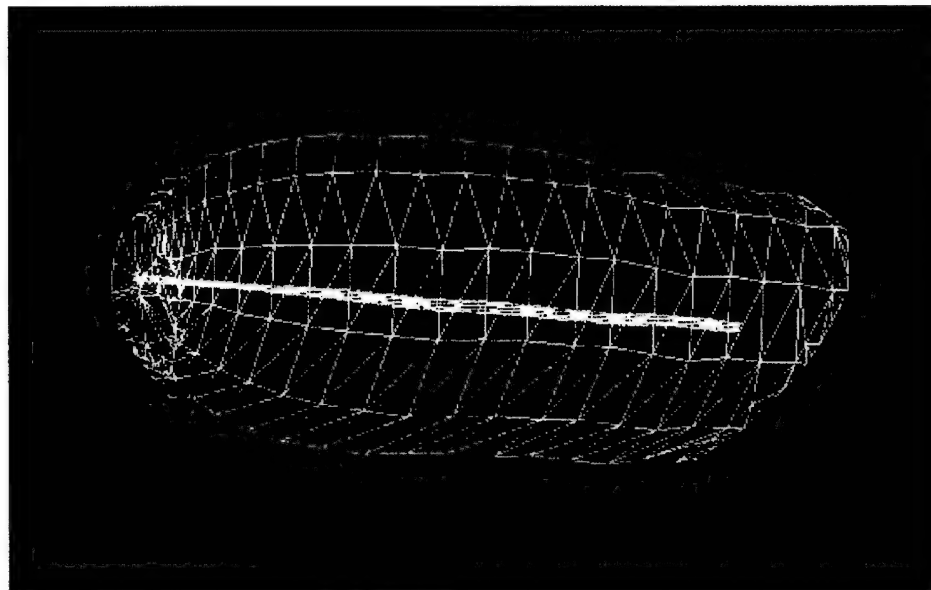


Figure 89. Wireframe model of predicted temporary and permanent cavities

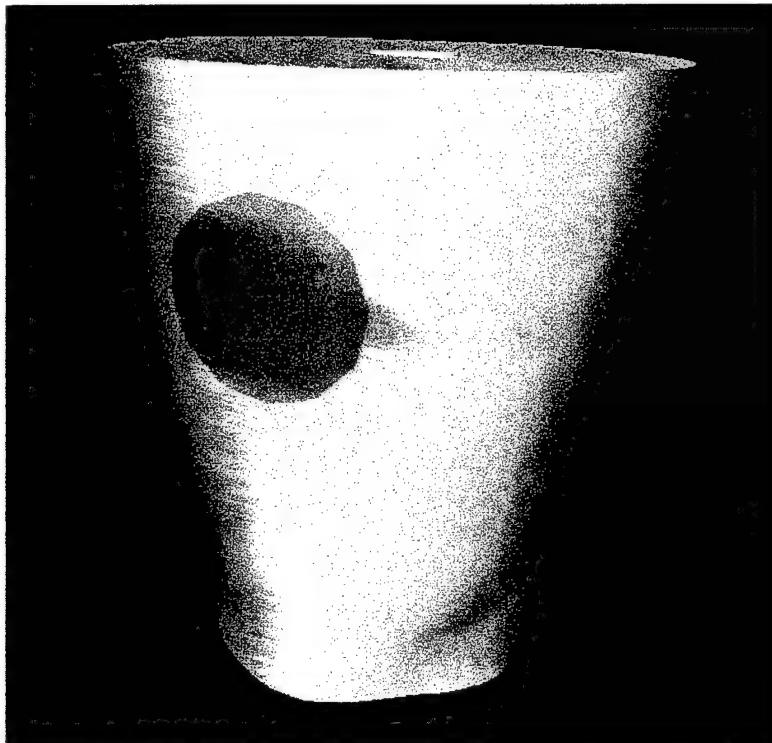


Figure 90. Analytically simulated entrance wound on thigh

5 CONCLUSIONS AND RECOMMENDATIONS

This effort used different configurations of ordnance gelatin as surrogate materials to develop an analytical and experimental methodology that describes mechanical damage to human tissue from penetrating wounds. The assumptions employed were specific to the lower extremities and battlefield threats but could be relaxed to generalize the methodology to other body regions, other threats, and other types of wounds. A software package based on this methodology was developed to predict wound geometries. This software was interfaced with a virtual anatomy based on the Visible Human database to describe tissue damage relative to the anatomy of the lower extremities. The software predicts the extent of soft tissue damage as well as bone interaction, including fracture mode and ejected bone fragments.

Recommendations for future work are sixfold and do not encompass major technical obstacles. First, the existing soft tissue-bone interaction models should be enhanced to include the effect of tissue tearing from the presence of ejected bone fragments in the projectile wake. The importance of this effect is significant. See for example the discussion of the casualty described in Figures 1 and 2 of Appendix A.

Second, the analytical models developed to describe wound geometry in soft tissue are sufficiently detailed that they could be easily extended to characterize the nature of the soft tissue damage adjacent to the wound tract. For example, since the models describe the stress/strain field promoted by the projectile interaction with soft tissue, the predicted stresses and strains could be used to describe the radius over which blood vessels of different diameters rupture, the extent of tissue concussion, etc.

Third, the mechanical property database for the constituent tissues could be more highly resolved in terms of number of tissue categories considered. The various models developed, in most cases, are functions of independently measured target properties where the data is already available but merely has to be reduced properly. In particular, it would be desirable to have a model specific to skin.

Fourth, in order to make the wound visualization more compelling, improved texture maps of damaged tissue and bleeding need to be developed. The bleeding should not only consider free-flowing blood but also blood that is not free-flowing and has altered the appearance and mechanical properties of other tissue.

Fifth, bone trauma from penetrating wounds is a major source of battlefield morbidity and long hospital stays, yet very little is known about the mechanics of projectile bone interaction. Presumably, just as the pathogenesis of any disease is studied to develop remedial treatment, the same logic would be applicable to bone trauma. An effort in this area would presumably include ballistic experiments on pre-loaded human bones in various gelatin matrices with in-situ instrumentation.

Finally, there is a need to more extensively validate the models that have been developed, in particular, by comparison with human autopsy data. -

Simulation and Modeling of Penetrating Wounds from Small Arms

R.D. Eisler and A.K. Chatterjee
Mission Research Corporation
Fountain Valley, California

G.H. Burghart
G.B. Laboratory, Inc.
Fountain Valley, California

This paper is being published in *Health Care in the Information Age: Future Tools for Transforming Medicine* and being presented at the *Medicine Meets Virtual Reality 4 International Symposium* sponsored by The University of California School of Medicine, the Advanced Research Projects Agency, American Psychiatric Association, Institute for Telemedicine, Society for Minimally Invasive Surgery, Society of Gastrointestinal Endoscopic Surgeons, and Society of Cardiovascular and Interventional Radiology, San Diego, California, 17 – 20 January 1996.

1. BACKGROUND

The overwhelming source of morbidity on the battlefield is penetrating injuries to the musculoskeletal system. Wounds to lower extremities, in particular, account for the majority of total and nonfatal military casualties in both conventional European-style campaigns and jungle warfare. Physical characteristics of these wounds, however, are highly variable and thwart assessment in terms of their medical consequences and operational effects on soldier performance. This is illustrated by the two combat casualties shown in Figures 1 and 2.

Both casualties were struck in the forearm by bullets fired from an AK47 assault rifle at ranges of about 20 meters. For both casualties the bullets were probably of identical design and construction and had the same striking velocity and kinetic energy. The casualty shown in Figure 1 however sustained a relatively superficial soft tissue wound while the casualty shown in Figure 2 almost sustained a traumatic amputation of the arm.

This subject effort is providing an integrated software package, applicable to the extremities, that: (1) Simulates tissue damage from small arm projectiles and fragments

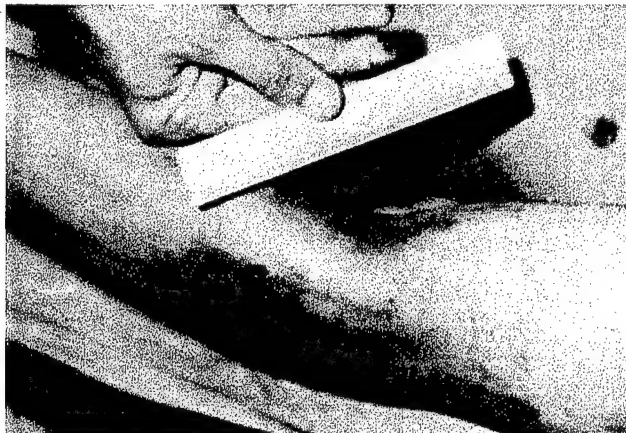


Figure 1. Casualty with perforating gunshot wound of the forearm, Fig. 4-52, Ref. 1.



Fig. 2a. Casualty with perforating gunshot wound of the forearm, Fig. 4-53, Ref. 1.

penetrating the musculoskeletal system; (2) Performs a detailed biomechanical assessment of residual physical capability; and, (3) Provides a high resolution graphical interface for medical simulation and training.

The program started in September 1994 and has a 36 month period of performance and consists of five tasks. The first task develops models describing soft tissue damage from a penetrating wound. This description includes the permanent wound cavity, tissue transient response, and hemorrhagic zone of extravasation. Models developed in the second task describe interaction of bone tissue with the missile including mode of fracture produced.



Figure 2b. Exit wound for Casualty shown in Figure 2a, Fig. 4-54, Ref. 1.

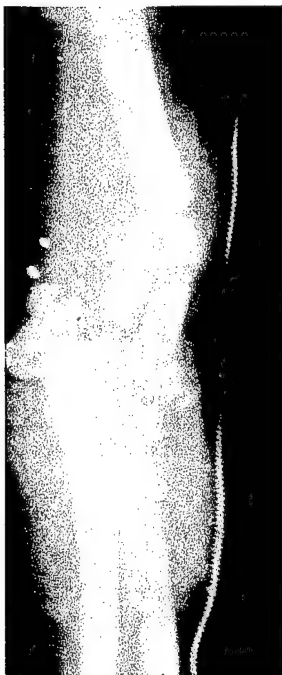


Figure 2c. Roentgenogram of casualty shown in Figure 2 shattered elbow, Fig. 4-55, Ref. 1.

Task 3 consists of three subtasks. The first subtask develops models to describe coupling between the ballistic response of the bone and the surrounding soft tissue. This coupling occurs due to ejection of secondary bone fragments (Figure 2c), fragmentation of the projectile, and enhanced projectile yaw.

In the second subtask, an interface will be developed which will allow visualization of the wound. This visualization will be used in the final subtask which involves selecting casualties from an autopsy data base for simulating specific wounds. This will be done to refine models and certify model fidelity.

Task 4 integrates biomechanical software which describes the moment generating capability of joints given the initial and deformed geometry of the bones, muscles and tendons resulting from the projectile interaction. The final task, Task 5, is an administrative task related to preparation of deliverables.

The models from this effort will eventually be imported into a lower extremity battlefield trauma simulator under development by Musclographics, Inc. for ARPA. The simulator will be used to train combat medics in the management of lower extremity trauma. During 1996-97, these simulators will begin replacing the use of animals in trauma management training of combat medics.

The current paper describes progress during the first year which focuses on the first two tasks, simulation of soft tissue response and bone trauma.

2. PHENOMENOLOGY

The gross morphology of a typical penetrating wound from a projectile into skeletal muscle tissue can be thought of as divided into three zones. First there is the *permanent wound cavity* which is a hole containing blood clots, detached chunks of tissue, and foreign material that may have been aspirated or carried into the wound. Surrounding the permanent wound cavity is a *zone of extravasation* which is grossly hemorrhagic, shredded, pulped muscle around the permanent cavity. Farther away is the *zone of concussion* which is grossly normal muscle but with histological abnormalities such as interstitial hemorrhage and abnormal myocytes.

Traditional soft-tissue wound surgery excises the hemorrhagic, shredded, pulped tissue of the zone of extravasation and some of the neighboring zone of concussion. Skeletal muscle tissue is surgically excised if its color is abnormal, if it fails to contract when simulated, if its circulation is impaired (i.e., not bleed when cut), and if it has abnormal consistency.¹

Immediately upon projectile impact with tissue, high amplitude stress waves radiate from the impact region. Figure 3 shows a schematic of a ballistic test series recently completed on ordnance gelatin targets. Ordnance gelatin of various formulations is conventionally used to simulate skeletal muscle tissue during ballistic testing.

In our experiments, gelatin formulation (10, 15 and 20 percent), projectile geometry (spheres of various diameters, cones, and parallelepipeds of various constituent materials) and striking velocity were parametrically varied. Target geometry was also varied (homogeneous parallelepipeds of different lengths and widths, with and without various types of inclusions, e.g., simulated femur). Striking velocity, temporally resolved pressure histories at particular insitu target locations, and transient and permanent gelatin displacements were recorded for the various experiments.

¹ Col., R.F. Bellamy, M.D., FACS, and BG. R. Zajtchuk, M.D., FACS, "The Physics and Biophysics of Wound Ballistics," Chapter 4 of *Textbook of Military Medicine: Conventional Warfare*, Office of the Surgeon General, Department of the Army, 1991, page 142.

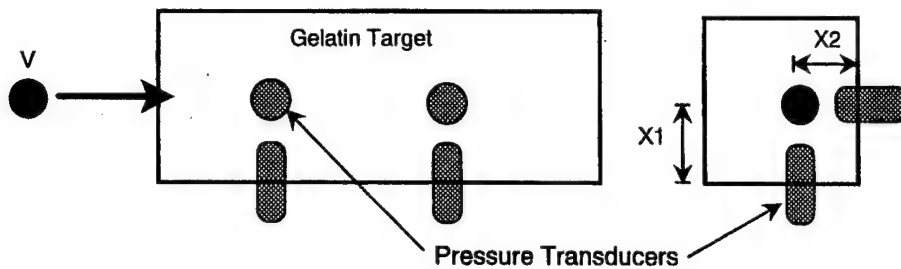


Figure 3. Schematic of Ballistic Test

The shadowgraph (back lighted photograph from diffuse light source) shown in Figure 4 shows a typical diffraction pattern (longitudinal section) from a low velocity impact of a sphere on a 20% gelatin target. Figure 5 shows a typical diffraction pattern at a significantly higher velocity recorded 1.33 msec after impact. These diffraction patterns record the transient displacement of the gelatin target after passage of the projectile. These displacements eventually collapse due to the elastic recoil of the tissue resulting in a much smaller permanent wound tract similar to that shown in Figure 6.



Figure 4. Shadowgraph of Low Velocity Impact

Preceding passage of the projectile and coinciding with target impact are large pressure transients.

Figure 7 shows a pressure time history from a 0.25 inch steel sphere with a striking velocity of 1,570 ft/sec on a 10% ordnance gelatin target. This data was recorded 0.5 inches above the projectile trajectory 2.40 inches downstream of the impact site. The measured peak pressure was 1,349 psi.

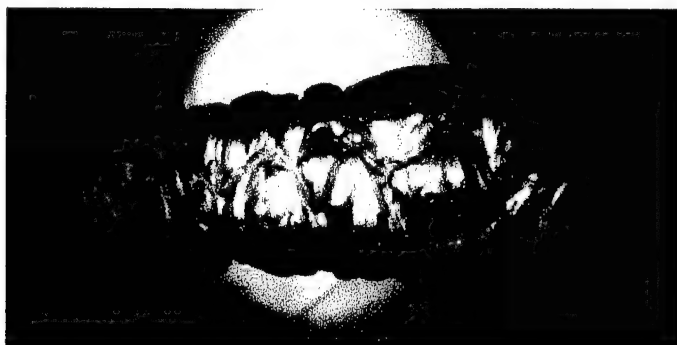


Figure 5. Shadowgraph of High Velocity Impact

Recorded pressure versus time traces are similar in shape and exhibit an initial steep rise to a local maxima about 1/2 of the peak value that is manifested later in the trace. This first peak is followed by a reduced pressure and gradual pressure elevation to a second peak which is the maximum pressure recorded. The second peak is then followed by an exponential decay to ambient

value that is manifested later in the trace. This first peak is followed by a reduced pressure and gradual pressure elevation to a second peak which is the maximum pressure recorded. The second peak is then followed by an exponential decay to ambient



Figure 6. Longitudinal Cross-Section of Permanent Cavity

wake of the projectile. Finally, intense dynamic oscillations affecting the entire target are evident in late time. These structural oscillations occur on the order of milliseconds.

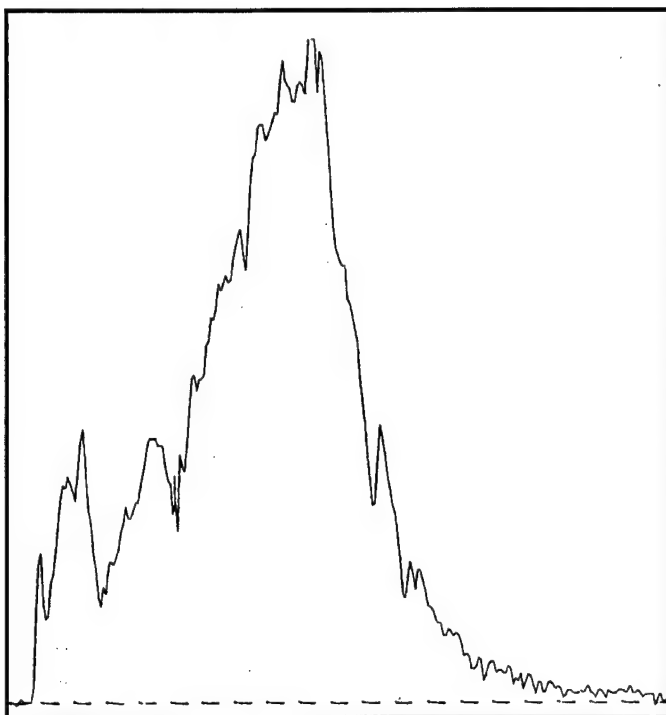


Figure 7. Measured 240 microsecond Pressure Pulse from Impact

pressure. The pressure transients evolve over about a hundred μ sec in these experiments reaching a peak when the projectile is nearest the pressure transducer. The gelatin displacement evolves over hundreds of μ sec in the

Peak pressures are plotted in Figure 8 as a function of striking velocity for 0.250 inch diameter spherical projectiles. The data identified by circles is for 20% gelatin targets and the square symbols represent 10% gelatin targets. The data point represented by the triangle was recorded closer than the nominal 0.5 inch lateral distance from the trajectory. For this data point the lateral distance was estimated to be 0.25 inches. This point falls well above the other data which we have attributed to the close proximity of the trajectory.

Figures 9 and 10 show a shadowgraph and pressure trace from a ballistic test on a simulated femur imbedded in a gelatin matrix. The pressure experienced at the location of the pressure transducer on the surface of the femur (45 degrees off-axis) is nearly 2,100 psi with a very steep rise and sharp drop. This is typical of shock loading and reflection and is very different from the pressure traces seen in homogeneous targets.

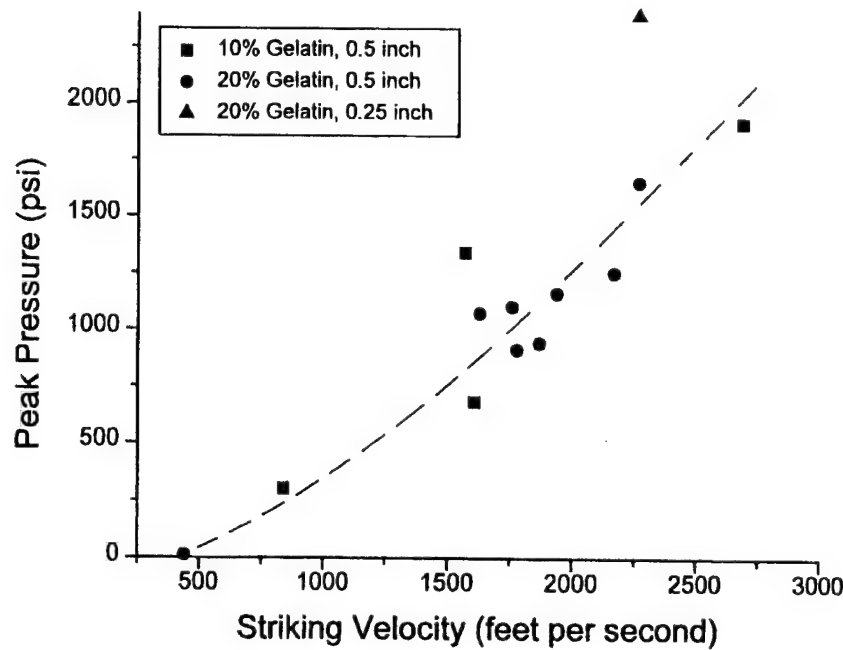


Figure 8. Peak Pressures are Proportional to Striking Velocity Squared.



Figure 9. Shadowgraph of Ballistic Experiment with Simulated Femur.

3. MODELING

The modeling effort is proceeding in two phases. In both phases, models describing temporally and spatially evolving stress and strain fields in the neighborhood of the projectile trajectory are being developed.

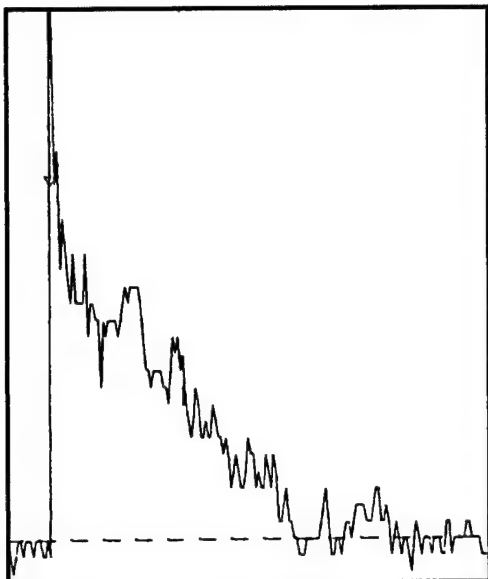


Figure 10. Shock Front and 98 microsecond Trace from Simulated Femur In situ Pressure Transducer

Models in the first phase are being developed with reference to ballistic experiments on biosimulants where various parameters in the experiments are being systematically varied. At this stage of the model development, it is assumed that the biosimulants manifest some phenomenology in common with the corresponding projectile interaction in human tissue. The goal of the model development activities is to obtain

algorithms with a functional form that describes important phenomenological characteristics of the projectile target interaction. In addition to identifying the functional form of model algorithms, model parameters can be physically interpreted. This physical interpretation arises from seeing the effect on projectile terminal ballistics of parametric variations in ballistic test conditions such as target mechanical properties, projectile geometry and velocity.

Once the functional forms have been posited and model parameters interpreted, the second phase of the modeling activities begins. This second phase which begins later this year, concerns extrapolation of the first phase algorithms to human tissue. This extrapolation is accomplished by substituting tissue properties from fresh unembalmed cadavers into model parameters developed in the first phase of the effort. The resulting second phase models are then compared with wound tract and associated tissue damage documented in wound data autopsies (e.g., Wound Data and Munitions Effectiveness Teams, WDMET, from Vietnam).²

In the first year of this project, algorithms have been developed which describe the retardation of the projectile as a function of penetration depth into a multilayer, multiphase viscoelastic medium.³ Models have also been developed which describe

² The WDMET data base maintained at the Uniformed Services University of Health Sciences in Bethesda, Maryland contains records of more than 8,000 autopsies from battlefield wounds in Vietnam. These records include over 120,000 slides along the wound tract, original x-rays, histological sections, clothing, projectile fragments, and in some cases interviews with witnesses.

³ A.K. Chatterjee, R.D. Eisler, and G.H. Burghart, "Penetration of Projectiles in Gelatin," Werner Goldsmith Symposium sponsored by the Joint Applied Mechanics and

FOOTNOTES, Continued

target transient displacement based on the quasistatic generalized stress-strain curve of the target material. The residual cavity is obtained by determining accumulation of inelastic strain in the target. Damage in affected areas is determined by comparing evolved stress and strain with empirically determined ultimate values for specific tissues.

Lateral displacement of target material is determined by using the velocity profile of the projectile during penetration and projectile leading edge geometry to predict local motion of target material around the projectile. In the event that the projectile manifests unstable rotational motion, the leading edge geometry is changed as a function of time to mimic projectile kinematics. The projectile rotational kinematics are predictable since the projectile retardation model entails modeling the distribution of retarding forces around the projectile.⁴ Key elements of this model are algorithms which describe the location on the projectile where boundary layers shed and how target material sticks to the surface of the projectile during penetration. Currently, these algorithms have developed to show parametric sensitivities in terms of the variables above and how target displacement velocities vary. Ballistic experiments will be used to establish the correct values of these parameters.

4. SIMULATION

The algorithms discussed above are used in the formulation of a three dimensional nonlinear spring lattice which is used to simulate soft tissue response local to the region of ballistic insult (see Figure 11). When a ballistic injury occurs, this lattice is superimposed on the polygonal element representation of the virtual anatomy.

The tissue stress-strain curve is measured from fresh unembalmed cadavers and is used to calibrate the springs in the lattice. The velocity profile of the projectile along the trajectory is used to determine the locations and time where the lattice is cut. The algorithms which describe transient displacement of the target material are used to determine initial velocities imposed on the spring network at the location of the lattice defects.

Materials Summer Meeting of the American Society of Mechanical Engineers and the University of California, Los Angeles, 28-30 June 1995.

⁴ A detailed explanation of the methodology and comparison of experimental results with model predictions is given for a fin stabilized 19.6 grain flechette in: R.D. Eisler, A.K. Chatterjee, S.F. Stone, and G.H. Burghart, *Algorithm Development to Describe Retardation in Human Tissue of a 19.6 Grain Flechette*, Mission Research Corporation report MRC-COM-93-372(R1), U.S. Army Natick Research, Development, and Engineering Center contract DAAK60-920C-0003, 15 May 1994 (To be published as a Natick Technical Report).

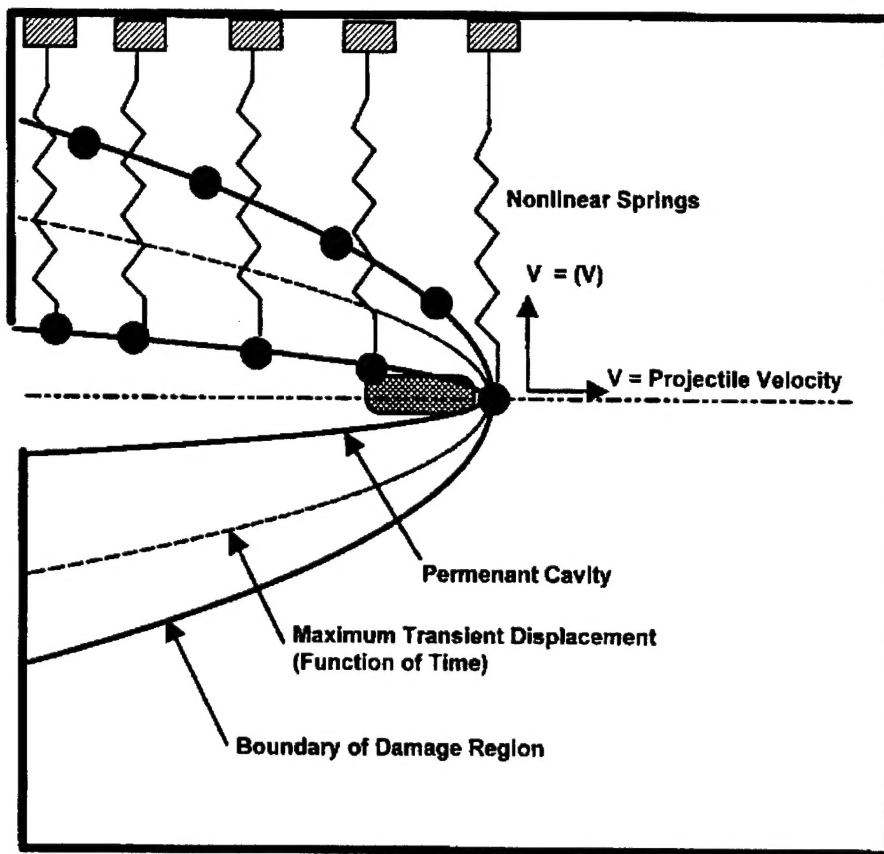


Figure 11. Schematic of Non-Linear Spring Lattice

The spring lattice enables simulation of the soft tissue dynamic response from which the a description of the residual wound tract is described based on accumulation of inelastic strain. Damage adjacent to the wound tract is also described based on the stress-strain field developed by the tissue, e.g., the region in which blood vessels rupture.

Relative to bone trauma; penetration, ricochet, and fracture mode resulting from the projectile interaction is described as well as perturbation of the projectile kinematics. Ejection of secondary bone fragments and their influence on soft tissue response is also being developed. Convergence studies on how tissue mass can be discretized and the influence of terms in the springs stiffness have already been studied.

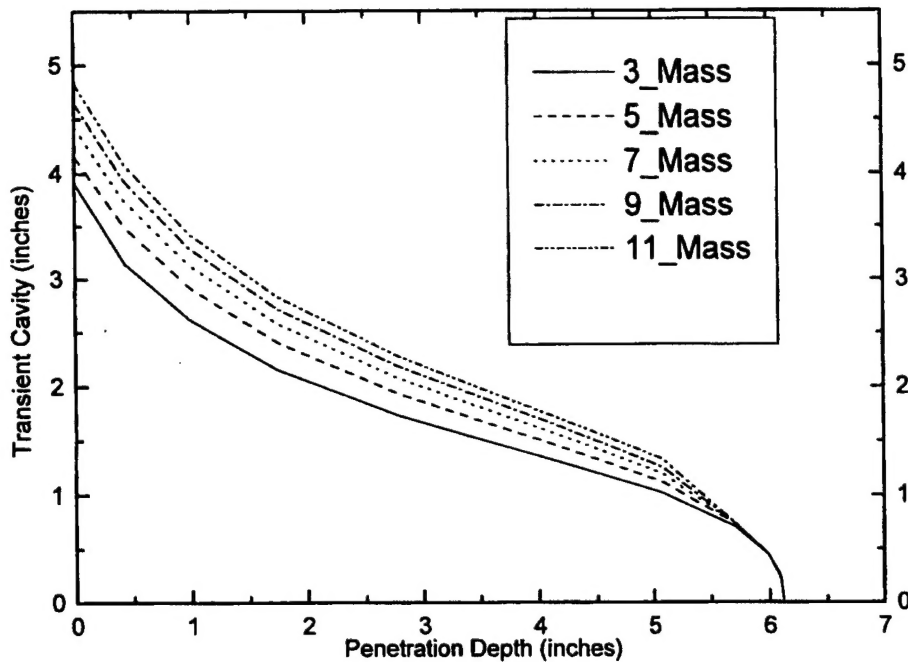


Figure 12. Tissue Displacement with Different Mass Discretization Schemes

Figure 12 shows maximum transient cavity radius as a function of penetration depth for different target mass discretization schemes. Figure 13 shows scaled displacement as a function of penetration depth for a 0.177 cm diameter, 431 mg sphere, striking 20% gelatin at 1,780 ft/sec. The diameter of the permanent cavity, maximum extent of the transient displacement, and affected region of tissue is superimposed on this plot. We are currently in the process of correlating these results with recently completed ballistic experiments.

5. ACKNOWLEDGEMENT

This effort is sponsored by the Advanced Biomedical Technology Program at the Advanced Research Projects Agency (ARPA) and is administered through the U.S. Army Medical Research Acquisition Activity, contract DAMD17-94-C-4099, entitled *Simulation and Assessment of Musculoskeletal Trauma due to Missile Penetration*.

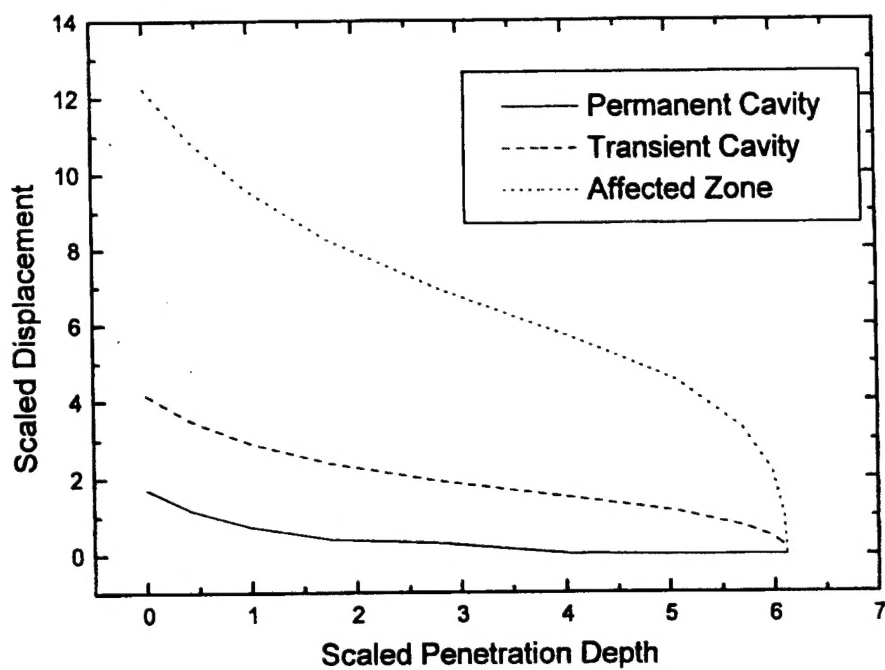


Figure 13. Non-Linear Spring Lattice Results

Personnel Supporting This Effort

Mission Research Corporation

Robert D. Eisler

Amiya K. Chatterjee

GB Laboratory, Inc

George H. Burghart

Steven Burghart

Musculographics, Inc.

Peter Loan

Arthur Wong

Randy Hudson